TUNING MATERIALS' PROPERTIES BY NON-PERTURBATIVE CAVITY QUANTUM ELECTRODYNAMICS

Erika Cortese
Supervisor: Prof. Simone De Liberato

School of Physics and Astronomy
Faculty of Physical Sciences and Engineering
University of Southampton

A thesis presented for the degree of
Doctor of Philosophy

14/07/2020

Declaration

I, Erika Cortese, declare that the thesis entitled 'Tuning Materials' properties by non-perturbative Cavity Quantum Electrodynamics' and the work presented in it are both my own, and have been generated by me as the result of my own original research. I confirm that:

- this work was done wholly or mainly while in candidature for a research degree at this University;
- where any part of this thesis has previously been submitted for a degree or any other qualification at this University or any other institution, this has been clearly stated;
- where I have consulted the published work of others, this is always clearly attributed;
- where I have quoted from the work of others, the source is always given. With the exception of such quotations, this thesis is entirely my own work;
- I have acknowledged all main sources of help;
- where the thesis is based on work done by myself jointly with others, I have made clear exactly what was done by others and what I have contributed myself;
- Part of the results presented in this work have been published previously in Phys. Rev. Lett. 2017 Jul 27;119(4):043604, Phys. Rev. A. 2017 Nov 28;96(5):053861, and Optica. 2019 Mar 20;6(3):354-61.

. Signed

Erika Cortese
23/04/2020

TUNING MATERIALS' PROPERTIES BY NON-PERTURBATIVE CAVITY QUANTUM ELECTRODYNAMICS

School of Physics and Astronomy
Faculty of Physical Sciences and Engineering
University of Southampton

Erika Cortese

Abstract

When in a quantum optical system the coupling between matter and cavity mode becomes comparable to the bare excitation frequency, we enter a non-perturbative coupling regime, as perturbation theory fails describing the system's dynamics. While recent advances in Cavity Quantum Electrodynamics allowed to achieve very high values of the coupling strength, thanks to the resonators properties optimization and the employment of solid-state devices, an ever growing interest has been shown about the possibility of significantly modify materials' properties. It has been demonstrated that the chemical structure of molecules strongly coupled to a photon mode can be altered, which opens the possibility to manipulate and control chemical reactions.

The aim of this thesis is to explore non-perturbative regimes on several quantum systems, and to investigate the effects of the coupling upon their properties, such as internal degrees of freedom or electronic states structure. I first developed a novel theory to determine the polariton spectrum of a dipolar ensamble in which a Ising-like dipole-dipole interaction in the

non-perturbative regime is considered. A further important focus is the investigation of the saturation effects due to the inclusion of the inter-dipole interaction, and the interplay between the latter and light-matter coupling strength. I also explored specifically the influence of the coupling on the rotational degrees of freedom of an ensemble of two-dimensional freely rotating dipoles, all coupled to a single cavity mode, finding that they are driven by the collective light-matter coupling to undergo a crossover between an isotropic and an aligned phase. I then investigated the case of cavity-embedded doped quantum wells, demonstrating that not only it is possible to couple a discrete cavity mode and bound-to-continuum transitions, but also that a novel bound exciton state appears, induced by the coupling strength. This results shows how light–matter coupling can be used to tune both optical and electronic properties of semiconductor heterostructures beyond those permitted by mere crystal properties. Finally, I explored the physics of an array of THz metamaterial resonators coupled to cyclotron resonances of a two-dimensional electron gas, developing a multiple-mode theory that takes in account the interaction between multiple photon modes mediated by the electrons. My results show that this cross-interaction, due to the strong two-dimensional geometry of the optically active medium, leads to the hybridization of different uncoupled photon modes, and manifests as a visible change of the distribution of the coupled electromagnetic field.

Acknowledgements

First of all, I would like to thank my supervisor Prof. Simone De Liberato not only for the great support and guidance during my PhD studies, but also for being extremely kind and patient, for teaching me with great enthusiasm and clarifying all my doubts. He has always encouraged me to pursue my ideas and be independent in my research experience. There are a lot of people I wish to thank for helping me during these years. I wish to thank every single member of my group, old and new: Dr Christopher Gubbin, who has always been very kind and helpful not only when I was struggling with both physics and numerical coding, but also as a friend in my daily life; Dr Nathan Shammah, for being very welcoming when I arrived in Southampton for the first time and being very helpful in research and not; Dr Luigi Garziano, who collaborated with me for the realization of my second paper; Wang Yuan, for being such an enthusiast student but also a great help for me in many occasions. I have to thank Prof. Salvatore Savasta and his group, who has been my bachelor thesis supervisor introducing me to the extraordinary field of cavity quantum electrodynamics. I also wish to thank all my external collaborators: Prof. Raffaele Colombelli and Prof. Iacopo Carusotto, who have contributed to the idea of Cavity-induced Bound Exciton, coauthoring my third theoretical paper. I must thank especially Prof. Colombelli for strongly believing in the project and supervising the experimental measurements. I must thank Prof. Christopher Lange and his group in Regensburg for starting a precious collaboration about ultrastrong coupling of Landau polaritons and allowing me to participate in person to some of the experimental sessions.

A special thank goes to my friends, Elisabetta, Andrea, Aurora, Valeria and Graziana, who supported my life choices from very far away always believing in my capabilities. I wish to thank all my friends here in Southampton, Carla, Alessandra, Viviana, Nadia, Luca who made happier even the worst

periods.

A very special thank goes to my partner Bruno, who supports me with his love and encouragement and teaches me to always live my life with positive attitude.

Last but not least, I wish to thank my all family, my brother Fabio, my step-father Nino, and especially my mother Daniela, who has always believed in me and encouraged me to follow my own way in life, although this way would take me far from her.

This thesis is dedicated to my father Ettore, who, I believe, is watching over me with love and pride. Every my single step has been taken for him.

Publications treated in this thesis

- Cortese E, Lagoudakis PG, De Liberato S. *Collective optomechanical effects in cavity quantum electrodynamics*. Phys. Rev. Lett. 2017 Jul 27;119(4):043604.

- Cortese E, Garziano L, De Liberato S. *Polariton spectrum of the Dicke-Ising model*. Phys. Rev. A. 2017 Nov 28;96(5):053861.

- Cortese E, Carusotto I, Colombelli R, De Liberato S. *Strong coupling of ionizing transitions*. Optica. 2019 Mar 20;6(3):354-61.

Accepted for publication in Nature Physics (2020 Jul 3)

- Cortese E, Tran L, Manceau JM, Bousseksou A, Carusotto I, Biasiol G, Colombelli R, De Liberato S. *Excitons bound by photon exchange*. arXiv preprint arXiv:1912.06124. 2019 Dec 12.

Contents

Chapter 1

Introduction

Cavity quantum electrodynamics (CQED) investigates the interaction of matter with single photons confined in a cavity. This field finds its origin in the Purcell's landmark work published in 1946 [1], demonstrating that the spontaneous emission rate of an excited atom can be enhanced or suppressed by changing the boundary conditions of the electromagnetic field by the employment of engineered cavities. Since then, several pioneering experiments performed on single atoms, or ions, such as Rydberg atoms in high-Q microwave cavities [2], and single atoms in a optical cavity [3], showed significant modifications of the spontaneous emission rates by achieving ever-higher cavity quality factors and light-matter coupling strengths. These experiments eventually started showing photon lifetimes inside the cavity sizeably bigger than the spontaneous emission rate, leading the system to undergo multiple absorption and remission before the photon could escape the cavity [4, 3]. This regime is known as *strong coupling* (SC) regime. This phenomenon has been soon observed on multiple solid-state systems, such as Wannier excitons in semiconductor optical microcavity [5], and nowadays CQED experiments are performed on a wide range of platforms, from microcavity embedded quantum wells [6], to quantum dots [7] and superconducting circuits [8].

SC regime is usually defined in terms of its spectroscopic observation: it occurs when the resonant coupling of an optically active transition with light is larger than the losses determining its spectral linewidth. It thus becomes possible to resolve a resonant coupling-dependant energy splitting, which is SC fundamental signature. In such a regime, the interaction between light and matter cannot be described in terms of emission and absorption of photons, but it is necessary to consider the *dressed* light-matter states of

the coupled system, called *polaritons* in case of matter bosonic excitations (such as excitons in a quantum well). While achieving SC for single emitters remains a challenging task [6], modern solid-state CQED technologies exploit, instead, the coherent collective coupling of a collection of optical active dipolar transitions to reach coupling strengths much larger than the one resolvable in the first observations of SC regime [9, 10, 11]. When the coupling strength becomes comparable to the spacing between different excited levels of the quantum matter system, it is possible to observe a mixing of the excited states, which modifies their matter properties. This phenomenon has been first predicted by Khurgin in 2001 [12], and later experimentally observed in 2017 in microcavity polaritons [13]. In this system, a coupling strength comparable to the exciton binding energy leads to an hybridization of the coupled exciton wavefunctions, which manifest a modified exciton radius length.

However, for coupling of this magnitude the dynamics can be still be described via first-order perturbation theory, and the number of the excitations in the system remains conserved. On the contrary, as the coupling strength becomes comparable to the bare transition energy, higher order phenomena come to play, such that we enter a *non-perturbative* regime, called *u*ltrastrong coupling (USC) regime. This was first predicted in [14], then observed for the first time in intersubband polaritons in cavity-embedded quantum wells, where the coupling strength can be easily tuned by adjusting the electron density [9]. USC has been studied both theoretically and experimentally in a variety of different systems, which exhibit not only a significant change in their spectral response, but also a rich new phenomenology [15, 16, 17, 18, 19], mainly due to the presence of a finite population of virtual excitations in their *dressed* ground-state [14, 20, 21, 22, 23].

Beyond the fundamental implications of CQED regimes, lot of interest has been shown for their applications. The capability of tuning the eigenenergies of the system by enlarging or shortening the resonant splitting, and by controlling the photon/matter content weights of coupled states finds application in photochemistry and material science [24, 25, 26]. It has been demonstrated that not only chemical reactions can be triggered, activated or suppressed by manipulating the molecular potential energy surfaces (PES) [27, 28, 29, 30, 12], but also structural features and degrees of freedom of molecular system can be affected by the coupling to a photonic field [31, 32, 27, 33, 30, 34]. As a consequence, the new field of *Polariton Chemistry* arised in the last decade [35, 36], motivated also by the concomitant development of

plasmonic technology, which has recently allowed to achieve a single-molecule SC [37]. Addressing ever larger couplings not only makes phenomena related to coupling-induced energy shifts more evident, but brings also a number of important consequences, such as the modification of matter states wavefunctions in VSC [12, 13], or non-linear saturation effects due to a dramatic alteration of the ground state nature at couplings comparable to the bare transition energy [38, 39]. Given the growing general interest in the applications of non-perturbative CQED phenomena, my PhD research project has the overall purpose of revealing their enormous potential as tool to tune materials' properties. Therefore, my research consists in the investigation of the effects of light-matter coupling on CQED systems in non-perturbative regimes, when the degrees of freedom, the electronic structure and internal interactions of the matter system are taken into account.

It is necessary to mention that my study has been exclusively of theoretical nature. However, thanks to the precious collaboration of some experimental groups, who will be mentioned throughout this dissertation, I had the opportunity to explore the real implementations of specific CQED systems, and to observe the experimental evidences of some of the phenomena predicted by our theory. I have also been invited by Prof. Christopher Lange to visit the THz-spectroscopy laboratory at the University of Regensburg (Germany) and partecipate to few lab sessions. Since the applicable phenomena I aimed to uncover had a general validity and could, in principle, be observed in many CQED set-ups, my investigation involved several matter-resonator platforms, ranging from molecular ensambles in open cavities to solid-state devices.

This dissertation illustrates the key results (peer reviewed and not) achieved during the last years, and it is articulated as follow. A first Chapter consists of a summary of the main background concepts and models employed in CQED theoretical descriptions, such as Rabi and Dicke models and respective approximations. Where possible, the main solving approaches will be mentioned, as well as their limitations. With the second Chapter we enter in the core of the dissertation. In particular, this is dedicated to the development of an novel accurate theory allowing to determine the polariton spectrum of an ensamble of mutually interacting dipoles in the USC regime. Moreover, we here investigate the saturation effects due to the inclusion of the Ising-like dipole-dipole interaction, and their impact on the effective light-matter coupling strength. In the third Chapter, we explore the effects of non-perturbative CQED on specific internal matter degrees of freedom.

In particular, it is shown that an ensemble of 2-dimensional freely rotating dipoles, coherently coupled to a single cavity mode, is driven by the collective light-matter coupling to undergo a crossover between two orientational configurations. More importantly, it is demonstrated that this cavity-induced ordering in highly excited systems energetically scales as a collective coupling, and not as the single-molecule one, as shown in previous works that investigate other kind of molecular degrees of freedom [31, 33]. This collective phenomena manifests itself as a significant change of the average internal energy of the highly excited system as the effective temperature decreases or the excitation rate increases, calculated by thermodynamic theoretical approaches. The fourth Chapter theoretically and experimentally explores the case of a cavity-embedded doped quantum well heterostructure, demonstrating that not only it is possible to achieve SC between a discrete cavity mode and ionizing transitions, but also that a cavity-induced novel bound exciton state appears where the uncoupled system showed none. In the fifth Chapter, we investigate the non-perturbative regime when several photon modes are involved in the coupling-induced hybridization. Aiming to theoretically explain both the simulated transmission spectra and the electric field maps of an array of THz metamaterial resonators coupled to cyclotron resonances of a two-dimensional electron gas, we develop a multi-mode theory able to fit the multiple polariton resonances. More importantly, our theory succeeds in reproducing some (so far unexplained) spectral features, thanks to the inclusion of a spatial overlap between different photon modes upon the surface of the electron gas. We show that this overlap leads to an hybridization of the different uncoupled photon modes, and manifests its self at high electron density as a visible change of the coupled electromagnetic field maps. In the final Chapter, we summarize the presented results and highlight future perspectives of my research project.

Chapter 2

Introduction to cavity QED and theoretical models

2.1 Introduction

In the following chapter we will present some of the main theoretical concepts of CQED, necessary for the full understanding of this thesis, including the fundamental theoretical models and the computational approaches adopted for the description of the different quantum systems taken into account.

2.2 Light-matter interaction Hamiltonian

Let us consider a dipolar interaction between a single photonic cavity mode of energy $\hbar\omega_c$ and optically active transitions between an initial state $|g\rangle$ and multiple final states $|j\rangle$, with transition energies $\hbar\omega_{g,j}$. The Hamiltonian for such a system can be derived by the minimal-coupling substitution $\hat{p} \rightarrow \hat{p} - e\hat{A}(\mathbf{r})$ into the matter kinetic Hamiltonian $\hat{H}_{kin} = \frac{\hat{p}^2}{2m}$ (with e and m_e, respectively, the elementary charge and charged particle mass, $\hat{p}$ the momentum operator and $\hat{A}$ the vector potential operator),

$$\hat{H} = \hat{H}_{EM} + \frac{\left(\hat{p} - e\hat{A}(\mathbf{r})\right)^2}{2m_e} + V(\mathbf{r}), \tag{2.1}$$

where $\hat{H}_{EM}$ is cavity field Hamiltonian and $V(\mathbf{r})$ is the Coulomb potential. From the expansion of Eq. 2.1, we obtain the light-matter interaction Hamil-

tonian as a sum of two terms

$$\hat{H}_{LM} = \hat{H}_{int} + \hat{H}_{dia}, \tag{2.2}$$

with

$$\hat{H}_{int} = -\frac{e\hat{p}\hat{A}(\mathbf{r})}{m_e}, \tag{2.3}$$

$$\hat{H}_{dia} = -\frac{e^2\hat{A}(\mathbf{r})^{\mathbf{2}}}{2m_e}. \tag{2.4}$$

$\hat{H}_{dia}$ is known as A^2 term or *diamagnetic* term, as it is responsible of the occurrence of diamagnetism.

The vector potential in the charged particle position can be written in the single-cavity-mode approximation, as $\hat{A} = A_0\left(\hat{a} + \hat{a}^\dagger\right)$, where $\hat{a}$ and $\hat{a}^\dagger$ are, respectively, the photon annihilation and creation operators, and A_0

$$A_0 = \sqrt{\frac{\hbar}{2\epsilon_0\omega_c V}}, \tag{2.5}$$

with ω_c photon energy, and V cavity volume where the electromagnetic field is confined. In the electric-dipole approximation, we arrive to express the light-matter Hamiltonian terms in the form

$$\hat{H}_{int} = \sum_j \hbar\Omega_R^j \left(|j\rangle\langle g| + |g\rangle\langle j|\right)\left(\hat{a} + \hat{a}^\dagger\right); \tag{2.6}$$

$$\hat{H}_{dia} = D\left(\hat{a} + \hat{a}^\dagger\right)^2, \tag{2.7}$$

where $|j\rangle\langle g|$ and $|g\rangle\langle j|$ are the raising and lowering transition operators, and coupling parameter $\Omega_R^j = \frac{\omega_{g,j}A_0\langle g|\hat{d}|j\rangle}{\hbar}$ with $\hat{d}$ transition dipole operator. The Hamiltonian term in Eq. 2.6 describes the interaction between the cavity field and the a number of matter transitions as multiple absorptions and emissions of photons with exchange rates Ω_R^j.

In order to solve this Hamiltonian, it is necessary to perform a truncation of the Hilbert space by reducing the number of matter levels taken into account. The light-matter coupling models presented below all rely on a single matter transition approximation, whose validity at larger coupling strengths is strongly Gauge dependent, as it has been demonstrated in multiple works [40].

2.3 Light-matter coupling regimes and models

2.3.1 Quantum Rabi model and RWA approximation

Let us thus now limit our self to the simplest case of a single optically active dipolar transition between an initial state $|g\rangle$ and a single final excited state $|e\rangle$, with energy difference $\hbar\omega_x$, coupled to a single cavity mode of energy $\hbar\omega_c$ by exchange rate Ω_R. This model is known as *Quantum Rabi model*, and its Hamiltonian can be written as

$$\hat{H}_{Rabi} = \hbar\omega_c \hat{a}^\dagger \hat{a} + \frac{1}{2}\hbar\omega_x \hat{\sigma}^z + \hbar\Omega_R \left(\hat{\sigma}^- + \hat{\sigma}^+\right)\left(\hat{a} + \hat{a}^\dagger\right), \tag{2.8}$$

where $\hat{\sigma}^z = |e\rangle\langle e| - |g\rangle\langle g|$ is one of the Pauli operators, $\hat{\sigma}^- = |g\rangle\langle e|$ and $\hat{\sigma}^+ = |e\rangle\langle g|$ are the Pauli lowering and raising operators connecting the ground state $|g\rangle$ and the excited state $|e\rangle$ of the 2LS. The first two terms in Eq. 2.8 represent the uncoupled energies, respectively, of single cavity mode and the optically active transition, while the last term can be recognize as the interaction Hamiltonian, as in Eqs. 2.6. Here, we shifted the Hamiltonian Eq.2.8 by the zero-point energy. The magnitude of the coupling strength Ω_R, compared to different parameters, determines the light-matter interaction regimes addressed by the system.

As far as the coupling remains smaller than any losses rate, the energy exchange process has an irreversible nature: the excitation energy gets lost before being exchanged multiple times between light and matter, and the only cavity-induced effect is the enhancement/suppression of the spontaneous emission rate according to the cavity density of states (Purcell effect) [1]. We call this regime *weak coupling* (WC). *Fermi Golden Rule* governing photon emission processes remains the most effective tool for the description for this kind of light-matter interaction.

We enter, instead, *strong coupling* (SC) regime when the coupling parameter Ω_R achieves values higher than the losses rate of the CQED system, and it is possible to observe a periodic exchange of the excitation between the emitter and the cavity field, called Rabi oscillations. The parameter Ω_R representing the frequency of the oscillations, is indeed also known as *Rabi frequency*. In this regime, a description in terms of photon absorption and emission results meaningless, as it is no longer possible to distinguish what is

light and what is matter excitation. Therefore, we are obliged to introduce novel *dressed quantum states* exhibiting an intrinsic dual nature.

Both the definitions of WC and SC are based on the comparison between the Rabi frequency and the losses. From a spectroscopic point of view, a coupling strength larger than the loss rate leads to a resolvable resonant energy splitting, which is a fundamental SC signature.

Let us now point our attention on the light-matter part in Eq. 2.8. We can expand it in two different components

$$\hat{H}_{int} = \hat{H}_{res} + \hat{H}_{anti-res}, \tag{2.9}$$

with

$$\hat{H}_{res} = \hbar\Omega_R \left(\hat{a}\hat{\sigma}^+ + \hat{a}^\dagger\hat{\sigma}^-\right), \tag{2.10}$$

$$\hat{H}_{anti-res} = \hbar\Omega_R \left(\hat{a}\hat{\sigma}^- + \hat{a}^\dagger\hat{\sigma}^+\right). \tag{2.11}$$

$\hat{H}_{res}$ contains the so called *resonant* terms, which conserve the total number of the excitations: as one photon is created in the cavity, one matter excitation is destroyed, and viceversa. In the quasi-resonant case, which means $\omega_c \approx \omega_x$, these terms connect states whose energy difference is close to zero. On the contrary, $\hat{H}_{anti-res}$ contains terms which do not conserve the number of the excitations, as they admit the double creation (or annihilation) of them, and connect states that, in the quasi-resonant case, differ by almost the double of the single excitation energy.

Let us now apply standard perturbation theory to evaluate the contribution of the interaction Hamiltonian upon the unperturbed states of the system. In the resonant case, first-order perturbation theory applied to a certain state $|\Phi\rangle$ gives

$$\Delta E^1_\Phi = \langle\Phi|\hat{H}_{int}|\Phi\rangle = \langle\Phi|\hat{H}_{res}|\Phi\rangle \propto \Omega_R, \tag{2.12}$$

which contains contributions only from the resonant terms. We can demonstrate that anti-resonant terms contribute only at the second order,

$$\Delta E^2_\Phi = \sum_{|\Psi\rangle\neq|\Phi\rangle} \frac{|\langle\Phi|\hat{H}_{anti-res}|\Psi\rangle|^2}{E_\Phi - E_\Psi} \propto \frac{\Omega_R^2}{\omega_x}, \tag{2.13}$$

which is of the order of $\Omega_R \times \frac{\Omega_R}{\omega_x}$. If we define the *normalised coupling* parameter as $\eta = \frac{\Omega_R}{\omega_x}$, we understand that its value determines whether it is necessary to include the anti-resonant terms .

As far as η remains negligible, we can set $\hat{H}_{anti-res} = 0$ by applying the so called *Rotating Wave Approximation* (RWA). By simply renormalising the bare photon frequency as $\tilde{\omega}_c \to \omega_c + 2\frac{\Omega_R^2}{\omega_x}$, we obtain the James-Cummings model [41] with Hamiltonian

$$\hat{H}_{JC} = \hbar\tilde{\omega}_c\hat{a}^\dagger\hat{a} + \frac{1}{2}\hbar\omega_x\hat{\sigma}^z + \hbar\Omega_R(\hat{\sigma}^+\hat{a} + \hat{\sigma}^-\hat{a}^\dagger). \tag{2.14}$$

This is the simplest model used for low-coupling SC cases. Since in the RWA the number of excitation is conserved and the dynamics develops in a 2D Hilbert subspace, Jaynes-Cummings Hamiltonian is easily analytically solvable and has a well known spectrum [41]. An analytical approach for the quantum Rabi Hamiltonian has been discovered only in 2011 [42], but, in most cases, it still relies on the numerical resolution of transcendental equations.

However, what happens when the coupling strength becomes comparable to the bare excitation frequency, that means when the normalised coupling η is comparable with the unity? As shown by perturbation theory, a larger normalised coupling implies larger second-order contributions due to the anti-resonant terms in the interaction Hamiltonian, which cannot be neglected for a correct description of the phenomena. When this happens, we enter a further light-matter coupling regime, that is known as *Ultrastrong coupling* (USC) regime (the historical conventional threshold to enter USC is $\eta = 0.1$ [9]). As its definition is based on a comparison between the Rabi and the bare transition frequencies, it follows that USC is not a *stronger* SC, as, in principle, it could admit losses larger than the coupling strength, that is the violation of SC requirements. Including the anti-resonant terms of the Hamiltonian leads to a series of interesting phenomena, as the appearance of virtual excitations, due to a change of the ground state of the system, that we will treat more in details on a next paragraph.

2.3.2 Many 2LSs models: Collective coupling

Dicke model

In the last decades, the achievement of ever larger coupling strengths has been object of an increasing interest of the CQED community. By recalling the form of the Rabi frequency presented in Sec.2.2, the coupling strength results proportional to the zero-point amplitude A_0, which means inversely

proportional to the square root of the cavity volume V. The most intuitive way to increase the normalised coupling is then reducing the mode volume where the photon field is confined. This strategy has been adopted in many CQED platforms, such as plasmonic nanocavities [37].

Another possible way to increase the light-matter coupling is having an ensamble of N 2LSs all interacting coherently with the same photon mode. This allows the effective coupling acquiring a collective nature [43]. In order to study the collective coherent light-matter interaction, it has been necessary to introduce a generalization of the Rabi model for a number N of 2LSs, called *Dicke model*, which reduces to *Tavis-Cummings model* under RWA [44]. Dicke Hamiltonian can be indeed written as

$$\hat{H}_{\text{Dicke}} = \omega_c \hat{a}^\dagger \hat{a} + \frac{1}{2}\sum_j \omega_j \hat{\sigma}_j^z + \sum_j \Omega_R^j \left(\hat{\sigma}_j^+ + \hat{\sigma}_j^-\right)\left(\hat{a} + \hat{a}^\dagger\right), \tag{2.15}$$

where the index j runs over the 2LSs.

Bosonic Approximation Let us notice that the Dicke model describes the interaction between a bosonic field and an ensemble of N electronic transitions, and as such, due to the electrons' fermionic nature, is affected by the Pauli blocking. This means that a collection of N 2LSs can be excited N times before saturation occurs, as electrons occupying at the same time the same quantum state would violate the Pauli exclusion principle.

However if we assume that the number of excitations n is much smaller than the total number N of 2LSs , we can approximate the Dicke model to a purely bosonic model. The latter describes the coupling between two bosonic fields, photons and bosonic collective matter excitations. This is formally seen by writing the collective excitation operators

$$\hat{b} = \frac{1}{\sqrt{N}}\sum_j \hat{\sigma}_j^-, \tag{2.16}$$

$$\hat{b}^\dagger = \frac{1}{\sqrt{N}}\sum_j \hat{\sigma}_j^+, \tag{2.17}$$

whose commutator, averaged on a quantum states with n excitations, is calculated as

$$\langle n|[\hat{b}, \hat{b}^\dagger]|n\rangle = 1 + O\left(\frac{n}{N}\right). \tag{2.18}$$

In the dilute regime condition $\frac{n}{N} << 1$, the collective operator b obeys the well known bosonic commutation rules $[\hat{b}, \hat{b}^\dagger] = 1$.

A simplified single-mode version of this bosonised Hamiltonian is

$$\hat{H}_{\text{Bos}} = \omega_c \hat{a}^\dagger \hat{a} + \omega_x \hat{b}^\dagger \hat{b} + \hat{H}_{LM}; \tag{2.19}$$

with

$$\hat{H}_{LM} = \Omega_R \sqrt{N} \left(\hat{b} + \hat{b}^\dagger\right) \left(\hat{a} + \hat{a}^\dagger\right); \tag{2.20}$$

where $\hat{b}$ and $\hat{b}^\dagger$ are the annihilation and creation operators for the bosonic excitations, and $\Omega_R\sqrt{N}$ is the *collective coupling*. The latter represents a very important key point, as it formally explains why coherently coupling a collection of 2LSs to a single cavity mode leads to a significant enhancement of the effective light-matter coupling strength. In other words, a collection of N dipoles coupled to a cavity behaves as a single dipole $\sqrt{N}$ times larger. This is also at the origin of the *Dicke superradiance* [43].

Hopfield model and Diamagnetic term

The boson Hamiltonian derived from the Dicke model, showed in Eq. 2.19, describes the interaction between two harmonic oscillators. An equivalent but independent model describing the interaction between photons and bosonic collective excitations (such as excitons) of a matter system is the *Hopfield model*. Its Hamiltonian can be written as

$$\hat{H}_{\text{Hop}} = \omega_c \hat{a}^\dagger \hat{a} + \omega_x \hat{b}^\dagger \hat{b} + \hat{H}_{LM} + \hat{H}_{dia}; \tag{2.21}$$

with

$$\hat{H}_{LM} = \Omega \left(\hat{b} + \hat{b}^\dagger\right) \left(\hat{a} + \hat{a}^\dagger\right); \tag{2.22}$$

$$\hat{H}_{dia} = D \left(\hat{a} + \hat{a}^\dagger\right)^2. \tag{2.23}$$

Unlike the Dicke model, the Hopfield Hamiltonian formally conserves the diamagnetic term. The latter, weighted by the parameter D, does not conserve any information about the emitter levels structure. Therefore, a truncation of this may lead to an overestimation of $\hat{H}_{dia}$ compared to $\hat{H}_{int}$. Nevertheless, the Thomas-Reiche-Kuhn (TRK) sum rule $\sum_j 2\frac{|\langle g|\hat{p}|j\rangle|^2}{\omega_{g,j}} = m_e$ comes

into play imposing a lower bound for the parameter D. By rewriting the diamagnetic Hamiltonian in Eq.2.23 as

$$\hat{H}_{dia} = \left(\hbar \sum_j 2 \frac{|\langle g|\hat{p}|j\rangle|^2}{\omega_{g,j}} \right) \frac{e^2 \hat{A}^2}{m^2} = \sum_j \hbar \frac{\Omega_R^j}{\omega_{g,j}} \left(\hat{a} + \hat{a}^\dagger\right)^2, \tag{2.24}$$

and comparing it to Eq. 2.7, derived from the minimal coupling substitution, we arrive to demonstrate that $D = \sum_j \frac{\Omega_R^j}{\omega_{g,j}}$. In the single mode approximation, the inequality

$$D \geq \frac{\Omega_R^2}{\omega_x} = \Omega_R \times \eta \tag{2.25}$$

is valid, becoming an equality if the transition fully saturates the TRK sum rule. This means that the weight D is not negligible in the USC regime, as the normalized coupling η becomes comparable to the unity [18].

The diamagnetic term assumes also the very important role of stabilizing the system against the occurrence of superradiant phase transitions [45, 46], predicted for values of η above a certain critic threshold [47, 48, 49, 50]. For the system to undergo a quantum phase transition, the coupling strength must be large enough to push one of the system eigenenergies to zero energy. The diamagnetic term can be reabsorbed by a rotation of the photon operators, at the price of renormalising the cavity frequency as $\tilde{\omega}_c = \sqrt{\omega_c^2 + 4D\omega_c}$. This blue-shift of the cavity frequency prevents the system from reaching the critic point of the phase transition, as a even larger coupling η would be necessary.

Polaritons Let us return to the Hamiltonian in Eq. 2.21. This results solvable by introducing the new *lower polariton* (LP) and *upper polariton* operators by *Hopfield Bogoliubov transformations* [51]

$$\hat{p}_\nu = x_\nu \hat{a} + z_\nu \hat{a}^\dagger + y_\nu \hat{b} + w_\nu \hat{b}^\dagger, \tag{2.26}$$

with $\nu \in [LP, UP]$, x_ν,z_ν,y_ν and w_ν known as Hopfield coefficients, obeying the normalisation rule $|x_\nu|^2 + |y_\nu|^2 - |z_\nu|^2 + |w_\nu|^2 = 1$. By applying the transformation above to the Hamiltonian, this takes the diagonal form

$$\hat{H}_{Hop} = \sum_\nu \omega_\nu \hat{p}_\nu^\dagger \hat{p}_\nu + E_G, \tag{2.27}$$

with ω_{LP} and ω_{UP}, respectively, the LP and UP eigenmodes frequencies, and E_G ground state energy.

Virtual excitation in USC regime

When we first introduced the USC regime, we mentioned that this is characterized by some important phenomena, which make this regime intrinsically different from WC and SC, and, as such, have been object of large interest in the last decade. One of them is the appearance of virtual excitations in the ground state, due to the presence of the anti-resonant terms in the light-matter Hamiltonian. The ground state of the uncoupled system is defined as $\hat{a}|0\rangle = \hat{b}|0\rangle = 0$, but, given the form of the new polariton operator in Eq. (2.26) describing the polariton eigenmodes, we see that $|0\rangle = 0$ can be no longer ground state of the coupled system, as $\hat{p}_\nu|0\rangle \neq 0$. A new ground state $|G\rangle$ has to be introduced, such that $\hat{p}|0\rangle = 0$, leading to a not zero population of photons and matter excitations. In the resonant case, we thus find

$$\langle G|\hat{a}^\dagger\hat{a}|G\rangle = |z_{LP}|^2 + |z_{UP}|^2 \propto \frac{\Omega^2}{\omega_x^2} + \mathcal{O}\left(\frac{\Omega_R^4}{\omega_x^4}\right), \tag{2.28}$$

$$\langle G|\hat{b}^\dagger\hat{b}|G\rangle = |w_{LP}|^2 + |w_{UP}|^2 \propto \frac{\Omega^2}{\omega_x^2} + \mathcal{O}\left(\frac{\Omega_R^4}{\omega_x^4}\right). \tag{2.29}$$

Let us notice that, at low coupling values, the virtual excitations population would be negligible. From a physical point of view, the appearance of excitations is due to an intrinsic change of the ground state nature. At low coupling strength, the ground state is a quantum state in which there are not photons inside the cavity and all the matter systems are in their lowest state. In USC, instead, the ground state becomes a dressed state mixed to multiple excited states containing different numbers of excitations.

2.3.3 Very Strong Coupling

The *Very strong coupling* (VSC) regime has been predicted by Khurgin in 2001 [12], and observed in microcavity polaritons in 2017 [52]. We enter this regime when the coupling becomes comparable to the spacing between the excited states of the quantum matter system. Here the 2Ls approximation breaks down, as the coupling strength results large enough to couple and thus hybridize the different excited states of the matter system. By applying a multi-level Hopfield model, we arrive to polaritons of the form

$$\hat{p}_\nu = x_\nu\hat{a} + z_\nu\hat{a}^\dagger + \sum_\alpha \left(y_{\alpha,\nu}\hat{b}_\alpha + w_{\alpha,\nu}\hat{b}_\alpha^\dagger\right), \tag{2.30}$$

where the operator $\hat{p}_\nu$ contains a sum over all the possible collective transitions between different matter energy states. As we will see, this leads to observable modifications of the matter and light coupled modes properties. In Khurgin's work, which investigates this regime on exciton-polaritons with a coupling strength comparable to the exciton binding energy, it is demonstrated that the radius of the exciton becomes a strong function of the coupling strength, manifesting clear signals of multi-matter-modes hybridization.

Further coupling regime: Deep Strong Coupling

For sake of completeness, we briefly introduce the *Deep strong coupling* (DSC) regime, occurring when the normalised coupling η overcomes the unity. In this regime, the second-order contribution of the anti-resonant terms, as well as the diamagnetic term contributions (both $\propto \eta^2$), not only become observable but results dominant over the first-order processes. It has been demonstrated that, when $\eta > 1$, the diamagnetic term can lead to an effective decoupling between light and matter, as it localises the photonic field away from the matter system [18]. This regime was theoretically investigated for the first time in 2010 [53], and experimentally demonstrated in 2017 on many different platforms [54, 55].

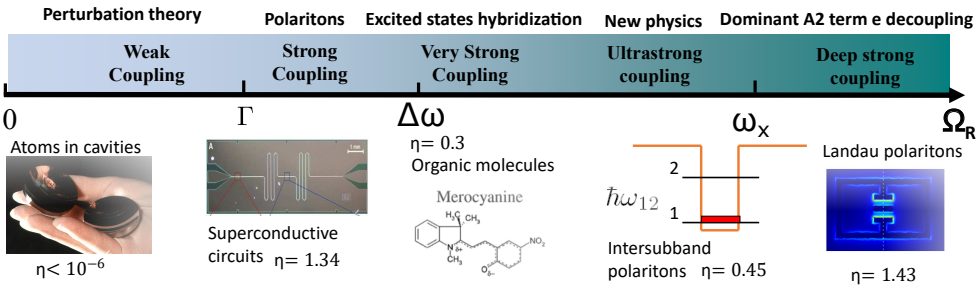

Figure 2.1: Top row: Scheme of light-matter coupling regimes as Ω_R increases with highlighted milestones: Γ loss rate, $\Delta\omega$ spacing between different excited states frequencies, ω_0 bare matter excitation frequency. Bottom row: main CQED platforms and record values of light-matter coupling strengths

.

The scheme in Fig. 2.1 is useful to remember the main signatures and

record values for each coupling regime. The reality is more complicated though. Our physical system will be more likely in more than one coupling regimes at the same time, because of their different definitions. One system could be simultaneously in USC, because its coupling strength is comparable to the bare frequency, in SC because it is larger than the losses, and in VSC if the coupling is also comparable to the excited states spacing. Throughout this dissertation, the different coupling regimes will be mentioned to highlight specific characteristic phonomena, but this does not exclude we entered the others.

Chapter 3

Saturation effects on polariton spectrum of a Dicke-Ising Hamiltonian

3.1 Introduction

The standard Hopfield model, presented in the previous chapter, thanks to a purely bosonic treatment, is the simplest model allowing to solve the dynamics of a multi-2LSs collection coupled to a single resonant cavity mode [51]. As far as we remain limited to the dilute regime and maintain both anti-resonant terms and the diamagnetic term in the Hamiltonian, the model describes quite accurately physical systems with a wide range of the normalised coupling strength, from WC to SC and USC regimes. Notwithstanding its general validity, this model still relies on the single mode approximation, and do not consider any specific structural feature or degrees of freedom in the matter component of the CQED system, treating it simply as an ensamble of 2LSs all coherently coupled to the same photonic mode. The validity of retaining a single optically active matter mode in the Hamiltonian has been demonstrated strongly gauge-dependent [56, 40], therefore, it is fully legitimate to wonder what happens in our theoretical description when we start pointing a magnifying lens on the structure and the internal interactions inside the matter system coupled to the light. Aiming to address this question, we investigate the specific case of a one-dimensional chain of dipoles, in which, together with the light-matter coupling to a single cavity mode, a

non-negligible longitudinal dipole-dipole interaction is included. This kind of system can represent in good approximation several kinds of molecular aggregates, e.g. J aggregates, which have been object of growing interest for displaying large values of both the light-matter coupling and of the inter-dipole coupling [57, 58, 59, 60].

We already know that the Dicke model (Sec. 2.3.2) describes a collection of dipoles coherently coupled to the same cavity mode, and, moreover, this can be easily solved in the dilute regime by applying the Hopfield approach, recovering the well known polariton spectrum. When a nearest-neighbour longitudinal coupling between the dipoles is called into play, the matter Hamiltonian describing their bare energies and mutual interactions takes the form of an Ising Hamiltonian in a transverse field, which can be solved exactly in terms of fermionic excitations through the Jordan-Wigner transformations [61, 62]. While in certain regimes exact approaches exist to solve both the Dicke and the Ising models separately, the two representations, one bosonic and the other fermionic, are incompatible. As a consequence, the full Dicke-Ising model, including both the longitudinal dipole-dipole interaction and the coupling with the transverse cavity photons, has until now been considered only from a thermodynamical perspective. It has been studied both analytically, by using a mean field approach to investigate the model's first- and second-order phase transitions [63, 64], and numerically ,by using matrix product states [65].

Our study aims, instead, to correctly determine the spectrum and the dynamics of a Dicke-Ising Hamiltonian, by exploiting higher order of the Holstein-Primakoff transformations [66], which map the matter excitation operators into bosonic operators. This theory remains valid for arbitrary values of the normalised coupling strenghts until the onset of the Ising ferromagnetic phase transition. Our results also reveal the nature and the implications of the interplay between the dipole-dipole and the light-matter coupling strengths, and their effect on the virtual excitations which populate the ground-state as the interactions become comparable to the bare transition frequency.

In the following, we summarize the theoretical background our work lies upon, that is the fermionic and bosonic representations of Ising and Dicke-Ising models, showing how the standard boson approach leads to meaningful deviations from the exact results as the coupling strength becomes relevant [67]. I will then introduce our novel approach, which allows to recover the correct spectrum of the Ising model in terms of bosonic excitations for ar-

bitrary values of the dipole-dipole interaction. For sake of clarity, only few necessary formulas are presented this chapter for who wishes extra details about the technical calculations to move to Appendix A.

3.2 The Ising Hamiltonian

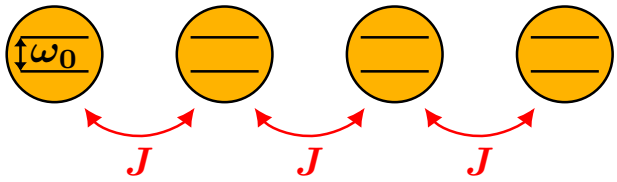

Figure 3.1: One dimensional chain of N coupled two level systems with transition frequency ω_0 and next-neighbour coupling strength J.

3.2.1 Standard theoretical models: Fermion and HP0 approximations

A one-dimensional chain of N interacting two-level systems of transition frequency ω_0 and dipole-dipole coupling strength J (Ising coupling) can be described by the Hamiltonian

$$\hat{H}_M = \sum_{n=1}^{N} \hbar\omega_0 \, \hat{\sigma}_n^+ \hat{\sigma}_n^- + \hbar J \sum_{n=1}^{N-1} (\hat{\sigma}_n^+ + \hat{\sigma}_n^-)(\hat{\sigma}_{n+1}^+ + \hat{\sigma}_{n+1}^-). \tag{3.1}$$

Applying the Jordan-Wigner transformation [61, 62] detailed in A 1.1, the Hamiltonian above can be put in the diagonal form

$$\hat{H}_F = \sum_k E_{F,k} \, \hat{d}_{F,k}^\dagger \hat{d}_{F,k} + E_F^0, \tag{3.2}$$

in terms of the operators $\hat{d}_{F,k}^\dagger$ and $\hat{d}_{F,k}$ obeying the fermionic anticommutation relations

$$\left\{\hat{d}_{F,k}, \hat{d}_{F,k'}^\dagger\right\} = \delta_{kk'} \ , \ \left\{\hat{d}_{F,k}^\dagger, \hat{d}_{F,k'}^\dagger\right\} = \left\{\hat{d}_{F,k}, \hat{d}_{F,k'}\right\} = 0, \tag{3.3}$$

where k is the quasi-momentum $0 < k < \pi$. The single-particle energies are

$$E_{F,k} = \hbar\sqrt{\omega_0^2 + 4J^2 + 4J\omega_0 \cos k} \tag{3.4}$$

, and the ground-state energy has the form

$$E_F^0 = \frac{1}{2}\left(N\hbar\omega_0 - \sum_k E_{F,k}\right). \tag{3.5}$$

Unfortunately this exact solution is not adequate to rigorously determine the polaritonic spectrum of an Ising chain coupled to a cavity photonic field, because its light-matter interaction Hamiltonian would contain both bosonic and fermionic operators.

Another approach consists of mapping the spin operators of Eq. 3.1 into fully bosonic one through the Holstein-Primakoff transformation

$$\begin{aligned}
\hat{\sigma}_n^+ &= \hat{b}_n^\dagger\sqrt{1-\hat{b}_n^\dagger\hat{b}_n} = \hat{b}_n^\dagger\left(1 - \frac{\hat{b}_n^\dagger\hat{b}_n}{2} - \frac{\hat{b}_n^\dagger\hat{b}_n\hat{b}_n^\dagger\hat{b}_n}{8} - \dots\right), \\
\hat{\sigma}_n^- &= \sqrt{1-\hat{b}_n^\dagger\hat{b}_n}\,\hat{b}_n = \left(1 - \frac{\hat{b}_n^\dagger\hat{b}_n}{2} - \frac{\hat{b}_n^\dagger\hat{b}_n\hat{b}_n^\dagger\hat{b}_n}{8} - \dots\right)\hat{b}_n,
\end{aligned} \tag{3.6}$$

where the $\hat{b}_n^\dagger$ operators now obey bosonic commutation relations

$$\left[\hat{b}_n, \hat{b}_{n'}^\dagger\right] = \delta_{nn'}\ ,\ \left[\hat{b}_n^\dagger, \hat{b}_{n'}^\dagger\right] = \left[\hat{b}_n, \hat{b}_{n'}\right] = 0. \tag{3.7}$$

If the population of the nth dipole $\hat{b}_n^\dagger\hat{b}_n$ is assumed to be negligible, we are then in the dilute regime and the expansion of Eq. 3.6 can be stopped at the first term. From now on, we refer to this approximation as *zero-th Holstein-Primakoff approximation* (HP0). This is the formal origin of the *bosonic approximation* widely adopted in the few-excitations regime for the standard Dicke model case, as seen in Sec. 2.3.2. In this case, the Hamiltonian in Eq. 3.1 can be written as

$$\hat{H}_{\mathrm{B}} = \hbar\omega_0\sum_{n=1}^{N}\hat{b}_n^\dagger\hat{b}_n + \hbar J\sum_{n=1}^{N-1}(\hat{b}_n + \hat{b}_n^\dagger)(\hat{b}_{n+1} + \hat{b}_{n+1}^\dagger). \tag{3.8}$$

Following the standard Hopfield procedure, one can write the Hamiltonian in the diagonal form

$$\hat{H}_{HP0} = \sum_k E_{B,k}\, \hat{d}^\dagger_{B,k} \hat{d}_{B,k} + E^0_B, \tag{3.9}$$

where $\hat{d}^\dagger_{B,k}, \hat{d}_{B,k}$ are bosonic operators and

$$\begin{aligned} E_{B,k} &= \hbar(\omega_0^2 + 4J\omega_0 \cos k)^{1/2}, \\ E^0_B &= \frac{1}{2}\left(\sum_k E_{B,k} - N\hbar\omega_0\right), \end{aligned} \tag{3.10}$$

are, respectively, the single-particle energy and the ground-state energy. Note that we use Pekar boundary conditions [68] for the wavevectors

$$k \equiv k(l) = l\pi/(N+1), \tag{3.11}$$

with $l = 1, 2, \ldots, N$. In order to compare the exact theory and the HP0 approximation, it is useful to explicit the expansion up to second order in the normalized Ising coupling $\mu = \frac{J}{\omega_0}$ of the single-particle energies $E_{F,k}$ and $E_{B,k}$

$$\begin{aligned} \frac{E_{F,k}}{\hbar\omega_0} &\approx 1 + 2\cos k\,\mu + 2\sin^2 k\,\mu^2, \\ \frac{E_{B,k}}{\hbar\omega_0} &\approx 1 + 2\cos k\,\mu - 2\cos^2 k\,\mu^2, \end{aligned} \tag{3.12}$$

noticing that the HP0 approximation leads to incorrect results at the second order in μ.

3.2.2 Beyond HP0 approximation: first-order Holstein-Primakoff approximation

In order to bridge the gap between the results in the exact fermionic and bosonic pictures, here we include higher-order terms of the Holstein-Primakoff expansion, obtaining in the Hamiltonian non-linear terms composed of an even number of $\hat{b}_n$ and $\hat{b}^\dagger_n$ operators. We introduce a novel approach to recover a quadratic bosonic Hamiltonian starting from these non-linear terms. This method is in principle applicable to all the orders, but we only consider

the first-order nonlinear terms in the Holstein-Primakoff transformations, as they already lead to correct results for the single-particle energies at the order μ^2. We thus apply the transformation

$$\begin{aligned} \hat{\sigma}_n^+ &= \hat{b}_n^\dagger \left(1 - \frac{\hat{b}_n^\dagger \hat{b}_n}{2}\right), \\ \hat{\sigma}_n^- &= \left(1 - \frac{\hat{b}_n^\dagger \hat{b}_n}{2}\right) \hat{b}_n, \end{aligned} \tag{3.13}$$

which we now refer to as first-order Holstein-Primakoff approximation (HP1). By using Eqs.3.13, the Hamiltonian of Eq.3.1 can be written as

$$\hat{H}_M = \hat{H}_M^{(0)} + \hat{H}_M^{(1)}, \tag{3.14}$$

where $\hat{H}_M^{(0)}$ is shown in Eq. 3.8 and the nonlinear part is

$$\hat{H}_M^{(1)} = -\frac{\hbar J}{2} \sum_{n=1}^{N-1} \hat{b}_n^\dagger \Big[\Big(\hat{b}_n^\dagger + \hat{b}_n \Big) \Big(\hat{b}_{n-1}^\dagger + \hat{b}_{n-1} + \hat{b}_{n+1}^\dagger + \hat{b}_{n+1} \Big) \Big] \hat{b}_n. \tag{3.15}$$

In analogy with what done for the HP0 approximation, we aim to put the Hamiltonian in the diagonal form, by introducing the bosonic operators $\hat{d}_{F,k}$, such that

$$\begin{aligned} \hat{b}_n &= \frac{1}{\sqrt{N}} \sum_k e^{ink} (\alpha_{\tilde{B},k}\, \hat{d}_{\tilde{B},k} + \beta_{\tilde{B},k}\, \hat{d}_{\tilde{B},-k}^\dagger), \\ \hat{b}_n^\dagger &= \frac{1}{\sqrt{N}} \sum_k e^{-ink} (\beta_{\tilde{B},k}\, \hat{d}_{\tilde{B},-k} + \alpha_{\tilde{B},k}\, \hat{d}_{\tilde{B},k}^\dagger), \end{aligned} \tag{3.16}$$

where $\alpha_{\tilde{B},k}$ and $\beta_{\tilde{B},k}$ are called Hopfield coefficients. They can always been chosen real and must satisfy the relation $\alpha_{\tilde{B},k}^2 - \beta_{\tilde{B},k}^2 = 1$ to preserve the bosonic nature of operators. Determining their values means solving the eigenvalues problem. Let us notice that Eq. 3.16 exactly diagonalises the Hamiltonian to the chosen order in the single-particle subspace, since, given $|\tilde{G}\rangle$ the ground state of the quadratic part, all the normally-ordered remaining nonlinear terms annihilate both $|\tilde{G}\rangle$ and the single-particle states $\hat{d}_{F,k}^\dagger |\tilde{G}\rangle$. By applying Eq. 3.16 to Eq. 3.14, normal ordering all the terms, and keeping

only terms up to the second order, we obtain

$$\begin{aligned}\hat{H}'_M &= \sum_k \hbar\Big[\mathcal{A}_k - \frac{J}{2}\sum_{k'} f(k,k')\Big]\hat{d}^\dagger_{\tilde{B},k}\hat{d}_{\tilde{B},k} \\ &+ \sum_k \hbar\Big[\mathcal{B}_k - \frac{J}{2}\sum_{k'} g(k,k')\Big]\Big(\hat{d}^\dagger_{\tilde{B},k}\,\hat{d}^\dagger_{\tilde{B},-k} + \hat{d}_{\tilde{B},k}\,\hat{d}_{\tilde{B},-k}\Big) \\ &+ \sum_k \hbar\Big[\mathcal{C}_k - \frac{J}{2}\sum_{k'} h(k,k')\Big]. \end{aligned} \tag{3.17}$$

The analytical expression for all the coefficients can be found in A.2. The set of nonlinear equations derived by imposing that the non-diagonal terms of the Hamiltonian have to be zero, could be solved numerically. Nevertheless in the following we will present a perturbative approach of the order μ^2, allowing us to derive analytic expressions to be compared to those obtained by the exact case and HP0 approximations. Diagonalising the Hamiltonian is thus equivalent to solve the set of equations

$$\mathcal{B}_k - \frac{J}{2}\sum_{k'} g(k,k') = 0, \quad \forall k, \tag{3.18}$$

which can be done analytically expanding the coefficients $\alpha_{\tilde{B},k}$ and $\beta_{\tilde{B},k}$ up to the second order in μ. Following such a procedure, detailed in A.2, we obtain

$$\begin{aligned}\alpha_{\tilde{B},k} &\approx 1 + \frac{\cos^2 k}{2}\,\mu^2, \\ \beta_{\tilde{B},k} &\approx -\cos k\,\mu + \Big(2\cos^2 k - \frac{1}{2}\Big)\,\mu^2, \end{aligned} \tag{3.19}$$

resulting in single-particle energies

$$\frac{E_{\tilde{B},k}}{\hbar\omega_0} \approx 1 + 2\cos k\,\mu + 2\sin^2 k\,\mu^2, \tag{3.20}$$

which, to the considered order, coincide with the single-particle energies of the exact case in Eq. 3.12. This result shows the success of our novel approach to recover an accurate spectrum although within a bosonic description.

Fig. 3.2 shows the normalised single-particle energies $E_{F,k}/\hbar\omega_0$ (solid blue line), $E_{B,k}/\hbar\omega_0$ (dashed red line), and $E_{\tilde{B},k}/\hbar\omega_0$ (dotted green line) calculated

as a function of $|\mu|$ for the first excited mode, which, in the thermodynamic limit, corresponds to $k \to 0$. It can be observed that, while for weak values of μ the three curves overlap, when the coupling strength J becomes a significant fraction of ω_0 the HP0 approximation presents a significant deviation from the exact theory. On the contrary, the HP1 approximation is in very good agreement with the exact theory.

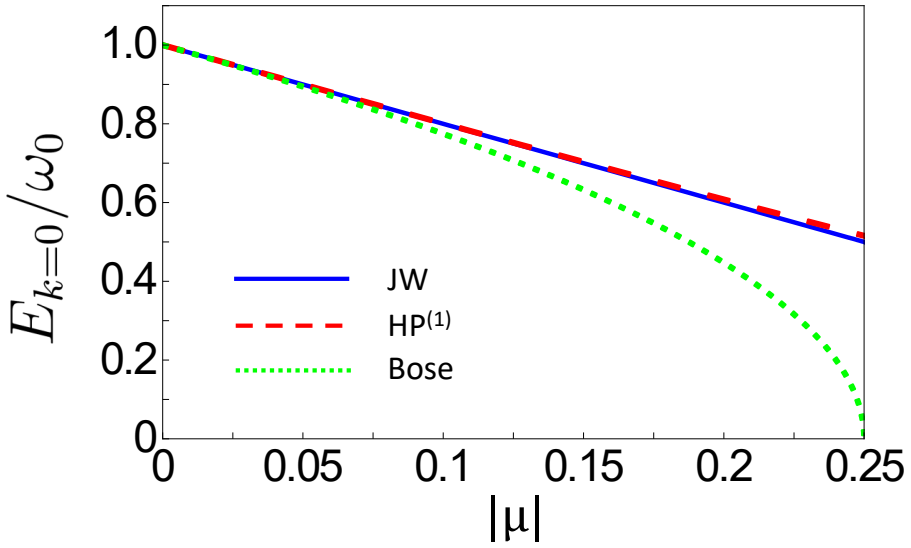

Figure 3.2: Single-particle energies for $k = 0$ obtained as a function of the normalised Ising coupling strength $|\mu|$ ($\hbar = 1$). Shown are the results obtained with the exact theory (solid blue line), the HP0 approximation (dotted green line) and the HP1 approximation (dashed red line).

It is possible also to study the dependence of the single-particle energies upon the number N of dipoles. In Fig. 3.3 the first two excited states (corresponding to $l = 1$ and $l = 2$, where l is the mode index from Eq. 3.11) are displayed as a function of the chain length N for (a) $\mu = -0.05$ and (b) $\mu = -0.2$. Given the results for the exact theory (Eq. 3.4),it can be observed that the HP0 approximation (Eq. 3.10) gives good results only for weak couplings, while the results obtained by applying the HP1 approximation (Eq. 3.20) are robust also for large values $|\mu|$.

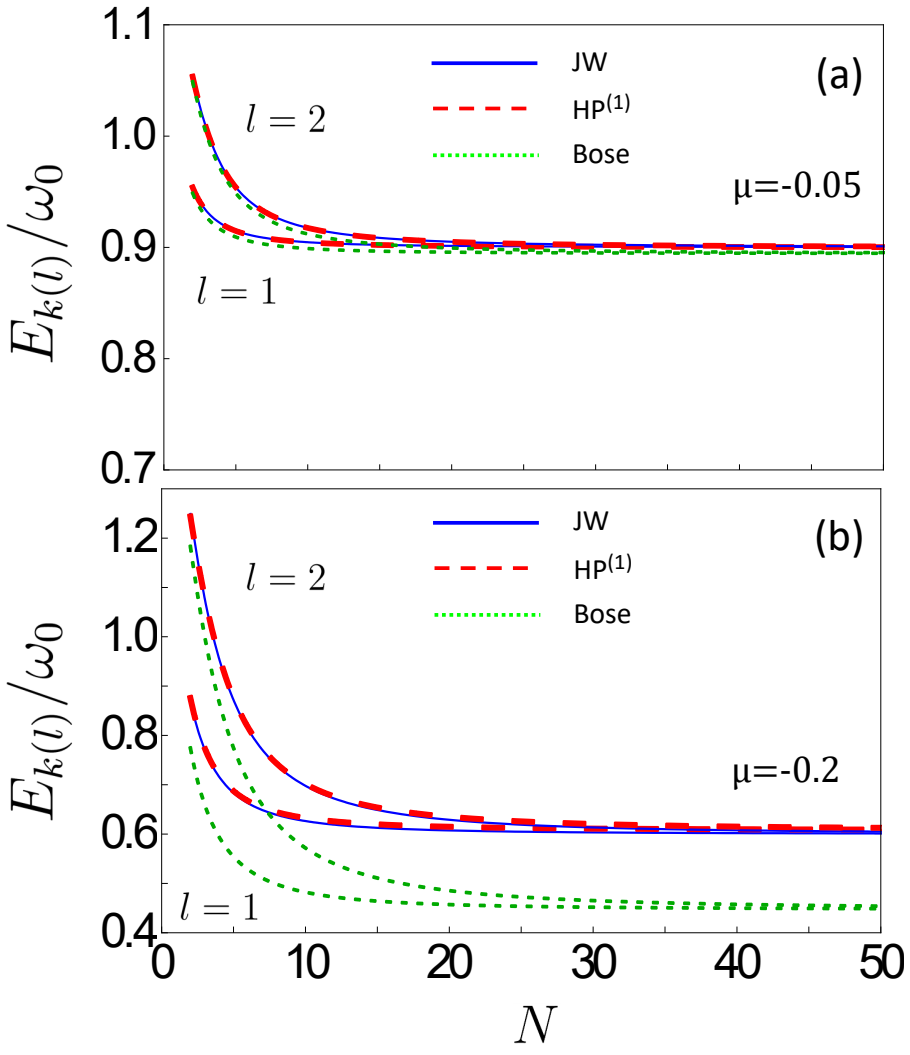

Figure 3.3: First two excited states $E_{k(l=1)}$ and $E_{k(l=2)}$ as a function of the chain length N for two different values of the normalised coupling strength ($\hbar = 1$): (a) $\mu = -0.05$ and (b) $\mu = -0.2$. Shown are the results obtained with the exact theory (solid blue line), the HP0 approximation (dotted green line) and the HP1 approximation (dashed red line).

3.3 The Dicke-Ising Hamiltonian

In order to determine the polariton spectrum of a one-dimensional Ising chain of N dipoles coupled to a cavity photonic field and investigate the interplay

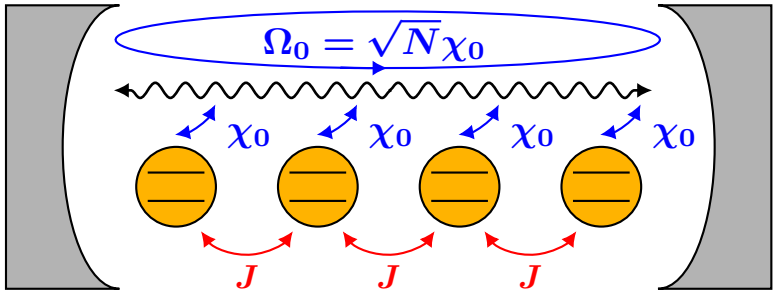

Figure 3.4: The same chain of in Fig.3.1 coupled to a cavity photonic field through a single-dipole light-matter resonant coupling χ_0 and collective coupling $\Omega_0 = \sqrt{N}\chi_0$.

between the Ising coupling and the light-matter coupling, we need to solve the Dicke-Ising Hamiltonian, which includes both a Ising-type inter-dipole and a light-matter interaction terms. It has been already mentioned that the exact fermionic formulation cannot be applied as not compatible with the bosonic nature of the polariton modes at diluite regime. The overall system can be described by the Dicke-Ising Hamiltonian

$$\hat{H}_{DI} = \hat{H}_C + \hat{H}_M + \hat{H}_I + \hat{H}_D, \tag{3.21}$$

with

$$\hat{H}_C = \sum_k \hbar\omega_k \, \hat{a}_k^\dagger \hat{a}_k, \tag{3.22}$$

$$\hat{H}_I = \sum_{n=1}^{N} \sum_k \hbar\chi_k \, (\hat{a}_k e^{ink} - \hat{a}_k^\dagger e^{-ink})(\hat{\sigma}_n^- - \hat{\sigma}_n^+), \tag{3.23}$$

$$\hat{H}_D = \sum_k \hbar D_k (\hat{a}_k^\dagger + \hat{a}_{-k})(\hat{a}_{-k}^\dagger + \hat{a}_k), \tag{3.24}$$

where $\hat{H}_C$ is the bare Hamiltonian of the cavity modes of frequencies $\omega_k = ck/L$, with bosonic annihilation and creation operators $\hat{a}_k$ and $\hat{a}_k^\dagger$, $\hat{H}_M$ is as in Eq. 3.1, $\hat{H}_I$ describes the interaction between the photonic modes and the dipoles, weighted by the single-dipole light-matter coupling $\chi_k = \chi_0\sqrt{\omega_0/\omega_k}$

with χ_0 the resonant coupling, and $\hat{H}_D$ is the diamagnetic term. Assuming the transition to saturate the TRK sum rule [45], $D_k = \Omega_0^2/\omega_k$ with $\Omega_0 = \sqrt{N}\chi_0$ the collective light-matter coupling. As usual, the diamagnetic term $\hat{H}_D$ can be removed by a Bogoliubov rotation, which leads to the renormalised cavity frequency $\tilde{\omega}_k \equiv \sqrt{\omega_k^2 + 4\Omega_0^2}$ and collective light-matter coupling $\tilde{\Omega}_k \equiv \Omega_0\sqrt{\omega_0/\tilde{\omega}_k}$. The Ising chain, assumed to have lattice constant a, creates a folding of the photonic dispersion on the border of the first Brillouin zone $\omega_{\mathrm{BZ}} = c\pi/a$. A matter mode of the Ising chain indexed by the quasi-momentum k would thus a priori couple with an infinity of photonic modes with wavevector differing by an integer multiple of π/a. In the following we will assume $\omega_{\mathrm{BZ}} - \omega_0 \gg \Omega_0$ and neglect Umklapp processes, that is we will assume that the photonic energy on the border of the first Brillouin zone is completely detuned from the dipolar transitions.

3.3.1 Polariton spectrum in HP0 approximation

We calculate and compare the polariton eigenenergies of $\hat{H}_{DI}$ at several orders of approximation. Initially, we diagonalise $\hat{H}_M$ in terms of bosonic operators $\hat{d}_{O,k}$, where $O \in [B, \tilde{B}]$ indicates either the HP0 or the HP1 approximations, but we do not consider nonlinear terms originating from the light-matter interaction Hamiltonian in Eq. 3.23, effectively treating $\hat{H}_I$ in the HP0 approximation. In the next subsection, we will drop this approximation and expand the HP1 approximation to the full Dicke-Ising Hamiltonian. By applying the Hopfield-Bogoliubov transformations

$$\begin{aligned} \hat{b}_n &= \frac{1}{\sqrt{N}} \sum_k e^{ink}(\alpha_{O,k}\, \hat{d}_{O,k} + \beta_{O,k}\, \hat{d}^\dagger_{O,-k}), \\ \hat{b}^\dagger_n &= \frac{1}{\sqrt{N}} \sum_k e^{-ink}(\beta_{O,k}\, \hat{d}_{O,-k} + \alpha_{O,k}\, \hat{d}^\dagger_{O,k}), \end{aligned} \tag{3.25}$$

where $\hat{d}_{O,k}$ and $\hat{d}^\dagger_{O,k}$ are generic bosonic operators which make $\hat{H}_M$ diagonal, and $\alpha_{O,k}$ and $\beta_{O,k}$ are the generic Hopfield coefficients of the transformations (they can be found in A.2), the total Hamiltonian $\hat{H}$ can be written as:

$$\begin{aligned} \hat{H} &= \sum_k \hbar\tilde{\omega}_k\, \hat{a}^\dagger_k \hat{a}_k + \sum_k E_{O,k} \hat{d}^\dagger_{O,k} \hat{d}_{O,k} + E^0_O + \\ &\quad \sum_k \hbar\Lambda_{O,k}\, (\hat{a}_{-k} - \hat{a}^\dagger_k)(\hat{d}_{O,k} - \hat{d}^\dagger_{O,-k}). \end{aligned} \tag{3.26}$$

$E_{O,k}$ in Eq. 3.26 is the single-particle energy, E_O^0 the matter ground-state energy, and

$$\Lambda_{O,k} \equiv \tilde{\Omega}_k F_{O,k}, \tag{3.27}$$

is the effective light-matter coupling, with $F_{O,k} \equiv \alpha_{O,k} - \beta_{O,k}$. The function $F_{O,k}$, depending upon μ, represents the contribute of the Ising interaction to the effective light-matter coupling $\Lambda_{O,k}$.

The Hamiltonian $\hat{H}$ can be now diagonalised by Hopfield approach, by mapping the bosonic operators $\hat{a}_k$ and $\hat{d}_k$ into the lower and upper polariton operators $\hat{p}_{-,k}$ and $\hat{p}_{+,k}$. The Dicke-Ising Hamiltonian takes then the diagonal form

$$\hat{H} = \sum_k \left(E_{O,k}^- \hat{p}_{-,k}^\dagger \hat{p}_{-,k} + E_{O,k}^+ \hat{p}_{+,k}^\dagger \hat{p}_{+,k} \right) + E_O^G, \tag{3.28}$$

where

$$E_O^G = \sum_k \left(E_{O,k}^- + E_{O,k}^+ - \tilde{\omega}_k - E_{O,k} \right) + E_O^0, \tag{3.29}$$

is the ground-state energy of the coupled system. The polariton energies $E_{O,k}^-$ and $E_{O,k}^+$ are given by the expression

$$E_{O,k}^\pm = \frac{\hbar}{\sqrt{2}} \left[\tilde{\omega}_k^2 + E_{O,k}^2 \pm \Delta_k \right]^{\frac{1}{2}}, \tag{3.30}$$

with $\Delta_k = \left[(\tilde{\omega}_k^2 - E_{O,k}^2)^2 + 16 \Lambda_{O,k}^2 \, \tilde{\omega}_k \, E_{O,k} \right]^{\frac{1}{2}}$. Details of the calculation can be found in A.3.

Treating the matter Hamiltonian in either of the two approximations leads to different polariton energies, which, given the example of the Ising chain, will differ by level of accuracy. In the following paragraph, we present the specific results for the two cases of the Ising Hamiltonian within HP0 approximation ($O = B$) and within the HP1 approximation ($O = \tilde{B}$). Without loss of generality, we will consider $\omega_k > \omega_0$.

HP0 approximation case In this case we assume $O = B$, then the single-particle energy $E_{B,k}$ is given by Eq. 3.10 and the expressions of coefficients $\alpha_{B,k}$ and $\beta_{B,k}$ can be found in A.2.

The lower and upper polariton energies in Eq. 3.30, expanded up to the second order with respect to the normalised Ising coupling μ and the collective light-matter coupling $\eta \equiv \Omega_0/\omega_0$ take then the form

$$\begin{aligned} \frac{E^+_{B,k}}{\hbar\omega_0} &\approx \frac{\omega_k}{\omega_0} + \frac{2\omega_0\omega_k\eta^2}{\omega_k^2 - \omega_0^2}, \\ \frac{E^-_{B,k}}{\hbar\omega_0} &\approx 1 + 2\mu\cos k - 2\mu^2\cos k^2 - \frac{2\omega_0^2\eta^2}{\omega_k^2 - \omega_0^2}. \end{aligned} \tag{3.31}$$

HP1 approximation We now consider the case in which the matter Hamiltonian is diagonalised within the HP1 approximation, so that $E_{O,k} = E_{\tilde{B},k}$ with $E_{\tilde{B},k}$ from Eq. (3.20) and the coefficients of the transformations are $\alpha_{\tilde{B},k}$ and $\beta_{\tilde{B},k}$, given in Eq. 3.19. The second-order expansions with respect to the normalised coupling strengths μ and η of the polariton energies are thus given by the expressions

$$\begin{aligned} \frac{E^+_{\tilde{B},k}}{\hbar\omega_0} &\approx \frac{\omega_k}{\omega_0} + \frac{2\omega_0\omega_k\eta^2}{\omega_k^2 - \omega_0^2}, \\ \frac{E^-_{\tilde{B},k}}{\hbar\omega_0} &\approx 1 + 2\mu\cos k + 2\mu^2\sin k^2 - \frac{2\omega_0^2\eta^2}{\omega_k^2 - \omega_0^2}. \end{aligned} \tag{3.32}$$

By comparing Eqs. 3.32 to Eqs. 3.31, we can notice a difference in the expansion of the lower polariton energy only in the term at the second-order in the Ising coupling μ. This deviation corresponds exactly to the discrepancy between the single-particle energies of the Ising chain in the two approximations. This was expected, as no non-linear terms are so far considered for the light-matter interaction.

3.3.2 HP1 approximation of the Dicke-Ising Hamiltonian

We considered so far the light-matter interaction Hamiltonian $\hat{H}_I$ in HP0 approximation, that is neglecting its nonlinear terms.

As in the case of the Ising chain we proved that going beyond the HP0 approximation gives relevant improvements to the exciton spectrum, in order to verify the accuracy of the polariton energies in Eq. 3.32 for large values of the normalised coupling strengths μ and η, we now include in $\hat{H}_I$

the fourth-order nonlinear terms arising from the first Holstein-Primakoff approximation, which means using Eq. 3.13 in Eq. 3.23. The procedure leads to a light-matter interaction Hamiltonian $\hat{H}_I$ of the form

$$\hat{H}_I = \hat{H}_I^{(0)} + \hat{H}_I^{(1)}, \tag{3.33}$$

with

$$\hat{H}_I^{(0)} = \hbar\chi_0 \sum_{n=1}^{N} \sum_k \sqrt{\frac{\omega_0}{\tilde{\omega}_k}} (\hat{a}_k e^{ikn} - \hat{a}_k^\dagger e^{-ikn})(\hat{b}_n - \hat{b}_n^\dagger), \tag{3.34}$$

and

$$\hat{H}_I^{(1)} = -\frac{\hbar\chi_0}{2} \sum_{n=1}^{N} \sum_k \sqrt{\frac{\omega_0}{\tilde{\omega}_k}} (\hat{a}_k e^{ikn} - \hat{a}_k^\dagger e^{-ikn}) \hat{b}_n^\dagger (\hat{b}_n - \hat{b}_n^\dagger) b_n. \tag{3.35}$$

The new polariton energies, up to the second order in the normalised couplings μ and η, are

$$\begin{aligned} \frac{E_{\check{B},k}^+}{\hbar\omega_0} &\approx \frac{\omega_k}{\omega_0} + \frac{2\omega_0\omega_k\eta^2}{\omega_k^2 - \omega_0^2}, \\ \frac{E_{\check{B},k}^-}{\hbar\omega_0} &\approx 1 + 2\mu\cos k + 2\mu^2 \sin k^2 - \eta^2 \left(\frac{2\omega_0^2}{\omega_k^2 - \omega_0^2} - \mathcal{F}(N) \right). \end{aligned} \tag{3.36}$$

Details about the diagonalisation procedure and the Hopfield coefficients can be found in A.4. Comparing Eq. 3.36 to Eq. 3.32 we see that the effect of the nonlinear light-matter interaction Hamiltonian $\hat{H}_I^{(1)}$ is only contained in the term

$$\mathcal{F}(N) = \sum_{k'} \frac{1}{N} \frac{\omega_0^2}{2\omega_{k'}(1 + \omega_{k'})}. \tag{3.37}$$

In the large N limit, by substituting the sum in Eq. C.8 with an integral, it is found that

$$\mathcal{F}(N) = \frac{\omega_0 L}{2c\pi N} \log \frac{N\left(\omega_0 + \frac{c\pi}{L}\right)}{\omega_0 + N\frac{c\pi}{L}}, \tag{3.38}$$

which vanishes in the thermodynamic limit $N \to \infty$ with finite L. This means that nonlinear terms in the light-matter interaction can safely be

neglected in the considered order and in the dilute limit. In the case of a finite number N of dipoles, $\mathcal{F}(N)$ can assume a finite value, giving a non-negligible contribution to the lower polariton energy. By defining the cavity dispersion slope as $\delta \equiv \omega_{BZ}/\omega_0$ such a function can be written in terms of the new parameter as

$$\mathcal{F}(N) = \frac{1}{2\delta} \log \frac{N+\delta}{1+\delta}, \tag{3.39}$$

from which we see that also for finite values of N, $\mathcal{F}(N)$ vanishes in the regime $\delta \to \infty$.

3.3.3 Quantum phase transitions and saturation effects

As mentioned in the previous chapter, the Dicke Hamiltonian presents a superradiant quantum phase transition, unless the diamagnetic term is included. In this case, indeed, it would occur only when $D_k < \frac{\Omega_0^2}{\omega_0}$, which is exactly the parameter range excluded by the TRK sum rule [45, 46]. As the Ising coupling modifies both the matter modes energies and their coupling to the photonic field, it is reasonable to wonder whether the transformed Hamiltonian in Eq. 3.26 still does not undergo any phase transition. A quantum phase transition cannot happen unless the frequency of one of the polariton eigenmodes vanishes. By requiring that the lower polariton energy $E^-_{O,k}$ never crosses zero, we obtain the condition on the effective light-matter coupling $\Lambda_{O,k}$

$$\Lambda_{O,k} \neq \pm \frac{\sqrt{\tilde{\omega}_k E_{O,k}}}{2}, \tag{3.40}$$

which leads to the inequality

$$F_{O,k} \leq \sqrt{\frac{E_{O,k}}{\omega_0}}, \tag{3.41}$$

always satisfied both for the HP0 and the HP1 approximations. This demonstrates that the no-go theorems regarding the absence of phase transitions in the Dicke model extend also the the Dicke-Ising model in the HP1 approximation. It is interesting to notice that the inequality in Eq. 3.41 is saturated only for the full HP0 approximation, that is for $F_{O,k} = F_{B,k}$, whereas using the HP1 approximation, $F_{\tilde{B},k}$ is smaller than $F_{B,k}$ of a finite

quantity $\mu^2/2$. Since, in general, the effective light-matter coupling is defined as $\Lambda_{O,k} = \tilde{\Omega}_k F_{O,k}$, and the average number of virtual matter excitations $\mathcal{N}$ in the ground-state $|G\rangle$ of the Ising Hamiltonian to the second order in the normalised dipole-dipole coupling is

$$\mathcal{N} \equiv \langle G| \sum_n \hat{b}_n^\dagger \hat{b}_n^\dagger |G\rangle = \frac{\mu^2}{2} + O(\mu^3), \tag{3.42}$$

we find that, within a second-order expansion in μ,

$$\Lambda_{\tilde{B},k} = \Lambda_{B,k} \left(1 - \mathcal{N}\right). \tag{3.43}$$

The reduction of the effective light-matter coupling in the HP1 approximation can be interpreted as a saturation effect of the transition due to the presence of ground-state virtual excitations, an example of the vacuum nonlinear effects which have recently been investigated in different systems [69, 70].

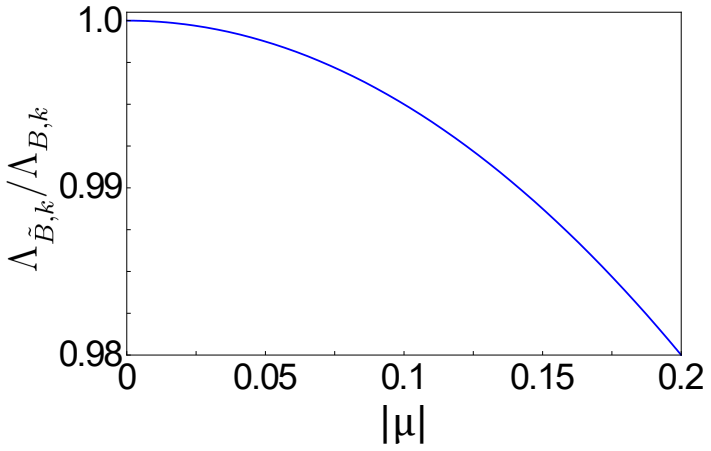

Figure 3.5: The effective coupling $\Lambda_{\tilde{B},k}$ normalised with respect to the full HP0 $\Lambda_{B,k}$ one as a function of the absolute value of μ.

In Fig.3.5 we show the behaviour of the effective light-matter coupling $\Lambda_{\tilde{B},k}$ as a function of μ. Within the range $0 \leq |\mu| \leq 0.2$, the presence of the virtual photons causes a small but evident reduction of $\sim 2\%$ respect to the value predicted by the full HP0 approximation $\Lambda_{B,k}$.

Unfortunately, although this shift could be in principle observable within present experimental set-ups, realistic spectral linewidths would not allow

yet to resolve it. However, our novel approach results to be suitable for theoretically describing the saturation effects which arise when the interaction becomes strong enough to observe a finite population of virtual excitations in the ground state.

3.3.4 Quantitative Comparison

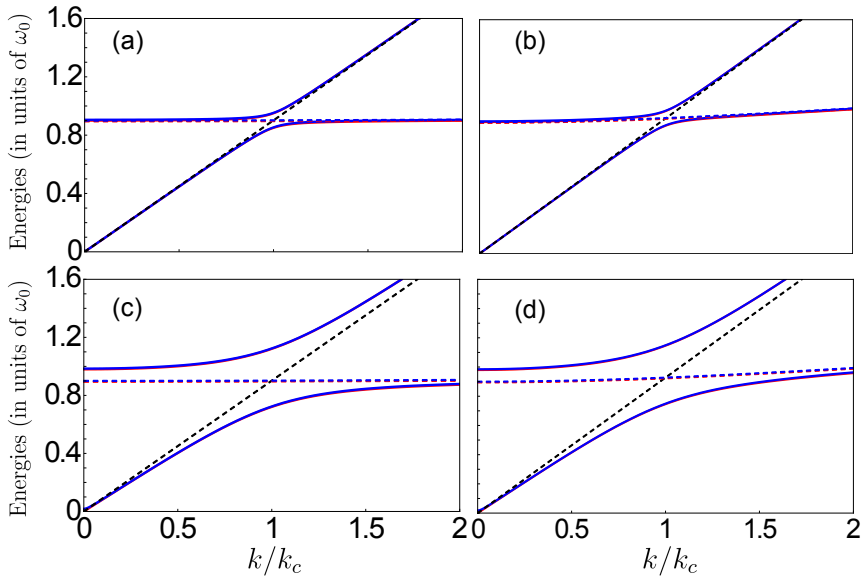

Figure 3.6: (Color online) Lower and upper polaritons obtained by full HP0 treatment (red solid line) and HP1 approximation (blue solid line) for $\mu = -0.05$, as a function of the normalised wavevector k/k_c, with k_c the crossing point coordinate. The linear cavity dispersion (black dashed line) and the exciton energies for both the HP0 (red dashed line) and first-order Holstein-Primakoff (blue dashed line) approximation are shown. The plots display cavity dispersion slopes $\delta = 4$ in panels (a) and (c), and $\delta = 16$ in panels (b) and (d), and normalised light-matter coupling $\eta = 0.05$ in (a) and (b), and $\eta = 0.2$ in (c) and (d)

.

Figs 3.6 and 3.7 show the dispersive behaviour in the thermodynamic limit of the lower and upper polaritons for both full HP0, $E^{\pm}_{B,k}$ (red line), and HP1 approximation, $E^{\pm}_{\tilde{B},k}$ (blue line), for different Ising and light-matter

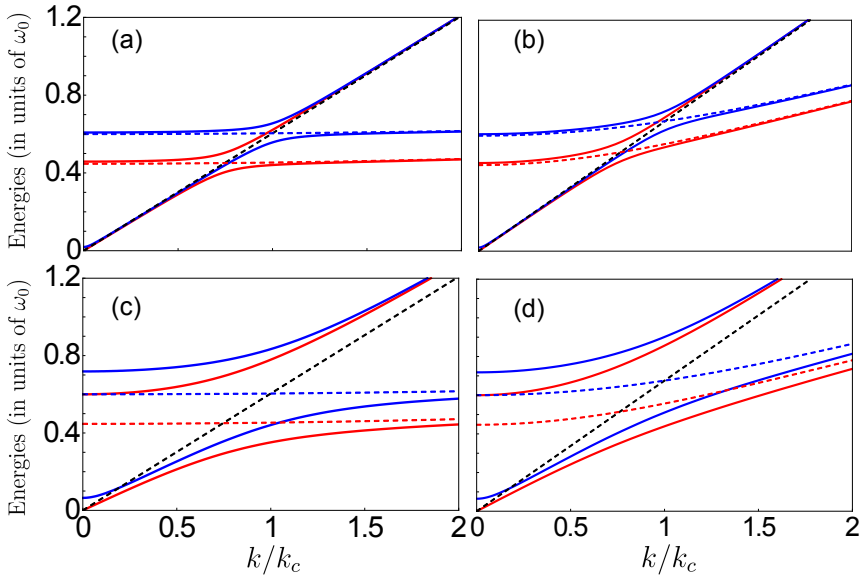

Figure 3.7: (Color online) Lower and upper polaritons obtained by full HP0 treatment (red solid line) and HP1 approximation (blue solid line) for $\mu = -0.2$, as a function of the normalised wavevector k/k_c, with k_c the crossing point coordinate. Parameters are the same as in Fig. 3.5.

coupling strengths, and for different slopes of the cavity linear dispersion δ (black dashed line). Figure 3.6 refers to a small normalised Ising coupling $\mu = -0.05$ and both the top panels (a) and (b) correspond to normalised light-matter coupling $\eta = 0.05$. The bottom panels (c) and (d) show, instead, the case of ultrastrong light-matter regime, with $\eta = 0.2$, displaying a sensitive increasing of the splitting between the two polariton energies. The left side panels (a) and (c) differ from the right side panels (b) and (d) for the slope of the cavity frequency. The left panels display a dispersion with $\delta = 4$, while the right panels correspond to $\delta = 16$. In Fig. 3.6 the energies of the different approximations perfectly overlap for such low value of the Ising coupling. In Fig. 3.7 a remarkable shift is instead visible, with same parameters as Fig. 3.6 but a value of the Ising interaction $\mu = -0.2$. In the thermodynamic limit the main effect of going beyond the HP0 approximation, at least at the second order in the coupling strengths, is thus a shift between the exciton energies $E_{\tilde{B},k}$ (blue dashed line) and $E_{B,k}$ (red dashed line).

3.4 Conclusions

In conclusion, we developed a solid approach to diagonalise the Ising Hamiltonian in transverse field in terms of bosonic excitations for arbitrary values of the Ising coupling, until the onset of the ferromagnetic phase transition. We then applied such an approach to the Dicke-Ising Hamiltonian, showing how the Ising interaction modifies the usual polaritonic excitations of the Dicke model. This Chapter highlighted a crucial difference between the Dicke and the Ising models in the regime of large couplings: while in the Dicke model the density of ground-state virtual excitations vanishes in the $N \to \infty$ limit, confirming the validity of a bosonic Hopfield approach in the dilute regime, the same quantity resulted finite in the Ising case. This ground-state population effectively saturates the transition, causing a reduction of the oscillator strength. Such an example of ground-state non-linearity, while comparatively small, could be spectroscopically resolved in setups in which the number of dipoles can be controllably modified. The model we develop could in particular be implemented in state-of-the-art superconducting circuit QED systems, in which chains of thousand of qubits with engineered interactions have recently been realised.

This study also aims to provide a new useful methodological tool for investigating nonlinear effects arising from detailing the inner structure and interactions of more complex many body light-matter coupled systems, which cannot be revealed by a mere multi-mode Hopfield model.

Chapter 4

Cavity-induced control of orientational degrees of freedom in a molecular ensamble

4.1 Introduction

In the last decades, SC has been object of great interest not only for its implications of fundamental nature, but also for a promising number of applications, both in molecular and solid-state physics. Among the wide range of suitable materials, organic molecular aggregates resulted to be good candidates for the investigation of SC phenomena for their unusually large transition dipole moment [71, 72, 73], and because of their important applications in biological and medical science. When the electronic transitions of these molecules are coherently coupled to the same cavity mode, the effective light-matter coupling is collectively enhanced by a the square root of the number of molecules involved in the SC process, leading to normal energy modes known as *polaritons* (see Sec. 2.3.2). Changing the molecular density of the system means thus tuning their effective interaction strength.

It has been theoretically and experimentally shown that SC regime in organic molecular ensambles can induce modifications of their chemical properties, leading to activation, triggering and suppression of photochemical reactions [27, 36, 74]. When an organic molecule is places into a cavity, its

ground and first excited-state potential energy surfaces (PESs) are coupled by the exchange of cavity photons. The uncoupled PESs exihibit certain equilibrium positions, which determine the chemical properties of the molecule. Where the bare excited PES crosses the bare ground PES, blue-shifted by the photon energy, the strong coupling opens one or more Rabi splittings, whose amplitudes depend on the coupling strength. It follows that the coupled PESs are deformed and acquire new energy minima, leading to significantly different chemical properties. When N molecules are coherently coupled to the same cavity mode, Rabi splitting occurring between the N-dimensional PESs will depend on the collective coupling strength [74]. It has been showed that the collective nature of the light-matter coupling does not reduce its influence on each single molecule, but it even enhances SC induced effects. Further theoretical works have investigated cavity-induced phenomena as a tool to significantly modify not only the optical response of molecular ensambles, but also its internal degrees of freedom. The fundamental idea is that the coupling of a single molecule to a cavity field is influenced by the state of its microscopic degrees of freedom, such as its orientation or vibrational state. For instance, if a molecule has a dipole moment which is on the same direction as the electric field vector of the fundamental cavity mode, the light-matter coupling will be maximum. Since the light-matter coupling tends to minimize the total energy of the system, which is determined by collective phenomena, each molecule will feel an optomechanical force acting upon its internal microscopic state, favoring that one which makes the coupling strength as large as possible. This phenomenon can be also see as a self-adaptation process of the molecular ensamble, as effects of the SC [33]. In most cases the light-matter strength of a single molecule χ is much smaller than the thermal energy of the system, while the collectively enhanced coupling $\Omega = \chi\sqrt{N}$, with N number of molecules, is usually large enough to defeat the thermal fluctuations. Whether the cavity-induced adaptation for the state of the microscopic degrees of freedom has an energy landscape which scales as the single-molecule or the collective coupling, determines if these effects are experimentally observable or not.

This matter has been investigated by several works [29, 27]. In particular, we highlight two theoretical works investigating the effects of SC on underlying degrees of freedom. [31] studies the modification of the molecular ground state bond length in the USC regime. [33] investigates, instead, the SC effects on vibrational and rotational states of coupled organic molecules, due to the molecular self-adaptation. In both the works, it is demonstrated

that, while observables depending on the polariton energies depend on the collective coupling Ω, the effects influencing the internal degrees of freedom of the individual molecules scale as the single coupling χ. This is easy to see if we consider to switch the state of one single molecule among a number N of molecules all coupled to the same cavity mode of frequency ω_c. By assuming the resonant case and a normalised coupling $\frac{\Omega}{\omega_c} \ll 1$, the energy of the lowest coupled mode would be

$$\hbar\omega_- = \hbar\sqrt{\omega_c^2 + 4\Omega} \approx \omega_c - \Omega. \tag{4.1}$$

When one single molecule switches its internal state, this energy shifts by

$$\frac{d\omega_-}{dN} \approx \frac{d\Omega}{dN} = \frac{\chi}{\sqrt{N}}. \tag{4.2}$$

As we can see, the variation in energy scales as the single-molecule coupling, suggesting that the energy landscape governing the single-molecule internal state is usually overcome by the thermal energy.

We demonstrate that this conclusion can be overturned in highly excited systems, where a non negligible polariton density $s = \frac{M}{N}$, with M the number of polaritons, is present. In this case the energy of the system in which all the M polaritons are in their lowest energy and no saturation is considered, results

$$M\omega_- \approx M\left(\omega_c - \Omega\right), \tag{4.3}$$

and its variation as one molecule turns its microscopic state is

$$M\frac{d\omega_-}{dN} \approx M\frac{\chi}{\sqrt{N}} = s\Omega \tag{4.4}$$

. This time this shift scales as the collective coupling strength, likely exceeding the thermal fluctuations, leading to potentially visible effects.

The quantum system here investigated consists of a set of N rotating two-dimensional molecular dipoles identically coupled to a single resonant cavity mode. This simplified model can describe a system of phobic molecules floating upon the surface of a solvent in an optical open cavity. For sake of simplicity, we consider the rotational degrees of freedom to be classical and adiabatic, and as such the orientation of the different dipoles to be described by classical coordinates and with no kinetic energy associated. In realistic experiments, this condition could be addressed by the employment of a viscous dissipative solvent.

Regarding the cavity-single-mode assumption, a specific photon mode can be selected, for instance, by using elliptic mirrors, leading to a resolvable polarization splitting (Fig. 4.1(a)). We here investigate the effects of SC upon the molecules' orientational degrees of freedom, by evaluating the average angular configuration as a function of the excitation density s and temperature. We arrive to demonstrate that the collective coupling drives the overall configuration of the dipolar ensamble to pass from an isotropic phase to a complete alignment.

4.2 Theoretical model

The most suitable model for the description of a set of orientable N dipoles coupled to a single cavity mode is a generalised Dicke model (Sec. 2.3.2). The electronic transition of the n-th dipole, approximated as a two-level system with transition energy $\hbar\omega_x$, is described by Pauli operators $\hat{\sigma}_n^z$, $\hat{\sigma}_n^-$, and $\hat{\sigma}_n^+$, while the cavity mode by the creation and annihilation operators $\hat{a}$ and $\hat{a}^\dagger$. The coupling strength of a single dipole is influenced by its orientation relative to the electric field direction, which, for dipoles free to rotate in plane, is determined by the angle θ_n, as pictured in Fig. 4.1(a). Since we do not now expect to observe any USC effect, apart from a shifting of the polariton eigenenergies by an amount of the order $\frac{N\chi^2}{\omega_x^2}$, usually negligible, we apply the RWA (see Sec. 2.3.2). In the resonant case, the Dicke Hamiltonian can thus be written as ($\hbar = 1$)

$$\hat{H} = \omega_x \hat{a}^\dagger \hat{a} + \sum_n \left[\frac{\omega_x}{2} \hat{\sigma}_n^z + \chi \cos\theta_n \left(\hat{a}\hat{\sigma}_n^+ + \hat{a}^\dagger \hat{\sigma}_n^- \right) \right]. \tag{4.5}$$

The Hamiltonian can be diagonalised in the one-excitation subspace recovering $N-1$ dark modes at the bare energy ω_x [75], and a pair of lower and upper polariton modes, whose frequencies $\omega_\pm$ are calculated as follows. The matrix associated to the Hamiltonian in Eq. 4.5 is

$$M = \begin{bmatrix} \omega_0 & 0 & \dots & 0 & \chi\cos(\theta_1) \\ 0 & \omega_0 & \dots & 0 & \chi\cos(\theta_2) \\ \dots & \dots & \dots & \dots & \dots \\ 0 & 0 & \dots & \omega_0 & \chi\cos(\theta_N) \\ \chi\cos(\theta_1) & \chi\cos(\theta_2) & \dots & \chi\cos(\theta_N) & \omega_0 \end{bmatrix}. \tag{4.6}$$

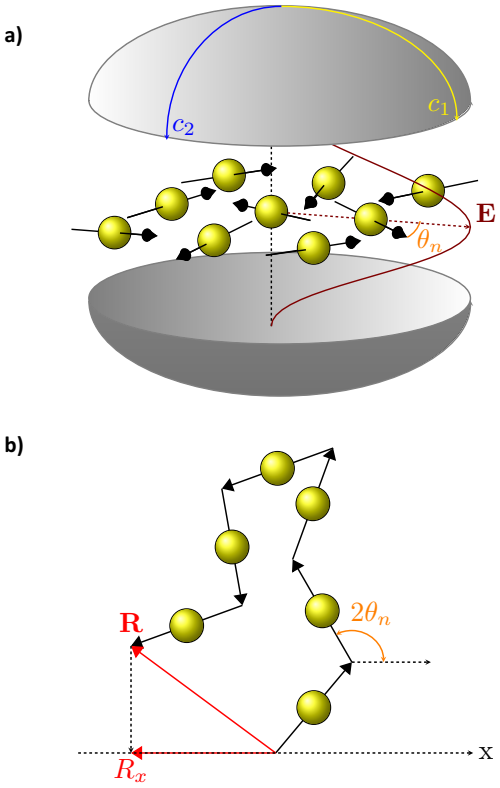

Figure 4.1: a) Sketch of the system under consideration: a set of rotating coplanar dipoles identically coupled to a single photonic cavity mode. The nth dipole forms an angle θ_n with the direction of the electric field. The cavity represented has elliptical mirrors with different curvatures along principal axis $c_1 \neq c_2$, allowing to consider a single resonant mode with well defined polarization. b) The phase space of the dipoles is equivalent to the one of a two-dimensional polymer, allowing us to calculate the relevant partition function.

Considering an eigenvector of the form $[y_n\ w]$, by shifting the energies by ω_x, for the eigenvalue frequencies ω we obtain the eigenvalues equations

$$\omega y_n - w\chi\cos(\theta_n) = 0 \tag{4.7}$$

$$\sum_n \chi\cos(\theta_n)y_n - \omega w = 0, \tag{4.8}$$

that is

$$\omega^2 y_n \;=\; \chi\cos(\theta_n)\sum_m \chi\cos(\theta_m)y_m. \tag{4.9}$$

Defining $Q=\sum_n \cos(\theta_n)y_n$, we can write

$$\omega^2 Q \;=\; \sum_n \chi^2\cos^2(\theta_n)Q, \tag{4.10}$$

which leads to

$$\omega_\pm \;=\; \omega_x \pm \chi\sqrt{\sum_{n=1}^{N}\cos^2(\theta_n)}. \tag{4.11}$$

As expected the energies of the polariton modes now depend upon all the angles θ_n. Let us point now our attention on Eq. 4.11 and on how this becomes as we consider different overall orientational configurations. For molecules fully oriented along the electric field ($\theta_n = 0\;\forall\, n$) we have

$$\omega_-^{\min} \;=\; \omega_x - \chi\sqrt{N} = \omega_x - \Omega, \tag{4.12}$$

while if the dipoles are isotropically distributed over the plane we get the higher energy

$$\omega_-^{\rm iso} \;=\; \omega_x - \chi\sqrt{\frac{N}{2}} = \omega_x - \frac{\Omega}{\sqrt{2}}. \tag{4.13}$$

If the system is in a state containing M polaritons only in the lower state, the total energy will be minimised by having all dipoles aligned, but this effect is counterbalanced by the higher entropy of non-aligned states. We have already made an argument about the energy landscape for the microscopic state of a single molecule in a highly excited system, observing that this scales as $s\Omega$. This leads us to expect that an increasing excitation density s can drive the system to undergo a crossover between the two angular configurations, with the lower polariton energy transitioning between $\omega_-^{\rm iso}$ and $\omega_-^{\min}$, with a critical temperature of $s\Omega$. In order to discover the nature of the ordering trend and to precisely identify its boundary, we calculate the partition function of the

system with M lower polaritons. Assuming the energy of such a state to be $M\omega_-$, the partition function reads

$$Z \propto \prod_{n=1}^{N} \int_0^{2\pi} d\theta_n \exp\left[M\beta\chi \sqrt{\sum_{n=1}^{N} \cos^2(\theta_n)} \right], \tag{4.14}$$

where $\beta = \frac{1}{k_B T}$ is the inverse temperature and we choose $M\omega_x$ as energy reference. In Eq. 4.14 we neglected the upper polariton mode, since we are only interested in systems that verify $\beta\Omega > 1$, as otherwise the crossover would be not observable for any realistic value of s. For instance, if we assume to reach collective coupling strengths of $\Omega = 500$meV, which have been achieved in molecular crystals [76], at room temperature, we would have $\beta\Omega = 20$. The nonlinear, collective interaction between the different dipoles in Eq. 4.14 can be put in a more manageable form by introducing N two-dimensional unit vectors $\mathbf{r}_n = [\cos(2\theta_n), \sin(2\theta_n)]$ and noticing that

$$\sum_{n=1}^{N} \cos^2(\theta_n) = \frac{N}{2} + \frac{1}{2}\sum_{n=1}^{N} \cos(2\theta_n) = \frac{N + R_x}{2}, \tag{4.15}$$

where R_x is the x component of the vector $\mathbf{R} = \sum_{n=1}^{N} \mathbf{r}_n$. This lead to identifying the set of dipoles with a two dimensional polymer made of N segments of unit lengths, sketched in Fig. 4.1(b), and rewrite the partition function as

$$Z \propto \int_{R^2} d^2\mathbf{R}\, P_N(R) \exp\left[\frac{sN\beta\chi}{\sqrt{2}} \sqrt{N + R_x} \right], \tag{4.16}$$

where $P_N(R)$ is the endpoint distribution of the two-dimensional polymer of length N. We now recognise in Eq. 4.14 an integral over the parameter space of the polymer, evolving in a potential depending on the x-projection of total length of the chain.

The exact form of the polymer's endpoint distribution can be found in [77] as

$$P_N(R) = \int_0^{\infty} dt\, t\, J(tR)\, J^N(R), \tag{4.17}$$

with J the Bessel function of order zero. Numerical evaluation of Eq.4.16 using the exact distribution of Eq. 4.17 becomes quickly impracticable for

$N \gg 1$, where instead we can apply its Gaussian approximation

$$P_N(R) \approx \frac{1}{\pi N} \exp\left(-\frac{R^2}{N}\right), \tag{4.18}$$

which is exact for $N \to \infty$ [77].

Using Eq. 4.18 into Eq. 4.16 we can evaluate the integral over R_y and, introducing the normalised coordinate $\eta = R_x/N \in [0,1]$, obtain

$$Z \;\propto\; \int_0^1 d\eta \, \mathrm{erf}\left[\sqrt{(1-\eta^2)N}\right] \exp\left[N g(\eta)\right], \tag{4.19}$$

where erf is the error function, $g(\eta) = \left[-\eta^2 + \Lambda\sqrt{\frac{1+\eta}{2}}\right]$. We here introduced the normalised inverse temperature $\Lambda = s\beta\Omega$, as the key parameter determining the energy landscape of the crossover. It linearly grows with the excitation density s, at a fixed temperature, or with the cooling of the system while the polaritons number is kept constant. For $\Lambda < \Lambda_C = 8$, $g(\eta)$ has an absolute maximum at $\eta_0 \in (0,1)$, with Λ_C corresponding to $\eta_0 = 1$, describing a fully stretched polymer. In Fig. 4.2 η_0 is plotted as a function of the normalised inverse temperature Λ. For $N \gg 1$ and $\Lambda < \Lambda_C$ we can thus analytically calculate the partition function using the Laplace method, leading to

$$Z \propto \sqrt{\frac{2\pi}{N g''(\eta_0)}} \quad \mathrm{erf}\left[\sqrt{(1-\eta_0^2)N}\right] \exp\left[N g(\eta_0)\right]. \tag{4.20}$$

The average energy of the lower polariton resonance can now be calculated dividing the expectation value of energy by the number of polaritons M

$$\langle \omega_- \rangle = \omega_x - \frac{\Omega}{N} \frac{d \ln Z}{d\Lambda}, \tag{4.21}$$

that from Eq. 4.20, in the thermodynamic limit $N \to \infty$ with Ω finite, takes the form

$$\langle \omega_- \rangle^{\mathrm{th}} = \omega_x - \Omega\sqrt{\frac{1+\eta_0}{2}}. \tag{4.22}$$

The average lower polariton energy thus interpolates between ω_-^{iso} and ω_-^{min} as the polymer passes from its bunched ($R \approx \sqrt{N}$, $\eta_0 \approx 0$) to its stretched ($R \approx N$, $\eta_0 \approx 1$) phase.

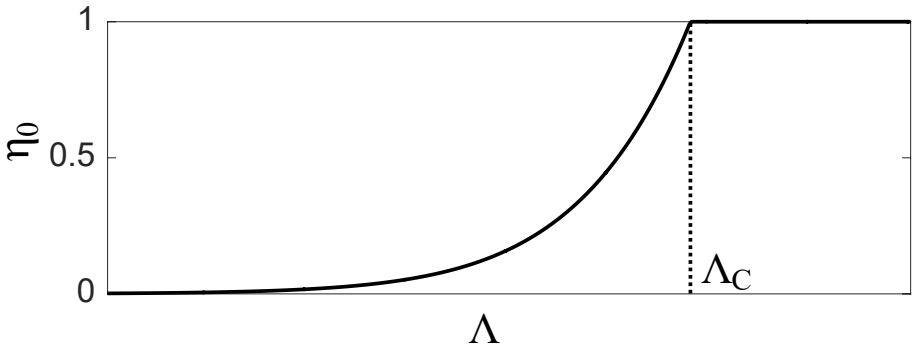

Figure 4.2: Top panel: η_0, as a function of the normalised inverse temperature Λ.

4.3 Results and discussion

In Fig. 4.2 we plot the energy of the lower polariton resonance as a function of the normalised inverse temperature Λ, obtained through the Laplace method in Eq. 4.22 (black solid line), and numerically integrating Eq. 4.16 with the exact form of the endpoint distribution from Eq. 4.17 for $N = 10$ (red dashed line) and using the Gaussian from Eq. 4.18 for $N = 10$ (blue dash-dotted line) and 100 (green dotted line). We can see that the system undergoes an orientational phase transition at the critical normalised temperature $\Lambda_C = 8$, that is a critical temperature $k_B T_C = \frac{s\Omega}{8}$. Numerical and analytical results support our initial intuition. At high excitation density (low temperature, $\Lambda \geq 8$) the optomechanical cavity force is strong enough to overcome thermal fluctuations and align all the dipoles parallel to the electric field, thus increasing the coupling and leading the polariton energy to its minimal value $\omega_-^{\min}$ from Eq. 4.12. At low excitation density instead (high temperature, $\Lambda \ll 8$) the force exerted by the cavity field on each dipole is not enough to compete against thermal fluctuations and the dipoles end up in an isotropic configuration. When the dipoles are not aligned with the electric field their average coupling is smaller, and the polariton energy starts to increase, converging at the isotropic value ω_-^{iso} from Eq. 4.13 for $\Lambda \approx 0.1$. The phase transition would thus manifest itself as an intensity-dependent shift of the lower polariton resonance upon optical pumping. In such a process only polaritonic bright states can be generated and thus the transition can be observed while the excitation density s is kept constant through the interplay of pump and losses long enough for the system to thermalize, regardless of

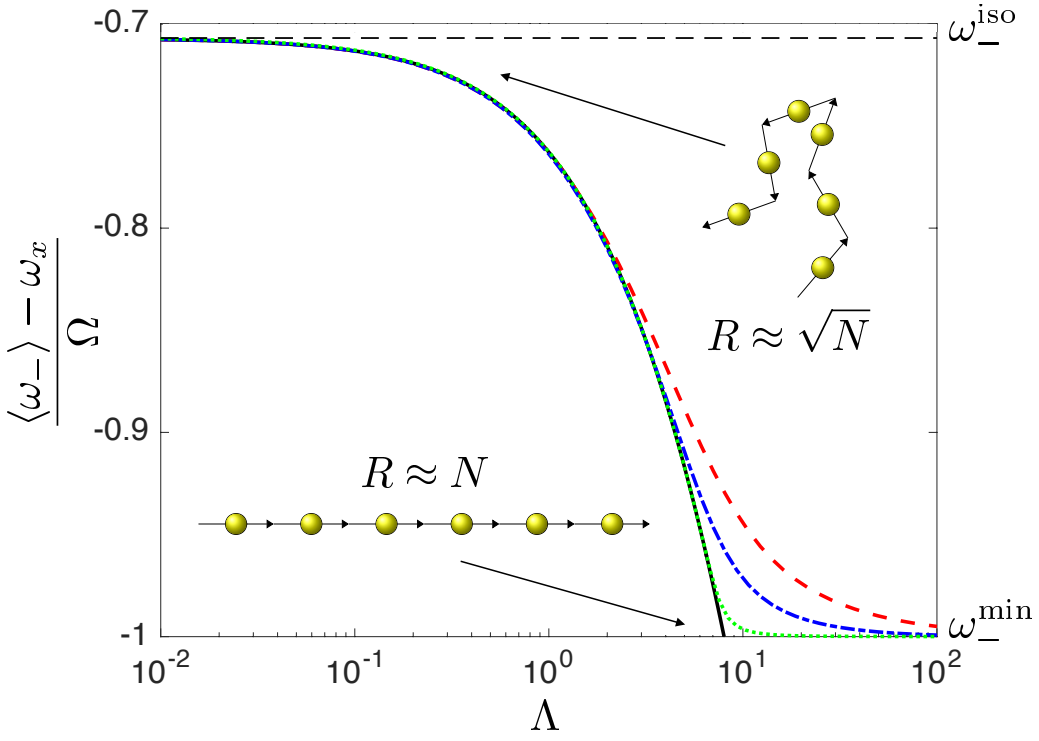

Figure 4.3: Energy of the lower polariton resonance as a function of Λ, obtained through the Laplace method in Eq. 4.22 (black solid line), and numerically integrating Eq. 4.16 either with the exact form of the endpoint distribution from Eq. 4.17 for $N = 10$ (red dashed line) and using the Gaussian form from Eq. 4.18 for $N = 10$ (blue dash-dotted line) and 100 (green dotted line).

the polariton lifetime.

4.3.1 Saturation effects

In writing Eq. 4.14 we made the assumption that the energy of the lowest lying state in the M excitations manifold can be written as M times the lower polariton energy ω_- from Eq. 4.11. While this is certainly true for a bosonic (harmonic) system, polaritons are strictly bosonic only in the dilute regime $s \ll 1$ and we thus need to assess for which value of s our theory remains accurate. To do so we numerically diagonalise the Hamiltonian in Eq. 3.21 in the M excitation manifold for the homogeneous case $\theta_n = 0 \ \forall n$. The lowest lying eigenvalue divided by M, that is the saturated lower polariton energy ω_-^{sat}, is plotted in Fig. 4.4 as a function of the excitation density s. The results are plotted for $N = 100$ (black solid line) and $N = 1000$ (red circles), showing that convergence has been achieved. The ω_-^{sat} shift with s highlights physics beyond the present bosonic treatment, including possibly an increased impact of the RWA. Still, comparing ω_-^{sat} with the value ω_-^{min} expected for a perfectly bosonic system, we can see that saturation leads to changes sizeably smaller than the effect we expect to observe, and it can thus be neglected for not too large values of s.

Organic microcavities are a promising system for an experimental implementation of our model. In those systems polariton condensates with filling fractions s of the order of 0.1 have been achieved , although we wish to stress that presence of coherence play no role in our theory. Note that the presence of a non-resonant pump used to create the condensate could also lead to spurious effects on the dipole orientation due to AC-Stark effect. Those nevertheless can be made negligibly small by increasing the detuning or completely removed using a non-polarised pump.

Record values of the light-matter coupling, up to $\Omega \approx 500$ meV, have been achieved in molecular crystals [78, 79, 80], that for an excitation density $s = 0.2$ corresponds to a critical temperature $k_B T_C = 150$ K, with the onset of the phase transition clearly visible well above room temperature. Strong coupling has also been obtained in floating molecules and molecular liquids [81], although using vibrational and not electronic transitions, leading to much smaller couplings. Strongly coupled electronic transitions in floating organic molecules seem thus a natural candidate to observe the phase transition, where the presence of a viscous solvent would easily allow to satisfy the classicality and adiabaticity conditions we imposed on our model. The

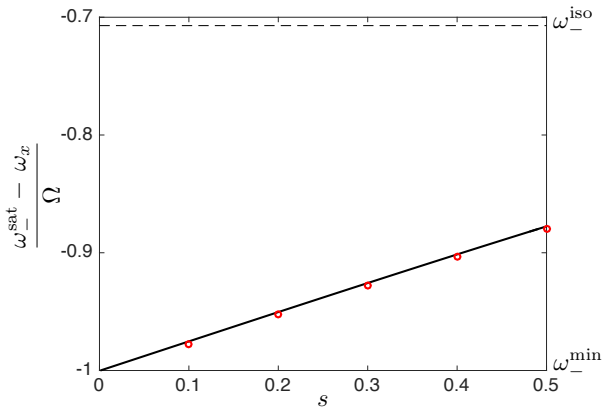

Figure 4.4: Plot as a function of the excitation density s of the saturated lower polariton energy $\omega_-^{\rm sat}$. The black solid line corresponds to $N = 100$ while the red dots to $N = 1000$. The black dashed line marks instead the isotropic value from the bosonic theory.

two-dimensional character of the dipoles could be implemented using phobic molecules floating on the surface of the solvent in an open cavity [82], or a similar three-dimensional case could be realised with molecules in suspension using a flow-cell cavity, conceptually similar to the one described in Ref. [83].

4.4 Conclusion

In conclusion we proved that, exploiting highly excited states, collective interactions of dipoles with a photonic cavity can generate optomechanical effects allowing to manipulate the microscopic degrees of freedom associated with the individual dipoles. As a first example we studied the case of rotating, strongly coupled two-dimensional dipoles, proving that the system undergoes a crossover from an isotropic to an aligned phase. We also demonstrated that, in a highly excited system, SC effects upon orientational degrees of freedom are governed by the collective light-matter coupling, and as such they can be possibly experimentally visible and not washed out by thermal energy. However, at the time in which this dissertation is written, recent advances in plasmonics have allowed to achieve SC even for a single molecule [37].

This implies that the energy landscape of cavity-induced phenomena could scale as the single-molecule coupling and be observable at standard temperatures. This important milestone will open the door to a wide number of new fundamental perspectives and applications.

Shortly after the publication of our results, further interest has been shown about cavity-induced control of orientational degrees of freedom in molecular systems. J. Keeling and co workers at University of St. Andrews published the work [84], in which they consider exactly our system, with the scope of improving the accuracy of our results. They manage to highlight two very important points. First of all, they point out that a Gaussian approximation for the calculation of the end-to-end probability distribution is inaccurate to reproduce correct results in the limit of high excitation density. This because such approximation is valid for typical values of the endpoint length $\mathbf{R}$, which means values of the order of $\sqrt{N}$, while, in the limit of large s, the light-matter coupling leads the system towards atypical configurations, where $\mathbf{R}$ is of the order of N. Such values are not counted by the Gaussian distribution. The authors also demonstrates that the evolution of the orientational order with temperature and excitation density can be achieved using different approaches, such as mean field theory for the calculation of the partition function, and large deviations formulation of the endpoint probability distribution.

Chapter 5

Tuning the electronic properties of a doped semiconductor heterostructure

5.1 Introduction

In the previous chapters, we studied how the saturation effects due to an intrinsic dipole-dipole interaction can affect the effective light-matter coupling strength, and how the light-matter coupling can modify properties of the underlying matter degrees of freedom.

SC regime investigation usually involves the interaction of a discrete photon mode with electronic transitions occurring between two or more energy bound states (bound-to-bound), in which the electrons are localised. In this case, the electron can reversibly jump from one state to another discrete state by exchanging photons with the cavity with an exchange frequency higher than any relaxation processes. This results in the formation of light-matter hybrid states, named polaritons, which conserve both photons and matter properties.

Many works have investigated light-matter hybridization as a tool to strongly alter not only the spectrum, but also the electric response of organic [85, 86] and inorganic [87] semiconductor materials, motivated by the fact that tuning their electronic and optical properties beyond those allowed by their original chemical structure would open the way to a wide number of technological applications. On another side, recent improvements in res-

onator design and fabrication have allowed to reach the Very Strong Coupling (VSC) regime, with light-matter couplings large enough to couple multiple electronic states, characterised by different spatial wavefunctions, to the same photonic mode. This leads to polariton modes whose electronic part is a linear superposition of the uncoupled states with features a priori different from the initial ones. This regime has recently been experimentally demonstrated in inorganic microcavities, where a change of the exciton radius occurs as consequence of the multi-mode hybridization [52].

Aware of the recent advances, we wondered whether such a phenomenon could be pushed forward to non-perturbatively modify the electronic excitation wavefunctions and create bound states from the continuum of delocalised ones. Aiming to answer this question, our idea was thus to exploit the hybridization occurring when we strongly couple transitions between a bound electronic state to a continuum of delocalised states (*bound to continuum* transitions), also known as ionizing transitions. SC for bound-to-continuum transitions is apparently counter-intuitive because of the intrinsic irreversible nature of any ionization process, as an electron acquiring enough energy to overcome the ionising threshold escapes into one of the continuum unbound states. Nevertheless, we show that SC for bound-to-continuum transitions is not only in principle possible but also experimentally observable.

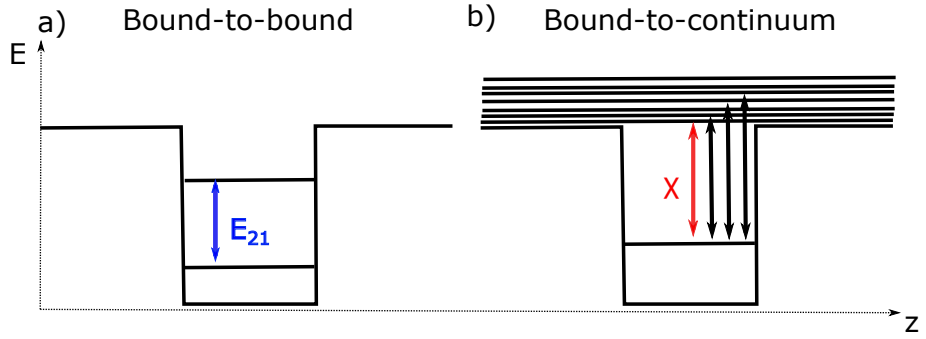

Figure 5.1: Bound-to-bound (panel (a)) and bound-to-continuum (panel(b)) transitions in a doped quantum well. E_{21} is the energy difference of the bound states in (a). χ is the first ionization energies (bound-to-continuum), also referred to as *ionization threshold* or continuum edge

In our study, we consider the case of microcavity-embedded doped quantum wells, which is a particularly suitable system for the achievement of

non-perturbative regimes. The first experimental observation of the USC regime has been achieved on this kind of platform in 2009 [9]. This system resulted to be a good candidate not only because changing the doping level in the quantum wells can easily tune the light-matter coupling strength, but also because its quasi-two-dimensional geometry allows us a simple numerical evaluation of its one-particle electronic states, both bound and unbound states. Moreover, it is possible to opportunely design the structure in order to host a single bound electronic state and a continuum of ionised states, with electrons undergoing only bound-to-continuum transitions, whose transition energies form a continuum (or a quasi-continuum) starting from a minimum ionization energy. A sketch highlighting the difference between bound-to-bound and bound-to-continuum can be found in Fig. 5.1.

We first theoretically and later experimentally showed the appearance of an optical discrete resonance below the continuum ionization threshold for large enough values of the light-matter coupling strengths. Such a resonance describes a transition of the electrons to a novel cavity-induced electronic state lying below the continuum edge, due to the collective coupling of the electron gas with the the photonic resonator field. As the lower edge of the continuum corresponds to a case of free electrons with zero kinetic energy, the novel discrete electronic state can only be bound, as the electrons in this state would not have enough energy to escape into the continuum. It is worthwhile to say that a physics similar to the one we consider here has also been theoretically described in terms of a Feshbach resonance without bound states in the uncoupled channels [88]. In our case, the two uncoupled channels are represented by the unbound electronic states with zero and one photon, which are coupled by the light-matter inter-channel coupling creating a bound state.

This result can be understood more deeply if one aims to investigate the nature of the novel electronic state. The physics of QWs tells us that the optical response of an undoped QW is dominated by the presence of a bound exciton resonance, representing a physical state in which an electron in the conduction band and a hole in the valence are bound together by Coulomb interaction [90]. Nevertheless, it also says that the doped QW counterpart does not manifests the same feature. The origin of this difference is sketched in Fig 5.2 and can be explained by recalling the electron-hole remapping approach used to show the formation of bound excitons in solid-state semiconductors.

The intrinsic difference between the two cases is due to the different sign

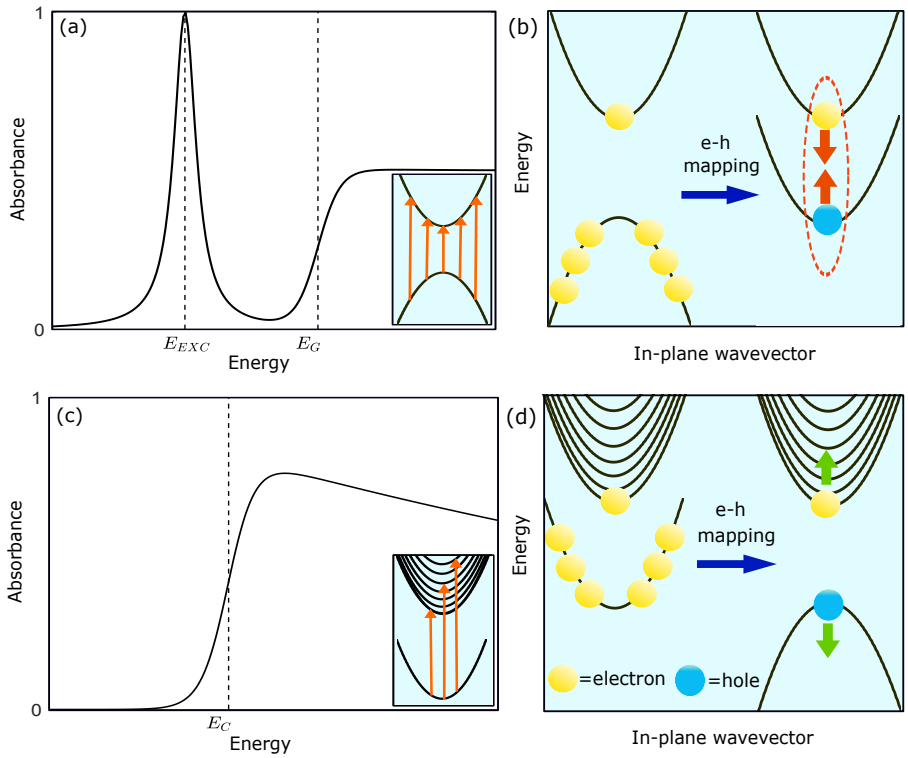

Figure 5.2: **Coulomb effect in doped and undoped quantum wells.** In panel (a) we sketch the interband absorbance of an undoped semiconductor QW, dominated by an excitonic peak below the bandgap and a continuum absorption above it. In the inset we schematically illustrate the origin of the continuum part of the spectrum, understandable in a single-electron picture as interband transitions of electrons with different in-plane wavevectors. In panel (b) we illustrate the standard electron-hole mapping, allowing us to describe a single electron vacancy in the valence band as a hole with positive charge and mass. We can thus understand the excitonic peak as an hydrogenoid bound state of an electron and a positively charged hole. In panel (c) we sketch instead the intersubband absorbance of a doped QW containing only one localized state, and a *continuum* of states above the barrier. Only the asymmetric, large bound-to-continuum absorbance is present, and no excitonic peak is visible [89]. As shown in the inset the continuum is, in this case, due to each electron having multiple possible delocalised final states. The reason for the lack of an excitonic resonance is illustrated in panel d). As the initially filled electron subband has in this case a positive effective mass, the electron-hole mapping leads to a positively charged hole with negative effective mass, unable to form a bound state with the electron.

of the effective mass of the electron in the initial band, which is negative for the fully filled valence band in the undoped QW, and positive for the partially filled conduction subband in the doped QW case. By the remapping, it is easy to see that this sign difference is indeed transferred to a sign difference of the final hole charge: while in the undoped case electron and hole are oppositely charged and as such exhibit Coulomb attraction, in the doped case the hole has negative charge and its interaction with the electron is repulsive [91]. Therefore, in the doped QW, no Coulomb-mediated bound exciton is formed.

The appearance of a novel cavity-induced bound electron state in a doped QW system demonstrates that a bound exciton can actually be induced by the exchange of photons with a cavity field and not by Coulomb interaction. This conclusion completely overturns the concept of exciton its self strictly related to the Coulomb interaction, as it has always been presented so far in the bibliography.

5.2 Quantum system

Before presenting in the details the most relevant results we have obtained, in the following paragraph I will be giving some key notions about the physics of doped quantum well heterostructure, in order to not be repetitive and ensure a full understanding of the reader.

5.2.1 Doped Quantum Well

A quantum well is a quantum heterostructure where a thin layer of a certain semiconductor material, for instance Gallium Arsenide (GaAs), is sandwiched between two layers of an other semiconductor with a wider bandgap, for instance Alluminium Gallium Arsenide (AlGaAs), such that the discontinuity of both conduction and valence bands leads to discrete energy levels in each band, called subbands. This structure has a quasi-two-dimensional geometry, thus characterized by a strong confinement of the electrons along the growth axis into the almost planar region of smaller bandgap, where they are forced to behave as a two-dimensional electron gas (2DEG) and to occupy the discrete subbands. The electrons can only have discrete wavevector components along the growth axis, conventionally the z-axis, while they are free to move on the normal plane with a different effective mass, depending on the

subband dispersion $\hbar\omega_{b,\mu}(k)$, with $b \in [v, c]$ standing for valence or conduction band, μ indicating the subband and k the in-plane wavevector. Electronic transitions from a subband to another are called *intersubband transitions*. The Fermi energy for an undoped quantum well lies between valence and the conduction bands, and, in this case, an electron-hole pair binds via Coulomb interaction. Exciton states have been deeply studied both theoretically and experimentally via magneto-optics spectroscopy [92, 93, 94].

When carriers are injected in the system, that means when the quantum well is doped, the Fermi level can be raised between two subbands in the conduction band, selecting which intersubband transitions are optically active. In Fig. 5.2.1 a sketch of a typical single doped quantum well structure is shown.

Intersubband transitions (ISBTs) in doped quantum well coupled to a cavity field have been object of lot of interest due to the fact that the almost parallelness of the subband dispersions allows to consider the 2DEG as an ensamble of 2-level systems with the same transition frequency. This happens because the wavevector of the photon interacting with the system is in general very small compared to the in-plane wavevector of the subband dispersion, and then the transitions from a subband to another can be considered vertical, with no exchange of in-plane momentum. ISBTs are then suitable to observe SC of collective excitations, well described by the Dicke model. As described in 2.3.2, this model predicts that, for an ensamble of N 2-level system with the same transition frequency, only one linear superposition of single electronic excitation, called bright intersubband excitation, couples to the cavity mode with a dipole $\sqrt{N}$ bigger than the one of a single excitation. This gives arise to half-light half-matter quasi-particle, known as *intersubband polaritons*. The enhanced dipole of the intersubband system is oriented along the growth axis leading to a polarization selection rule for the cavity field modes: only the Transverse magnetic (TM) field mode can couple to the intersubband dipole, having a non-zero component of the electric field along the same growth axis. The first experimental observation of intersubband polaritons dispersions has been reported in [95], where the reflectance resonance peaks of a microcavity-embedded-doped-QWs structure clearly show an anti-crossing due to the formation of hybrid polariton states (Fig. 5.2.1). It is thus sufficient to change the electron density in the quantum well to increase the light-matter coupling strength, even beyond the USC regime threshold. We remind that the first observation of USC in 2009 was on an intersubband polaritons platform with a normalised coupling

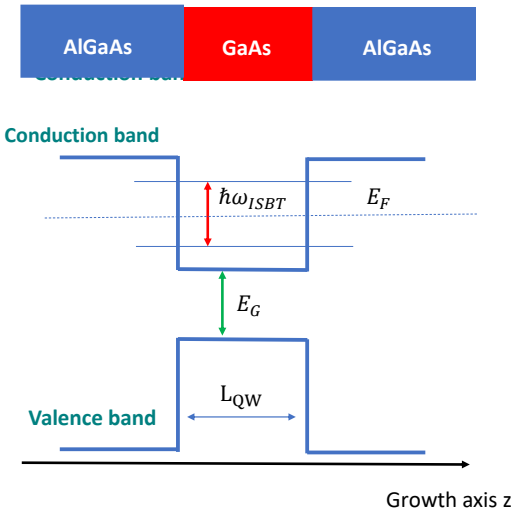

Figure 5.3: **Sketch of a typical doped quantum well structure.** Top: material composition of a single quantum well, in which a single layer of narrow-band-gap material (e.g. GaAs) is sandwiched between two barriers of a larger-bandgap material (e.g. AlGaAs). Bottom: Sketch of a typical band structure for a single well. E_F is the Fermi energy, which the doping sets within the conduction band. E_G is the energy gap between the bottom of the conduction band and the the top of the valence band. ω_{ISBT} is intersubband transition frequency.

of 0.11 [9], while now the record value for intersubband systems is 0.45 [96].

In our study we considered a GaAs/AlGaAs quantum heterostructure composed of N_{QW} quantum wells embedded in microcavity resonator. Details about the latter will be presented in the next paragraph. The thickness of the single well is taken enough small ($L_{\mathrm{QW}} = 4nm$) to manifest only one single electronic bound state below the continuum edge, in order to exclude the appearance of intersubband polaritons, generated by bound-to-bound intersubband transitions (Fig. 5.2.1).

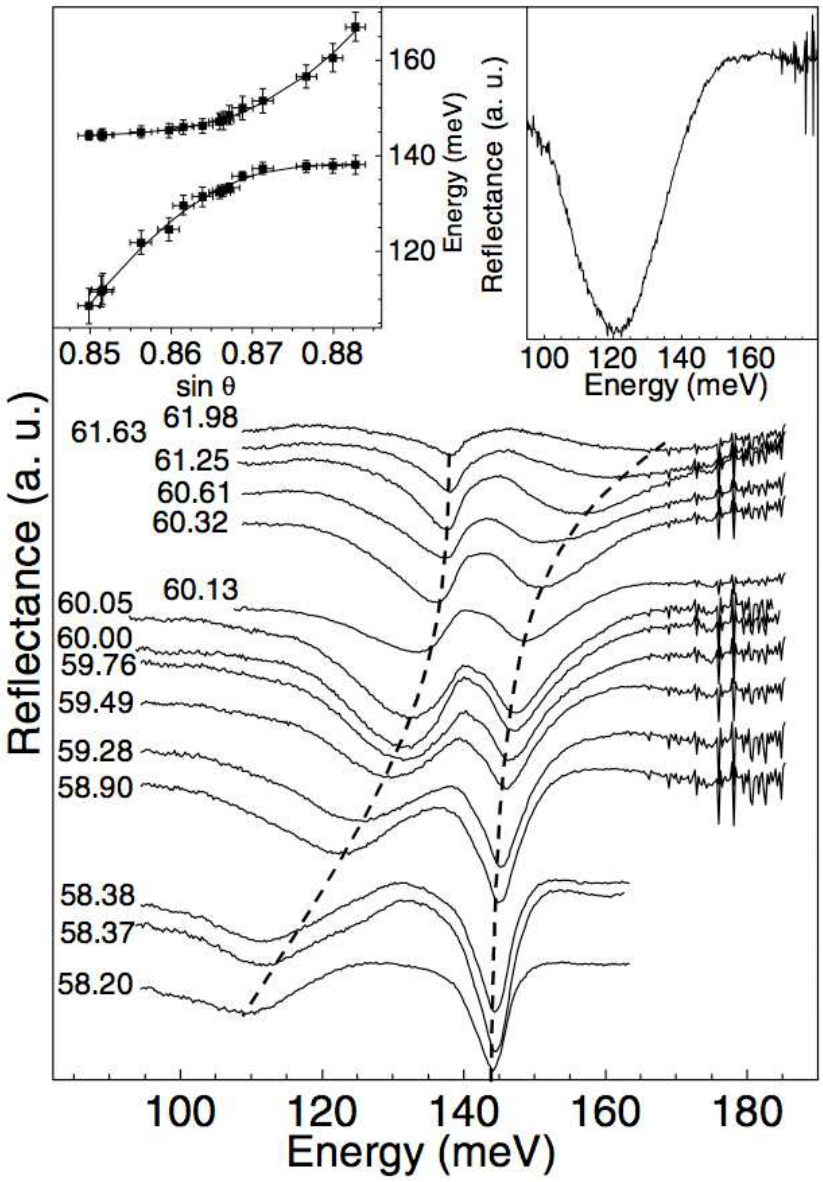

Figure 5.4: Experimental reflectance data from [95] for various angles show clearly a polaritonic anticrossing. This is the first experimental observation of intersubband polaritons

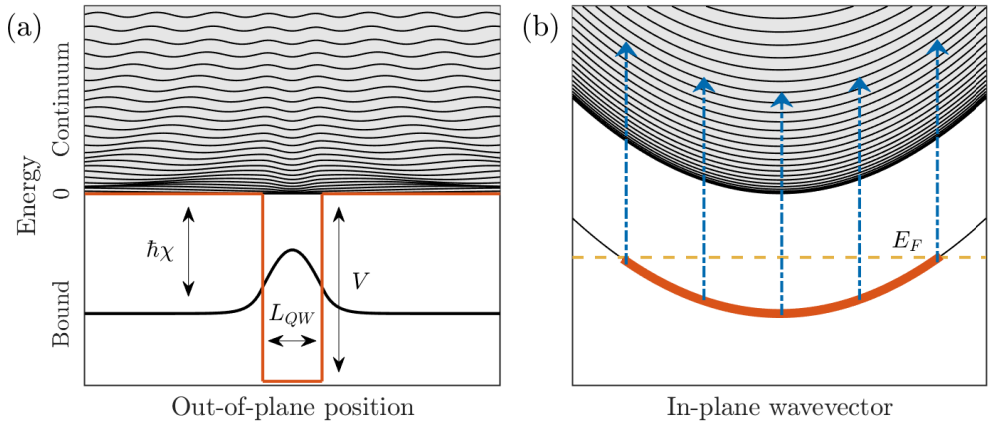

Figure 5.5: Schematic representation of the electronic structure of a quantum well of width L_{QW}, with a single bound state below the continuum (shaded in gray). (a) Electronic density envelope functions of the different single-particle eigenmodes, shifted by their energy. The potential profile is plotted in red, with the first ionisation energy $\hbar\chi$ and the conduction band discontinuity V explicitly marked. The figure has been obtained using the parameters of the structure described in Sec. 5.4.1. For sake of clarity only one continuum mode every ten is shown, with its probability density multiplied by ten. (b) In-plane dispersion of the different subbands in momentum space. The single bound state is filled with electrons (in red), up to the Fermi energy E_F (dashed yellow line). The dash-dotted blue arrows represent a collective bound-to-continuum transition.

5.2.2 Microcavity resonator

One of the most commonly employed microcavity resonator for quantum well systems is characterised by a planar geometry in order to be embedded in the semiconductor heterostructure. It can be made of Bragg-type or metallic mirrors, according to the physics we need to explore. In a planar cavity the photon wavevector along the growth axis is quantized, such that the photon energy dispersion can be expressed as

$$\hbar\omega_{cav,\nu} = \hbar\frac{c}{\sqrt{\epsilon_r}}\sqrt{q^2 + q_{z,\nu}^2}, \tag{5.1}$$

where ϵ_r is the relative dielectric constant of the cavity medium, q and $q_{z,\nu}$ are respectively the in-plane component and the quantized normal component of the photon wavevector, with quantum number $\nu = 0, 1, 2, ..$, for TM polarized light. For sake of simplicity and due to the relatively small overall size of the cavity-quantum well structure, in our study we couple the system to the $\nu = 0$ TM polarized photon mode, for which the dispersion is perfectly linear with the in-plane wavevector.

In the experimental implementation, in order to opportunely tune the cavity energy according to the bound-to-continuum transitions frequency range, highly-confining, grating-shaped gold microcavity resonators have been used. These are metal-semiconductor-metal grating resonators with period D and width of the metallic finger p, following a procedure similar to the one in Ref.[98]. The extreme thinness of the active region forbids operation in the photonic-crystal regime [99], as each module made of metallic finger, semiconductor substrate, and gold bottom mirror behaves as an independent resonator. A sketch of the resonator system and the mode dispersion can be found in Fig. 5.2.2(a)-(b). The resonance frequency $\omega_{0,m}$ is set by p, and not by the period D, according to the formula

$$\omega_{0,m} = \frac{2\pi c}{n_{eff}}\frac{m}{p} \tag{5.2}$$

with n_{eff} effective refractive index of the resonator considering the reflectivity phase at the metallic boundaries, and m integer number representing the quantization of the in-plane wavevector along the grating direction. As stated above, the index 0 indicates that we are referring to a TM0 mode along the z-axis.

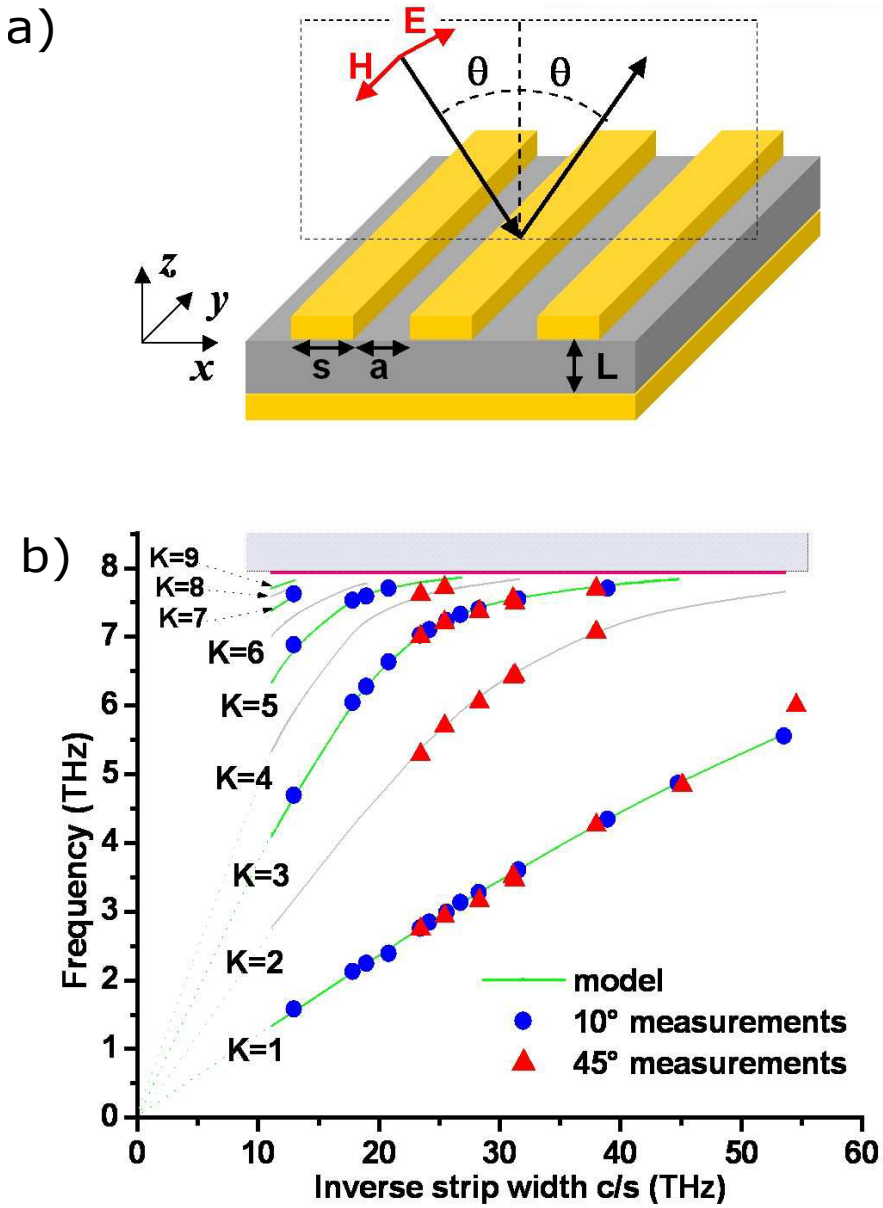

Figure 5.6: Sketch of the metal-dielectric-metal resonator structure (a) and modes energy dispersion as a function of the inverse metal finger width c/s (b), taken from Ref. [97]. In our dissertation, we name the metal finger width as p and the integer number denoting each mode as m

5.3 Theory

The problem of coupling a discrete resonance to a continuum has been initially addressed by Fano in his landmark paper [100]. In that work, Fano studies the interference of a discrete electronic state with a continuum of ionized states, assuming though the coupled eigenergies lying within the uncoupled continuum. This leads to the to the characteristic asymmetrical absorbance lineshape. In our work we consider instead a semi-infinite continuum of ionised unbound states and that one of the coupled eigenenergies falls below the ionisation threshold, either because the uncoupled discrete resonance is already below the continuum or because the coupling strength is large enough to push the coupled mode downwards.

In this section we present the theory used for bound-to-continuum strong coupling and the calculation of the resonator-induced bound exciton states. We applied for the bound-to-continuum case the same theory described in [101] for multiple-intersubband transitions in the electric dipole gauge. In multiple-quantum well semiconductor heterostructures, the single electron wavefunctions can be indexed by the in-plane wavevector $\mathbf{k}$, and by the quantum number n indicating the energy level, both bound and continuum states. The field operator for the electron can be written as

$$\mathbf{\Psi_k(z)} = \sum_{\mathbf{n}} \phi_{\mathbf{n}}(\mathbf{z}) \mathbf{c_{n,k}}, \tag{5.3}$$

where $c_{n,\mathbf{k}}$ is the annihilation operator for the electron in the n-th subband with energy $\hbar\omega_{n,bfk}$ and in-plane momentum $\mathbf{k}$, and $\phi_n(z)$ is the envelope wavefunction. The single-particle spectrum is thus formed by negative energies ($\hbar\omega_{n,\mathbf{k}} < 0$), which correspond to bound electronic states, and positive energies ($\hbar\omega_{n,\mathbf{k}} > 0$) corresponding to unbound states delocalised across the bulk. We refer to these last states as continuum states even though they arrange themself either as a real continuum or as a set of broadened minibands, due to the finite size of the semiconductor bulk.

To describe the system we use the Power-Zienau-Wooley (PZW) Hamiltonian, initially introduced to describe multisubbands polariton in Ref. [101, 102]. Introducing $a_{c,\mathbf{q}}$, the bosonic operator for a cavity photon with in-plane wavevector $\mathbf{q}$ and frequency $\omega^c_{\mathbf{q}}$, it is possible to write the Hamiltonian

in terms of the electronic operators $c_{n,\mathbf{k}}$ as

$$\begin{aligned} H &= \sum_{\mathbf{q}} \Bigg[\hbar\omega_q^a a_{\mathbf{q}}^\dagger a_{\mathbf{q}} + \sum_{\mathbf{k}} \omega_{n,\mathbf{k}} c_{n,\mathbf{k}}^\dagger c_{n,\mathbf{k}} \\ &+ \sum_{m>n,\mathbf{k}} \sqrt{\frac{\hbar\omega_q^a}{2\epsilon_0\epsilon S L_c}} \frac{\hbar e d_{nm}}{2m^*\omega_{n,m}} (a_{-\mathbf{q}}^\dagger + a_{\mathbf{q}}) \left(c_{n,\mathbf{k}+\mathbf{q}}^\dagger c_{m,\mathbf{k}} + c_{m,\mathbf{k}}^\dagger c_{n,\mathbf{k}-\mathbf{q}} \right) \\ &+ \frac{e^2\hbar^2}{8\epsilon_0\epsilon S m^*} \sum_{m>n} \sum_{m'>n',\mathbf{k}} \left(c_{n,\mathbf{k}+\mathbf{q}}^\dagger c_{m,\mathbf{k}} + c_{m,\mathbf{k}}^\dagger c_{n,\mathbf{k}-\mathbf{q}} \right) \\ &\times \left(c_{n',\mathbf{k}-\mathbf{q}}^\dagger c_{m',\mathbf{k}} + c_{m',\mathbf{k}}^\dagger c_{n',\mathbf{k}+\mathbf{q}} \right) \Bigg] \end{aligned} \tag{5.4}$$

.

In Eq.(5.4), the transition frequency between subbands n and m, ω_{nm} is considered dispersionless. This is due to the to the quasi-parabolic subbands dispersion and the smallness of the photonic momentum [14], such that

$$\omega_{n|\mathbf{k}+\mathbf{q}|}^c - \omega_{mk}^c \simeq \omega_{n0}^c - \omega_{m0}^c, \tag{5.5}$$

leading to transition frequency

$$\omega_{(nm)}^b = \omega_{n0}^c - \omega_{m0}^c. \tag{5.6}$$

The first two terms of Eq. 5.4 describe the free photonic and excitonic fields, the third the dipolar interaction between light and matter, the fourth the dipole-dipole interaction term, often named P^2 in a parallel with the A^2 term present in the Coulomb gauge. The remaining parameters of the Hamiltonian are L_c, the effective length of the photonic cavity, S the in-plane surface of the QWs heterostructure, and $d_{n,m}$, the dipole moment

$$d_{(nm)} = \int \left[\bar{\phi}_n(z)\partial_z\phi_m(z) - \phi_m(z)\partial_z\bar{\phi}_n(z) \right] dz. \tag{5.7}$$

. We now specialise the system to the case in which there is a single bound state per quantum well, the quantum wells are identical, and their respective bound levels can be considered quasi-degenerate. In this case each *bare* electronic bound state m has the same population density N_{2DEG}, we can then neglect intersubband bound-to-bound transitions and consider dielectric parameters inside the quantum well. In order to study the interaction between

the cavity photons and the subbands, we transform the fermionic Hamiltonian in Eq.5.4 to an effective bosonic Hamiltonian. In this way, we obtain a fully diagonalizable Hopfield-type model, as the one presented in 2.3.2. We thus need to replace the fermion operators $c_{n,\mathbf{k}}$ by collective operators $b_{\alpha,\mathbf{q}}$, which describes collective electronic transitions

$$b_{\alpha,\mathbf{q}} = \frac{1}{\sqrt{N}} \sum_{\mathbf{k}} c^{\dagger}_{n,\mathbf{k}+\mathbf{q}} c_{m,\mathbf{k}}, \tag{5.8}$$

where q is the excitation exchange wavevector, the index $\alpha = (m, n)$ identifies a specific transition from a subband n to a subband m. Unlike the photon operators, the collective electronic operators $b_{\alpha,\mathbf{q}}$ are not elementary bosonic, but, if we compute their commutator as in Ref.[103, 101], we obtain

$$\left[b_{\alpha,\mathbf{q}}, b^{\dagger}_{\alpha,\mathbf{q}}\right] = \frac{1}{N} \sum_{\mathbf{k}} \left(c^{\dagger}_{m,\mathbf{k}} c_{m,\mathbf{k}} - c^{\dagger}_{n,\mathbf{k}+\mathbf{q}} c_{n,\mathbf{k}+\mathbf{q}} \right), \tag{5.9}$$

that we can recognize as the difference of the number operators for the two subbands. If we consider a weakly excited system, where the number of excitations we wish to treat is much smaller than the number of electrons N, the operator 5.8 can be assumed bosonic, obeying the commutation rule

$$[b_{\alpha,\mathbf{q}}, b_{\beta,\mathbf{q}'}] = \delta_{\alpha,\beta}\delta(\mathbf{q} - \mathbf{q}'). \tag{5.10}$$

The Power-Zienau-Wooley Hamiltonian thus reads

$$\begin{aligned} H \;=\; & \sum_{\mathbf{q}} \Bigg[\hbar\omega^{a}_{q} a^{\dagger}_{\mathbf{q}} a_{\mathbf{q}} + \sum_{\alpha} \omega^{b}_{\alpha} b^{\dagger}_{\alpha\mathbf{q}} b_{\alpha\mathbf{q}} \\ & + \sum_{\alpha} \frac{\hbar\omega_{P\alpha} d_{\alpha}}{2} \sqrt{\frac{\omega^{a}_{q}}{L_c I_{\alpha\alpha} \omega^{b}_{\alpha}}} (a^{\dagger}_{-\mathbf{q}} + a_{\mathbf{q}})(b^{\dagger}_{\alpha\mathbf{q}} + b_{\alpha-\mathbf{q}}) \\ & + \sum_{\alpha,\beta} \frac{I_{\alpha\beta}}{\sqrt{I_{\alpha\alpha} I_{\beta\beta}}} \frac{\hbar\omega_{P\alpha}\omega_{P\beta}}{4\sqrt{\omega^{b}_{\alpha}\omega^{b}_{\beta}}} (b^{\dagger}_{\alpha\mathbf{q}} + b_{\alpha-\mathbf{q}})(b^{\dagger}_{\beta-\mathbf{q}} + b_{\beta\mathbf{q}}) \Bigg], \end{aligned} \tag{5.11}$$

where we introduced the plasma frequency $\omega_{P\alpha}$, as

$$\omega^{2}_{P\alpha} \;=\; \frac{I_{\alpha\alpha}\hbar e^{2} N_{2DEG}}{2 m^{*2}_{W} \epsilon_0 \epsilon_r \omega^{b}_{\alpha}}. \tag{5.12}$$

In Eq.5.12 the term $I_{\alpha\beta}$ is an overlap integral between the currents generated by different transitions $\alpha = (n, m)$ and $\beta = (n', m')$

$$\begin{aligned} I_{\alpha\beta} &= \int \left(\bar{\phi}_n(z)\partial_z\phi_m(z) - \phi_m(z)\partial_z\bar{\phi}_n(z)\right) \times \\ &\quad \left(\bar{\phi}_{n'}(z)\partial_z\phi_{m'}(z) - \phi_{m'}(z)\partial_z\bar{\phi}_{n'}(z)\right) dz. \end{aligned} \tag{5.13}$$

Assuming a factorised form for the overlap integral,

$$I_{\alpha\beta} = \sqrt{I_{\alpha\alpha}I_{\beta\beta}}, \tag{5.14}$$

corresponds to applying an effective medium approximation, as in Ref. [104]. This means assuming no correlations between currents of different transitions allowing to treat the QWs heterostructure as a whole medium with an effective dielectric function.

We now introduce the concept of effective length L^{α}_{eff}, initially presented in Ref.[105], describing the spatial extension of the current density of a specific transition

$$L^{\alpha}_{eff} = \frac{2m^*\omega^b_\alpha}{\hbar I_{\alpha\alpha}}. \tag{5.15}$$

Expressing the light-matter coupling parameter in terms of the transition harmonic oscillator $f^o_\alpha = \frac{\hbar d^2_\alpha}{2m^*\omega^b_\alpha}$, we can rewrite the light-matter interaction term of the Hamiltonian in Eq. 5.11 as

$$H_{L-M} = \sum_{\mathbf{q}}\sum_{\alpha} \frac{\hbar\omega_{P\alpha}}{2}\sqrt{\frac{\omega^a_q}{\omega^b_\alpha} f^o_\alpha f_\alpha}(a^\dagger_{-\mathbf{q}} + a_{\mathbf{q}})(b^\dagger_{\alpha\mathbf{q}} + b_{\alpha-\mathbf{q}}). \tag{5.16}$$

In Eq. 5.16 we introduced the parameter $f_\alpha = \frac{L^{\alpha}_{eff}}{L_c}$ [101], which quantifies how much of the total cavity length is occupied by the electronic current of each transition. It is thus reasonable to expect this factor to have a weight in the light-matter coupling.

At high electron density regimes, plasmonic effects due to the Coulomb interaction of electrons involved in different transitions have to be considered. We start considering at first the matter part of the Hamiltonian

$$H_M = \sum_{\mathbf{q}}\left[\sum_{\alpha}\omega^b_\alpha b^\dagger_{\alpha\mathbf{q}}b_{\alpha\mathbf{q}} + \sum_{\alpha,\beta}\frac{I_{\alpha\beta}}{\sqrt{I_{\alpha\alpha}I_{\beta\beta}}}\frac{\hbar\omega_{P\alpha}\omega_{P\beta}}{4\sqrt{\omega^b_\alpha\omega^b_\beta}}(b^\dagger_{\alpha\mathbf{q}} + b_{\alpha-\mathbf{q}})(b^\dagger_{\beta-\mathbf{q}} + b_{\beta\mathbf{q}})\right], \tag{5.17}$$

which can be diagonalised in terms of multisubband plasmon operators as

$$H_M = \sum_{\alpha\mathbf{q}} \hbar\omega^p_\alpha p^\dagger_{\alpha\mathbf{q}} p_{\alpha\mathbf{q}}, \tag{5.18}$$

where the collective transition operators between single-particle states can be expressed as linear superpositions of multisubband plasmons

$$(b^\dagger_{\alpha\mathbf{q}} + b_{\alpha-\mathbf{q}}) = \sum_\beta h_{\alpha\beta}(p^\dagger_{\beta\mathbf{q}} + p_{\beta-\mathbf{q}}). \tag{5.19}$$

Introducing the renormalised coupling coefficient

$$\Xi_{\alpha q} = \sqrt{\frac{\omega^a_q}{L_c}} \left[\sum_\beta h_{\beta\alpha} \frac{\omega_{P\beta} d_\beta}{\sqrt{I_{\beta\beta}\omega^b_\beta}} \right], \tag{5.20}$$

it is possible to rewrite the light-matter Hamiltonian

$$H = \sum_{\mathbf{q}} \left[\hbar\omega^c_{\mathbf{q}} a^\dagger_{\mathbf{q}} a_{\mathbf{q}} + \sum_\alpha \hbar\omega^P_\alpha p^\dagger_{\alpha,\mathbf{q}} p^\dagger_{\alpha,\mathbf{q}} + \sum_\alpha \frac{\hbar\Xi_{\alpha q}}{2} \left(a_{\mathbf{q}} + a^\dagger_{\mathbf{q}}\right) \left(p_{\alpha,\mathbf{q}} + p^\dagger_{\alpha,-\mathbf{q}}\right) \right], \tag{5.21}$$

where $\omega^P_\alpha = \sqrt{\omega^{b2}_\alpha + \omega^{P2}_\alpha}$ is the electronic transition frequency dressed by the plasmonic effects.

We can diagonalise this Hamiltonian by Hopfield-Bogoliubov transformations, which express the plasmon and photon operators in terms of the polariton operators $d_{\alpha,\mathbf{q}}$

$$d_{s,\mathbf{q}} = x_{sq} a_{\mathbf{q}} + z_{sq} a^\dagger_{-\mathbf{q}} + \sum_\alpha \left[y_{s\alpha q} p_{\alpha,\mathbf{q}} + w_{s\alpha q} p^\dagger_{\alpha,-\mathbf{q}} \right]. \tag{5.22}$$

In the case considered by Fano, the index s runs over the continuum coupled states, whilst in our case one of the coupled modes has frequency $\omega^d_{s,\mathbf{q}} < \chi$, where we define the first ionization threshold χ as the lowest ω^P_α belonging

to the continuum. Starting from the Heisenberg equations for our system,

$$x_{s,q}\left(\omega^d_{s\mathbf{q}}-\omega^c_{\mathbf{q}}\right) = \frac{1}{2}\sum_\alpha\left(\Xi_\alpha y_{s\alpha q}-\Xi^*_\alpha w_{s\alpha q}\right), \tag{5.23}$$

$$z_{s,q}\left(\omega^d_{s\mathbf{q}}+\omega^c_{\mathbf{q}}\right) = \frac{1}{2}\sum_\alpha\left(\Xi_\alpha y_{s\alpha q}-\Xi^*_\alpha w_{s\alpha q}\right), \tag{5.24}$$

$$y_{\alpha,q}\left(\omega^d_{s\mathbf{q}}-\omega^P_\alpha\right) = \frac{1}{2}\Xi^*_\alpha\left(x_{sq}-z_{sq}\right), \tag{5.25}$$

$$w_{\alpha,q}\left(\omega^d_{s\mathbf{q}}+\omega^P_\alpha\right) = \frac{1}{2}\Xi_\alpha\left(x_{sq}-z_{sq}\right), \tag{5.26}$$

we find that the frequency $\omega^d_{s,\mathbf{q}}$ obeys the equation

$$\frac{\omega^c_{\mathbf{q}}}{\omega^{d2}_{s,\mathbf{q}}-\omega^{c2}_{\mathbf{q}}}\sum_\alpha|\Xi_\alpha|^2\frac{\omega^P_\alpha}{\omega^{d2}_{s,\mathbf{q}}-\omega^{P2}_\alpha}=1. \tag{5.27}$$

By manipulating the equation above and dividing by χ^2, we arrive to the condition for having a discrete solution

$$\sum_\alpha|\Xi_\alpha|^2\frac{\omega^c_{\mathbf{q}}}{\chi}\frac{1}{\omega^{d2}_{s,\mathbf{q}}-\omega^{P2}_\alpha}<1-\frac{\omega^{c\,2}_{\mathbf{q}}}{\chi^2}. \tag{5.28}$$

It can be seen that the condition above is certainly satisfied when the photon frequency $\omega^c_{\mathbf{q}}$ is below the ionization threshold, which means $\omega^c_{\mathbf{q}}/\chi<1$. For the opposite case ($\omega^c_{\mathbf{q}}>\chi$), Eq. 5.27 has to be solved to verify that the light-matter coupling is strong enough to push one of the coupled mode below the continuum edge.

5.4 Bound Exciton States

Let us assume that one of the coupled mode $\omega^d_{s,\mathbf{q}}$ is below the continuum edge, and let us study its properties. This mode results as a superposition of photonic and matter excitations, but although the electronic transitions are all in the continuum range, and as such all the available final states are delocalised, its matter part weighted by the coefficients $y_{s\alpha q}$ and $w_{s\alpha q}$ in Eq. 5.22 describes a bound excitonic state non present in the uncoupled Hamiltonian, and as such generated by the coupling with the photon field.

By defining the electron density operator

$$N(z) = \sum_{\mathbf{k}} \mathbf{\Psi}^{\dagger}_{\mathbf{k}}(\mathbf{z}) \mathbf{\Psi}_{\mathbf{k}}(\mathbf{z}), \tag{5.29}$$

we calculate the difference in electron density between the ground state $|G\rangle$ and the state with one polariton excitation

$$\Delta N_{a\mathbf{q}}(z) = \langle G|d_{s\mathbf{q}} N(z) d^{\dagger}_{s\mathbf{q}}|G\rangle - \langle G|N(z)|G\rangle \tag{5.30}$$

$$. \tag{5.31}$$

Starting from Eq. 5.22, expressing the hybrid light-matter operators in terms of the bare single electron transitions, and their definition in terms of electronic states of Eq.5.8, we calculate the commutators

$$[a_{\mathbf{q}}, N(z)] = \left[a^{\dagger}_{-\mathbf{q}}, N(z)\right] = 0, \tag{5.32}$$

$$\left[b_{(nm)\mathbf{q}}, N(z)\right] = \sum_{n'>n_{QW}} \phi_n(z)\phi_{n'}(z) b_{(n'm)\mathbf{q}} - \sum_{m'\leq n_{QW}} \phi_m(z)\phi_{m'}(z) b_{(nm')\mathbf{q}}, \tag{5.33}$$

$$\left[b^{\dagger}_{(nm)-\mathbf{q}}, N(z)\right] = \sum_{m'\leq n_{QW}} \phi_m(z)\phi_{m'}(z) b^{\dagger}_{(nm')-\mathbf{q}} - \sum_{n'>n_{QW}} \phi_n(z)\phi_{n'}(z) b^{\dagger}_{(n'm)-\mathbf{q}}, \tag{5.34}$$

where n_{QW} is the number of quantum wells equal to the number of bare electronic bound states. Exploiting those commutators we are able to calculate

$$\Delta N_{s\mathbf{q}}(z) = \sum_{nn'>n_{QW}} \phi_n(z)\phi_{n'}(z) M^{nn'}_{Esq} - \sum_{mm'\leq n_{QW}} \phi_m(z)\phi_{m'}(z) M^{mm'}_{Gsq}, \tag{5.35}$$

with

$$M^{nn'}_{Esq} = \sum_{m\leq n_{QW}} \left[\tilde{y}_{s(nm)q}\tilde{y}_{s(n'm)q} + \tilde{w}_{s(nm)q}\tilde{w}_{s(n'm)q}\right], \tag{5.36}$$

$$M^{mm'}_{Gsq} = \sum_{n>n_{QW}} \left[\tilde{y}_{s(nm)q}\tilde{y}_{s(nm')q} + \tilde{w}_{s(nm)q}\tilde{w}_{s(nm')q}\right]. \tag{5.37}$$

Noticing that

$$\int dz \sum_{nn'>n_{QW}} \phi_n(z)\phi_{n'}(z)M_{Esq}^{nn'} = \int dz \sum_{mm'\leq n_{QW}} \phi_m(z)\phi_{m'}(z)M_{Gsq}^{mm'}$$
$$= \sum_{\substack{n>n_{QW}\\ m\leq n_{QW}}} \left[\tilde{y}^2_{s(nm)q} + \tilde{w}^2_{s(nm)q}\right] \tag{5.38}$$

as required from charge conservation, we can thus write

$$\Delta N_{s\mathbf{q}}(z) \;=\; P_{sq}\left[|\psi^e_{sq}(z)|^2 - |\psi^g_{sq}(z)|^2\right], \tag{5.39}$$

where the matter component weight is given by

$$P_{sq} \;=\; \sum_{\substack{n>n_{QW}\\ m\leq n_{QW}}} \left[\tilde{y}^2_{s(nm)q} + \tilde{w}^2_{s(nm)q}\right], \tag{5.40}$$

and the normalised ground and excited electron densities read

$$|\psi^g_{sq}(z)|^2 \;=\; \frac{1}{P_{sq}} \sum_{mm'\leq n_{QW}} \phi_m(z)\phi_{m'}(z)M_{Gsq}^{mm'}, \tag{5.41}$$

$$|\psi^e_{sq}(z)|^2 \;=\; \frac{1}{P_{sq}} \sum_{nn'>n_{QW}} \phi_n(z)\phi_{n'}(z)M_{Esq}^{nn'}. \tag{5.42}$$

5.4.1 Numerical results

We now present the numerical results obtained by applying the bound-to-continuum strong coupling theory to the case of n_{QW} identical doped GaAs/Al_x Ga_{1-x}As quantum wells heterostructure of width $L_{QW} = 4nm$. The alluminium concentration of $x = 0.33$ has been chosen to ensure the existence of a single bound state per quantum well. The single particle electronic bare wavefunctions are calculated by imposing Bastard continuity boundary conditions and solving the resulting system of $2\times n_{QW}+1$ equations in the effective mass approximation (see Appendix B). These wavefunctions has been used to calculate the electronic parameters appearing in the coupling parameter of the full Hamiltonian, which is numerically diagonalised by multimode Hopfield-Bogoliubov approach. This leads to the determination of the eigenfrequencies ω^d_{sq} and the Hopfield coefficients playing a role in the

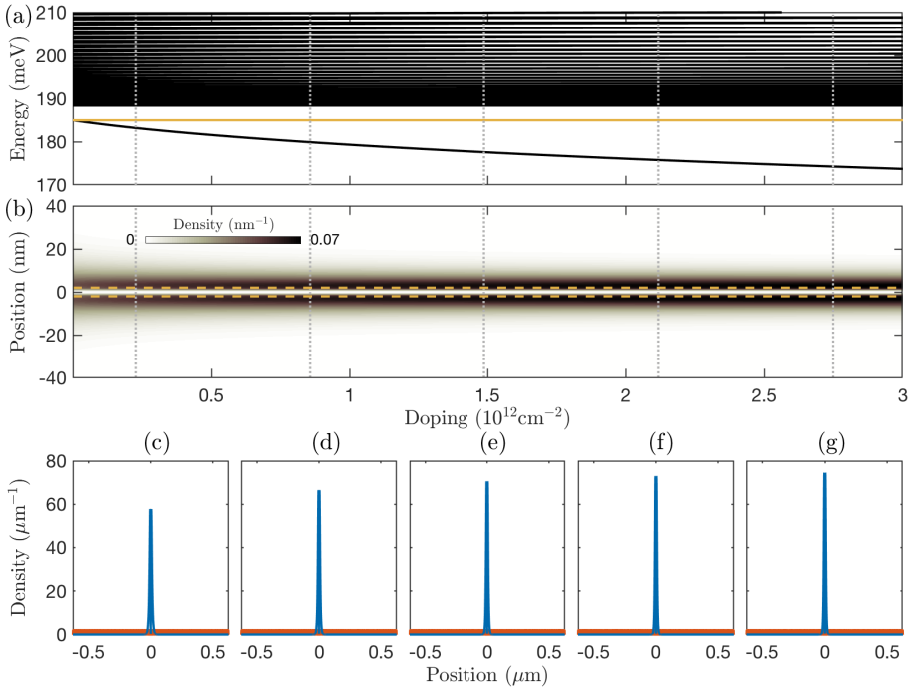

Figure 5.7: Simulation of a single quantum well of width $L_{QW} = 4$nm in a bulk of total width $T = 1\mu$m, with effective cavity length $L_c = 25nm$ and cavity energy $\hbar\omega_q^a = 185$meV, smaller than the first ionisation $\hbar\chi = 188.4$meV. (a) Polaritonic spectrum as a function of the doping. The yellow line marks the cavity energy. (b) Colormap of the excited electron density $|\psi_{sq}^e(z)|^2$ for the lowest lying polaritonic mode as a function of doping. Yellow dashed lines mark the boundaries of the quantum well. (c-g) Plots of $|\psi_{sq}^e(z)|^2$ for all the polaritonic modes (all the s up to the cutoff) relative to the five values of doping marked by dotted vertical grey lines in panels (a,b). The lowest lying mode represented in panel (b) is plotted in blue, all the other modes in the continuum are instead coloured in red, forming the thin homogeneous red band of density T^{-1} visible at the bottom of each panel. Note that, due to the different scale, the node of the lowest lying localised electronic density visible in panel (b), is not clearly resolved in panels (c-g).

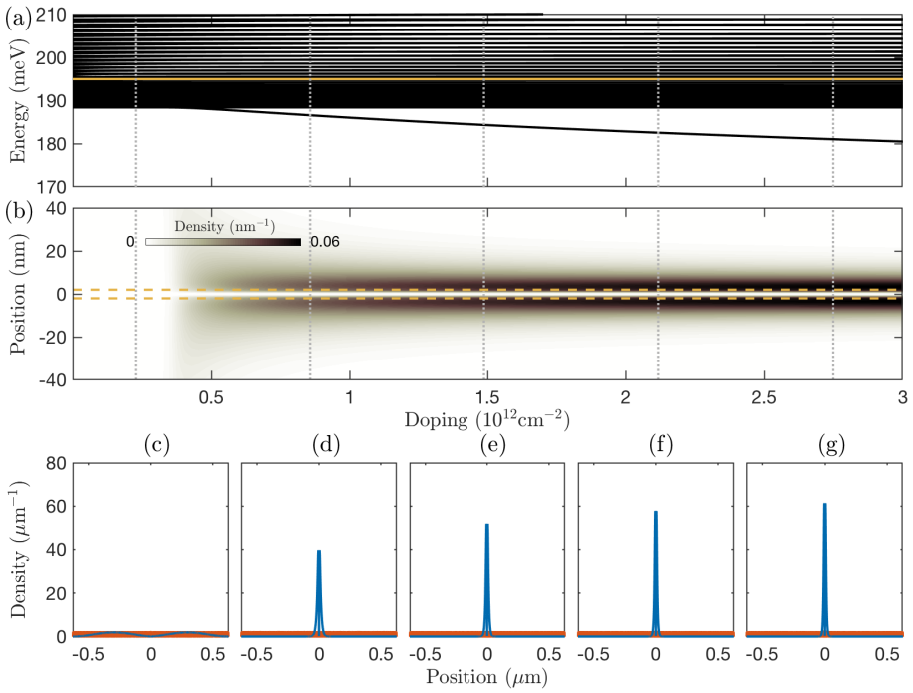

Figure 5.8: Same as in Fig. 5.7 but with cavity energy $\hbar\omega_q^a = 195$meV, larger than the first ionisation $\hbar\chi = 188.4$meV.

ground and excited electronic densities $|\Psi^g_{sq}|^2$ and $|\Psi^e_{sq}|^2$, and moreover the matter weight P_{sq}.

We here present the numerical results obtained for the cases of a single quantum well, $n_{QW} = 1$, and multiple quantum wells, $n_{QW} = 20$. We chose two structures characterized by the same ratio $f = N_{QW}L_{QW}/L_c$, which we refer to as *filling factor* because it quantifies how much of the cavity length is occupied by the electron gas. As explained in Ref. [101], this factor come into play in the so called "semiclassical approximation", made by substituting in Eq. 5.16 the product $f^o_\alpha f_\alpha$ with its maximum value L_{QW}/L_c, and it plays a crucial role in quantifying the light-matter coupling of a microcavity-embedded-quantum-wells structure.

$\mathbf{N_{QW} = 1}$ In order to provide solid basis for the good understanding of the physics of bound to continuum strong coupling, we start by considering a single quantum well in a wide bulk of width $T = 1\mu m$, which succeeds in modeling a realistic ionising continuum where the electron can get lost. In order to get large values of the light-matter coupling we choose to couple electronic transition of wavelength λ to a subwavelength photon resonance with effective cavity length $L_c << \lambda$. Specifically, we fix the cavity length $L_c = 25$ nm ($f = 0.16$), which implies $\frac{\lambda}{2L_c} \approx 125$ in quasi-resonance. This is nowadays an achievable value in mid-infrared experimental systems [106, 107, 96, 98, 108]. The results for different values of the cavity energy are shown in Figs.5.7,5.8 and 5.9, specifically with $\hbar\omega^a_q = 185\,, 195$ and 205meV. The first panel (a) of each figure displays the polaritonic spectrum as a function of the doping level, with ionisation threshold at $\hbar\chi = 188.4$meV. We can clearly observe that a single discrete mode is present for every values of doping in Fig.5.7, when $\omega^a_q < \chi$. while only above a certain doping threshold when $\omega^a_q > \chi$. This is because, when the photon energy is smaller than the ionization threshold, the electrons cannot acquire enough energy to jump and get lost in the continuum, remaining bound for any light-matter coupling.

If the cavity energy is above the ionization level, above a certain doping, the coupling is strong enough to push the coupled mode out of the continuum, forcing the excitonic state to be bound. In panel (b) we plot the spatial distribution in the z-direction of the normalised excited state density $|\Psi^e_{sq}(z)|^2$ for the lowest polariton mode, calculated as in Eq. 5.42. It is showed indeed that a discrete polaritonic resonance corresponds to a localised electronic state, which means that a bound exciton is formed. The difference between

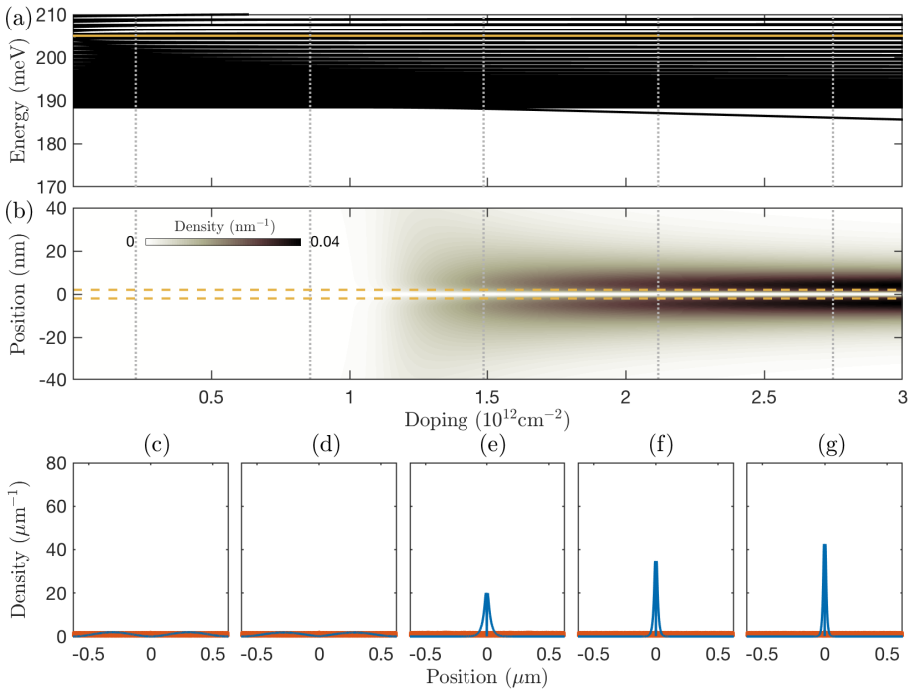

Figure 5.9: Same as in Fig. 5.7 but with cavity energy $\hbar\omega_q^a = 205$meV, larger than the first ionisation $\hbar\chi = 188.4$meV.

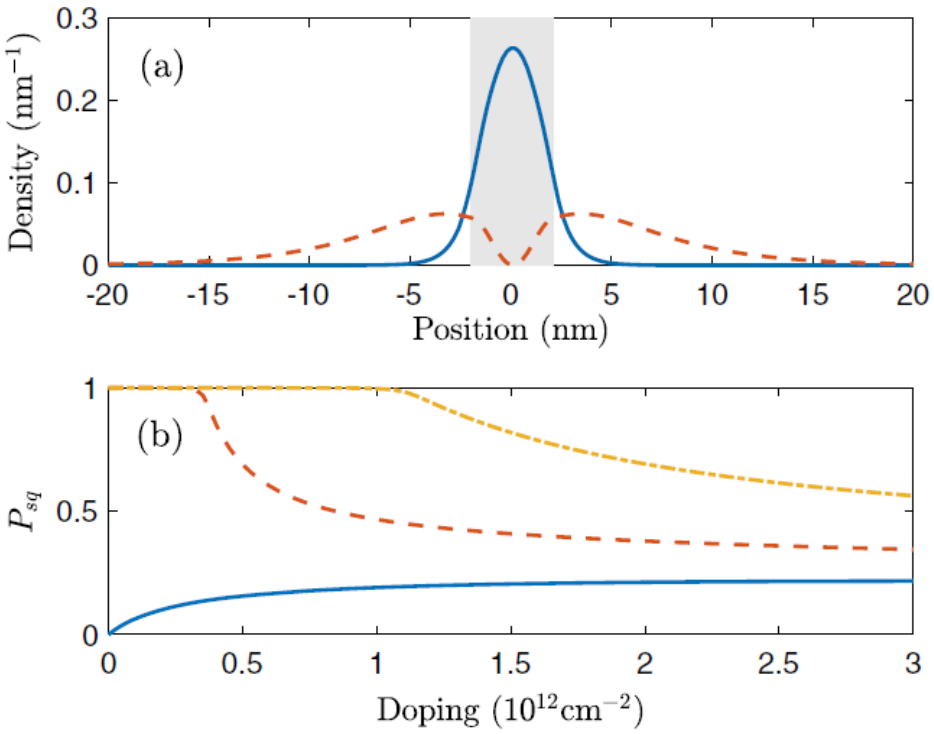

Figure 5.10: (a) Ground (blue solid line) and excited (red dashed line) electronic densities corresponding to the lowest eigenmode in Fig. 5.7(g). The shaded region corresponds to the quantum well. (b) Weight of the matter component P_{sq} for the lowest-lying polaritonic mode as a function of doping for $\hbar\omega_q^a = 185$meV (blue solid line), $\hbar\omega_q^a = 195$meV (red dashed line), and $\hbar\omega_q^a = 205$meV (yellow dashed–dotted line). Other parameters as in Fig.5.7

.

the energy of first ionisation and the energy of the discrete polariton mode plays as binding energy for the exciton, being the excess of energy the matter component of the polariton needs to dissociate. Let us notice that, at low enough temperature, the discrete polaritonic resonance is expected to have a linewidth of the order of few meV, not having enough energy to fall within the continuum. This is sizeably smaller than the predicted shifts induced by the light-matter coupling, making those resonances spectroscopically observable. In panels (c)-(g) we plot the excited electronic densities $|\Psi^e_s(z)|^2$ for all the polaritonic modes (below a cutoff energy of 500 meV), at different values of the doping, in order to demonstrate that no bound excitonic states correspond to the coupled modes forming a continuum below the doping threshold. All the electronic densities for all the s coupled modes, except the one corresponding to the lowest one, are plotted in red, and form a uniform red band, of homogeneous density T^{-1}. In the limit $T \to \infty$, such a density vanishes as expected for bound-to-continuum excitations. The curve plotted in blue which corresponds to the lowest polariton state confirms instead that a localised electronic state emerges only above a critical doping value. In the panel (a) of Fig 5.10, we plot both the ground state and excited electronic densities $|\Psi^g_{sq}|^2$ (solid blue line) and $|\Psi^g_{sq}|^2$ (red dashed line), calculated as in Eqs. 5.41-5.42 for the lowest coupled mode in a 40nm interval around the quantum well. It is clear that, while the ground state density as defined in Eq. 5.30 corresponds to the initially fully occupied electronic state, the excited state density corresponds to a localised odd-symmetry wavefunction. Of course the normalised electronic density $|\Psi^e_{sq}|^2$ suggests us only partial informations about the observability of cavity-induced bound exciton states, because from Eq.5.30 it is weighted by the matter fraction P_{sq}. In panel (b) of Fig.5.10 $|\Psi^e_{sq}|^2$, calculated by Eq. 5.40 for the mode considered in panel (b) of Figs. 5.7-5.9, is plotted as a function of the doping, for each of the three considered values of the cavity energy. As expected, the matter weight of the lowest coupled mode is negligible where the cavity energy is below the continuum ($\hbar\omega^a_q = 185$ meV, blue solid line), because it is almost entirely the bare cavity mode. For the remaining two cases ($\hbar\omega^a_q = 195$ meV, red dashed line, $\hbar\omega^a_q = 205$ meV, yellow dash-dotted line), the lowest mode is initially purely matter ($P_{sq} = 1$) and only when we observe the discrete polariton mode appearing below the continuum it starts hybridising with light.

$\mathbf{N_{QW} = 20}$ After having studied the single quantum well case, demonstrating the appearance of a cavity-induced bound exciton state for experimentally achievable values of the light-matter coupling, in this paragraph we consider a more realistic heterostructure of $n_{QW} = 20$ quantum wells coupling to the TM0 photon mode of a planar resonator as wide as the semiconductor bulk. Considering a multiple-quantum well structure allows us to achieve more easily the light-matter coupling needed to observe the discrete polaritonic resonances emerging out of the continuum, and thus the generation of the cavity-induced bound exciton states. Our sample consists of $n_{QW} = 20$ quantum wells of width $L_{QW} = 4$ nm sandwiched between 20 nm wide barriers. The bulk and the resonator have a total length $L_c = T = 0.5\mu$m.

In Fig. 5.11 we show the eigenmodes for a cavity energy $\hbar\omega_q^a = 195$ meV. Here we observe a quasi-continuum of states grouped in minibands, due to the spatial periodicity of the QWs. In such a system the first ionization energy $\hbar\chi = 192$ meV reveals to be larger than in the previous case. Nevertheless, the results recovered here are in good agreement with those in Fig. 5.8 (a) showing that a discrete resonance below the continuum is observable also in a multiple- quantum well structure. Panels (b) and (c) display the excited electronic density of the lowest polariton mode for the extreme values of the doping range considered, that are $N_{2DEG} = 0$ and $N_{2DEG} = 3 \times 10^{12}$ cm^{-2}, marked by arrows in panel (a). A visible difference arises between the single and multiple-quantum well cases: the ionised states of a single quantum well did not exhibit any sort of localisation, but their electronic density was highly delocalised throughout the bulk, while in the multi quantum wells case, as expected, the electronic density of a continuum state seems to maintain a confinement in the proximity of the wells, as in a multiple-quantum wells structure the total space occupied by the quantum wells is now a macroscopic fraction of the total width of the bulk. Nevertheless, we can recognise the same physics, as the collective excited electronic density at zero doping, although modulated by the presence of the well, describes a mode which is of the entire structure with maximal magnitude at the center, while instead, at high doping level, it corresponds to a mode localised in each quantum well.

At the end of our theoretical study, we test its accuracy and provide an experimentally suitable observable, by calculating the reflectivity of the same heterostructure coupled to a planar metallic resonator via transfer matrix approach in effective medium approximation including local field effects, that has been treated in several theoretical works [105, 109, 110, 111]. Results are shown in Fig.5.12, which recover pretty well the eigenmodes spectrum

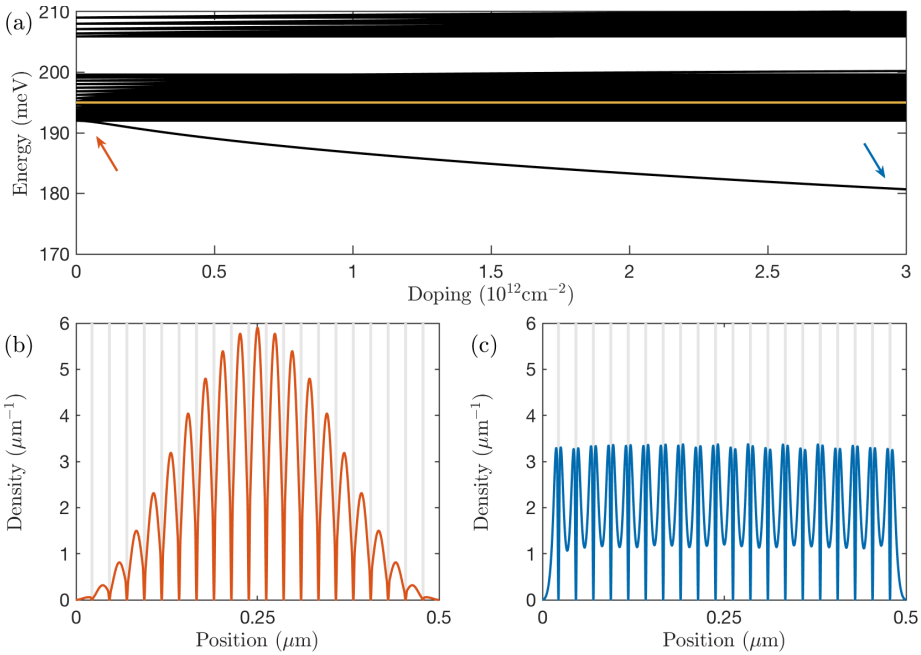

Figure 5.11: Simulation of $n_{QW} = 20$ quantum wells of width $L_{QW} = 4$nm in a bulk of total width $T = 0.5\mu$m embedded in a planar microcavity. The TM0 mode of the microcavity is chosen to have energy $\hbar\omega_q^a = 195$ meV, larger than the first ionisation energy $\hbar\chi = 192$ meV. (a) Polaritonic spectrum as a function of the doping. The yellow line marks the cavity energy. (b,c) Plots of the excited electron density $|\psi_{sq}^e(z)|^2$ for the lowest lying polaritonic mode, for values of doping equal respectively to $N_{2DEG} = 0$ and 3×10^{16} cm^{-2}, marked by arrows in panel (a). Shaded regions correspond to the locations of the quantum wells.

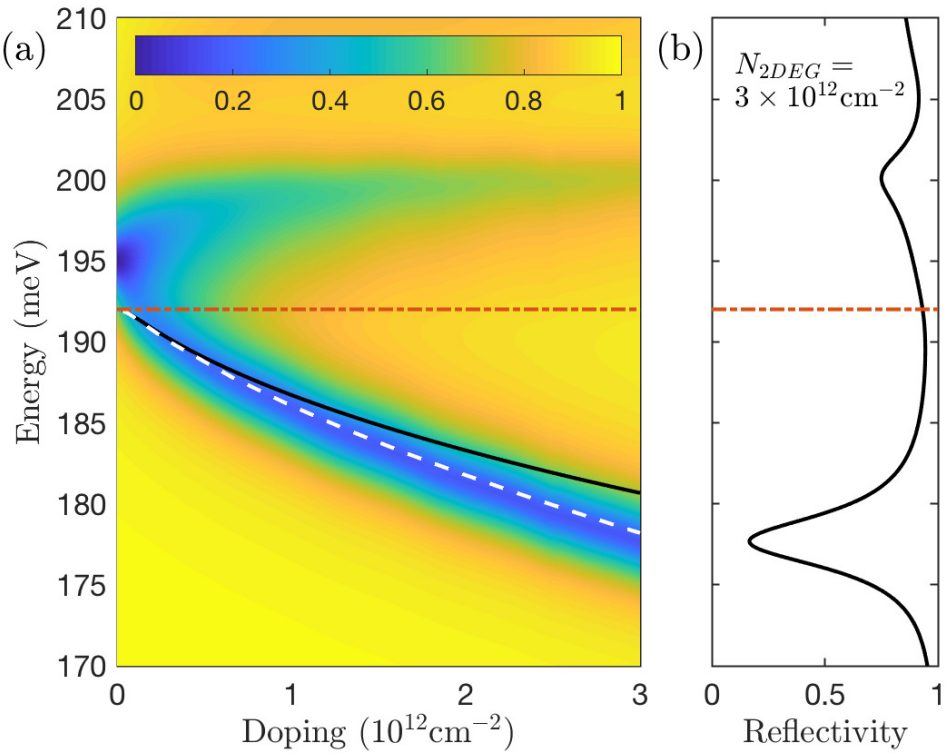

Figure 5.12: (a) Reflectivity map for the same structure studied in Fig. 5.11, calculated considering an electronic linewidth of 4meV. The horizontal dash-dotted red line marks the first ionisation energy. The solid black and dashed white lines mark instead the dispersion of the lowest polariton mode obtained using the Hopfield approach respectively without and with the effective medium approximation. (b) A vertical cut of panel (a) for $N_{2DEG} = 3 \times 10^{12}$ cm^{-2}.

of Fig. 5.11 (a). The lowest polariton mode calculated by Hopfield method (black solid line) is superimposed on the reflectivity map, and its small deviation from the reflectivity dip is due to the use of an effective medium approximation. We verified the origin of this discrepancy by implementing the same approximation in the Hopfield theory leading to a "approximated" mode (white dashed line) which is in a definitely better agreement with the reflectivity spectrum.

5.5 Experimental Results

The promising result of creating cavity-induced bound exciton states obtained by the theoretical calculation finds its definitive demonstration in the experimental measurements run by the experimental group of Prof. Colombelli in the *Centre de Nanosciences et de Nanotechnologies (C2N)* in Paris, who is also co-author of the theoretical work.

The system under investigation is similar to the one considered for the numerical calculations, and it is composed of $N_{QW} = 13$ GaAs/AlGaAs quantum wells embedded in highly-confined, grating-shaped gold microcavity resonators. They are 1D ribbons (or 1D patch cavities), and the electromagnetic field, as sketched in Fig. 5.2.2(b), is completely confined below the gold fingers. As in the theoretical study, the QWs are designed thin enough to ensure the presence of only one conduction subband, in order to avoid intersubband transitions giving arise to intersubband polaritons.

In order to determine the nature of the transition coupled to the single cavity photon mode, two samples, HM4229 and HM4230, differing in QW width and doping, are fabricated. Sample HM4229 contains QWs of thickness $L_{QW} = 4$ nm, each doped at a density 5×10^{12} cm^{-2}, while sample HM4230 has QWs of thickness $L_{QW} = 3.5$ nm doped at 4.77×10^{12} cm^{-2}. Comparing the transmission spectra of these two samples, plotted in Fig. 5.14 (a), allows us to determine whether the optically active transition is a bound-to-bound or bound-to-continuum. The two, indeed, undergo opposite frequency shifts when the quantum well width is reduced: The former ones blue-shift, as the energy difference between two subbands is inversely proportional to the L_{QW}, while the latter ones red-shift, because a single subband is lifted up as L_{QW} decreases. This difference of behaviour is sketched in panels (b)-(e) of Fig 5.14. In panel (a) we observe a very broad absorption that, being transverse magnetic polarized, is clearly originated from the doped QWs, and, moreover,

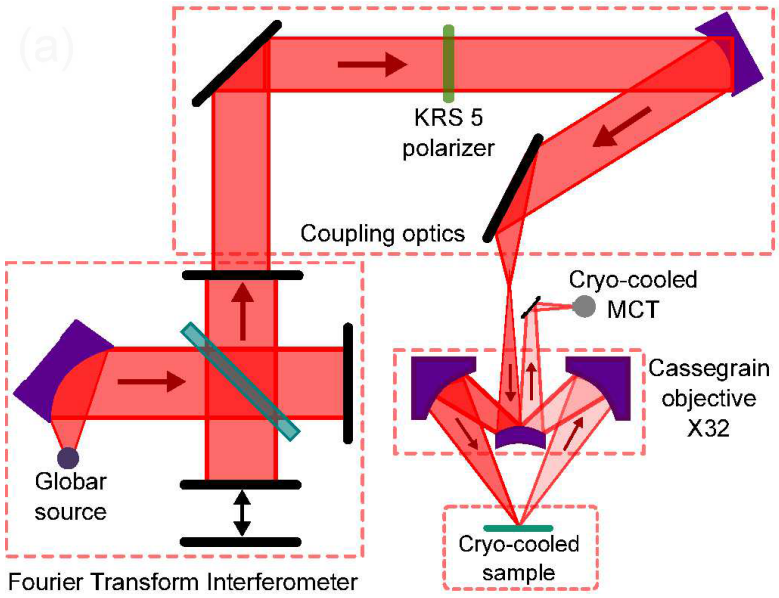

Figure 5.13: Scheme of the experimental setup employed for the reflectivity measurements. It consists of a mid-IR microscope connected to an FTIR spectrometer. The source is a thermal globar lamp, and the detector is a liquid nitrogen cooled MCT. The incident beam is polarized normally to the metallic fingers, and the system operates in reflection. A compact, thin cryostat permits to perform the measurements down to a temperature of 78K.

some narrower feature around 140 meV which we can identify as the edge of the continuum. This feature does not blue-shift as the QW width decrease. It shows a transfer of spectral weight toward the lower-frequency range, while a bound-to-bound intersubband transition would have led to a blue-shift of the order of tens of meVs. This definetely proves the bound-to-continuum nature of the transitions in the uncoupled QWs system. Fig. 5.13 show the experimental set up, including the metal-semiconductor-metal grating resonators with period D and width of metallic stripes p, showed in Fig. 5.2.2 (a). Details about the resonators and their mode frequency dispersion are preliminarly presented in Sec. 5.2.2.

The grating-based devices are fabricated 200 $\times$ 200 μm^2 large, with p ranging from 800 nm to 5 μm, to span a wide range of frequencies (Fig. 5.13

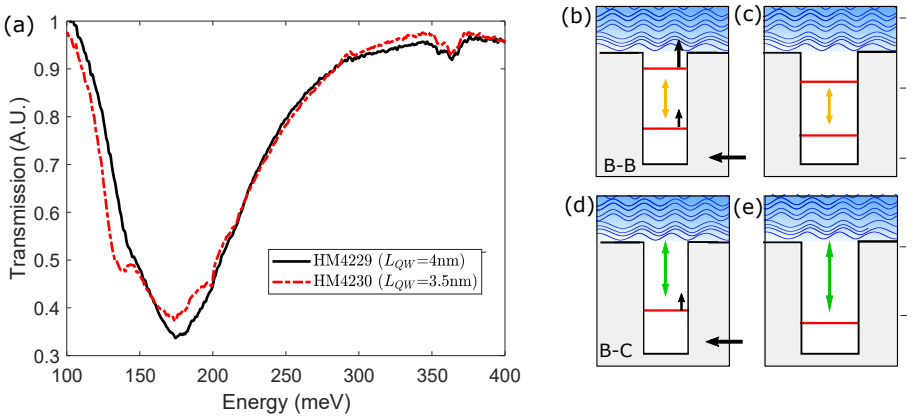

Figure 5.14: **Bound-to-continuum nature of the transition.** (a) The black solid line is the transmission measured at 300K from the sample HM4299, with $L_{\mathrm{QW}} = 4$ nm. The red dashed line represent instead sample HM4230, with $L_{\mathrm{QW}} = 3.5$ nm. In the inset we sketch how the transition frequency shifts as a function of the quantum well width for bound-to-bound (b,c) and bound-to-continuum (d,e) transitions.

(b)). We remind that the frequency dispersion for this kind of resonator is expressed in Eq. 5.2. The cavity mode employed here to strongly couple to the matter system is the one with $m = 2$, instead of the fundamental one with $m = 0$, named TM_{02} that is typically used in these systems, in order to simplify the fabrication process and increase the overlap between the electromagnetic field and the quantum wells, as visible in Fig. 5.13(c) that highlights three nodal lines for the considered TM_{02} mode. For each device a measurement in reflectivity is performed, at temperature T=78K, using a FTIR microscope (Fig. 5.13(a)). Figs. 5.15-5.17 displays the main experimental results relative to the HM4229 sample. In Fig.5.15 we plot the 78 K reflectivity map as a function of the bare resonator energy, where we observe an absorption continuum above the first ionization energy (black horizontal dashed line), and a narrow discrete polaritonic resonance below it. The latter lies more than 20 meV below the uncoupled resonator energy. We plot superimposed on the colormap the peak frequencies obtained by a multiple lorentzian peak fitting procedure of the experimental data sets for each width value of the metal finger. Same procedure is employed to extract the bare

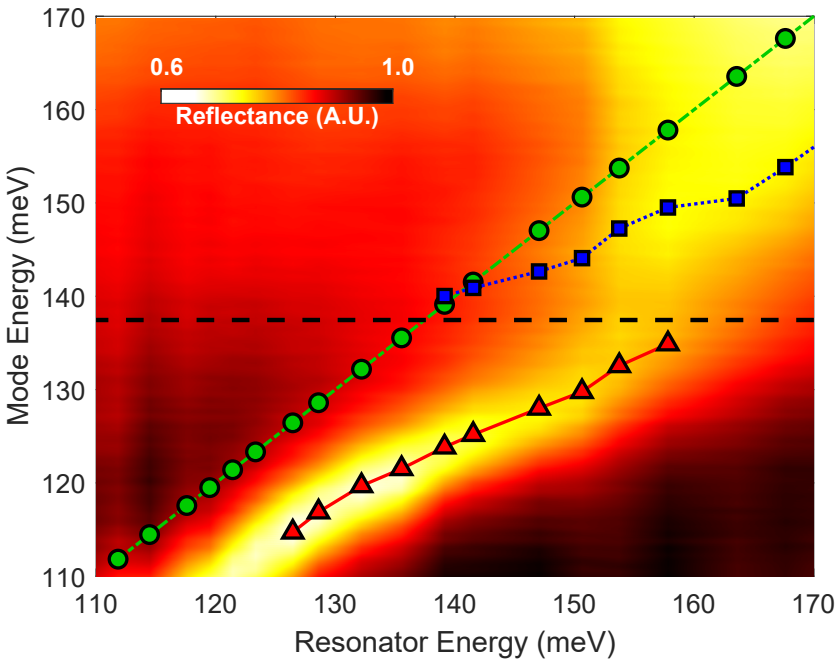

Figure 5.15: **Experimental reflectivity data** Reflectance data from the doped sample HM4229 as a function of the resonator frequency. Superimposed we show the peak position extracted from the data, using blue squares and red triangles for the datapoints respectively below and above the edge of the continuum. With green dot we mark instead data from the undoped sample taken as reference for the cavity energy.

cavity resonances from an undoped sample. In Fig. 5.15 the frequencies below and above the identified ionization threshold are marked respectively by red triangles and blue squares, while the frequency of the uncoupled resonator are marked by green circles. Fig. 5.17 shows the respective linewidths as a function of their mode frequency. These are extracted as lorentzian peaks linewidths by the same fitting procedure. Below the edge of the continuum (vertical black dashed line) the lifetime of the discrete polariton has as main contribution the lifetime of the bare resonator mode. Beyond the ionising threshold, instead, we observe a very broadened undefined feature, clearly corresponding to a continuum spectrum. Let us notice that in Fig. 5.15

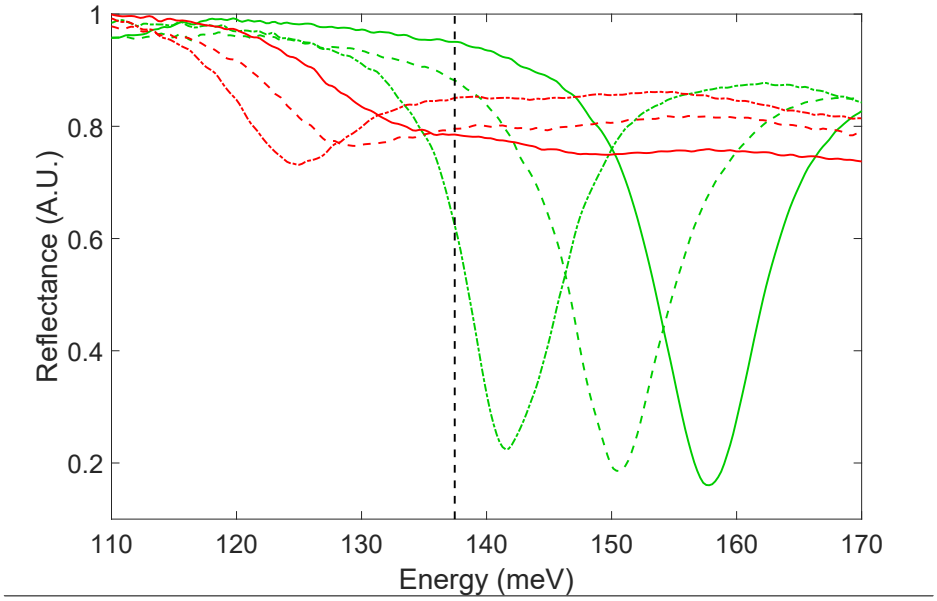

Figure 5.16: Reflectance data for doped sample HM4229 (red) and the empty cavity (green) for resonator frequencies $\hbar\omega_c = 157.8\,\text{meV}$ (solid), $\hbar\omega_c = 147\,\text{meV}$ (dashed), and $\hbar\omega_c = 141.5\,\text{meV}$ (dot dashed).

both the narrow discrete mode (red) and the extracted peak of the broad spectrum are at frequency lower than the bare resonator frequency (green). Moreover, they maintain very different linewidths, which do not cross at any point. This feature is incompatible with the standard intersubband polariton description, where the light and matter resonances are enclosed between the polariton modes, and the coupled mode linewidths, as the result of a weighted linear combination of the bare ones in the simple Hopfield model, should cross at the anticrossing point. In order to make even more evident the appearance of a strong-coupling-induced discrete resonance below the continuum, we plot in Fig. 5.16 the reflectivity spectra of the doped sample (red curves) for different values of the bare resonator energy, together with the reflectivity spectra of the undoped sample (green curves). We can clearly observe that the doped sample shows a discrete resonance below the ionization threshold which does not exists in an identical but optically uncoupled system. The same misurements are also performed on the HM4230 sample, showing very similar results.

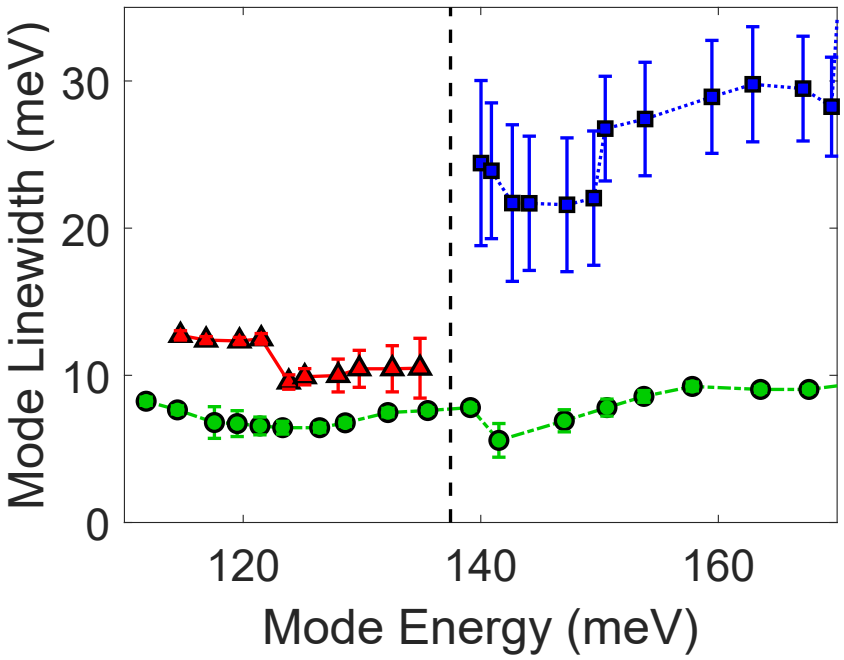

Figure 5.17: Linewidths for the different resonances, showed in Fig. 5.17, as a function of the mode energy. In all the panels the dashed black line marks the edge of the continuum.

In order to compare the developed theoretical model with the experimental data, we calculate the polariton spectrum to match the experimental reflectivity map (Fig. 5.18(a)), using using the doping and the ionization energy as adjustable parameters. By the parameters obtained by the simulation, we calculated the matter weight P of Eq. 5.30, which is plotted in Fig. 5.18 (b). We can observe that the discrete resonance below the continuum edge is clearly defined for non-vanishing values of P, proving a significant occupation of the cavity-induced electronic bound wavefunction $\Psi^e(z)$.

5.6 Conclusions

In this chapter, we present the theoretical prediction and the experimental demonstration of strong coupling for ionizing transitions, resulting in

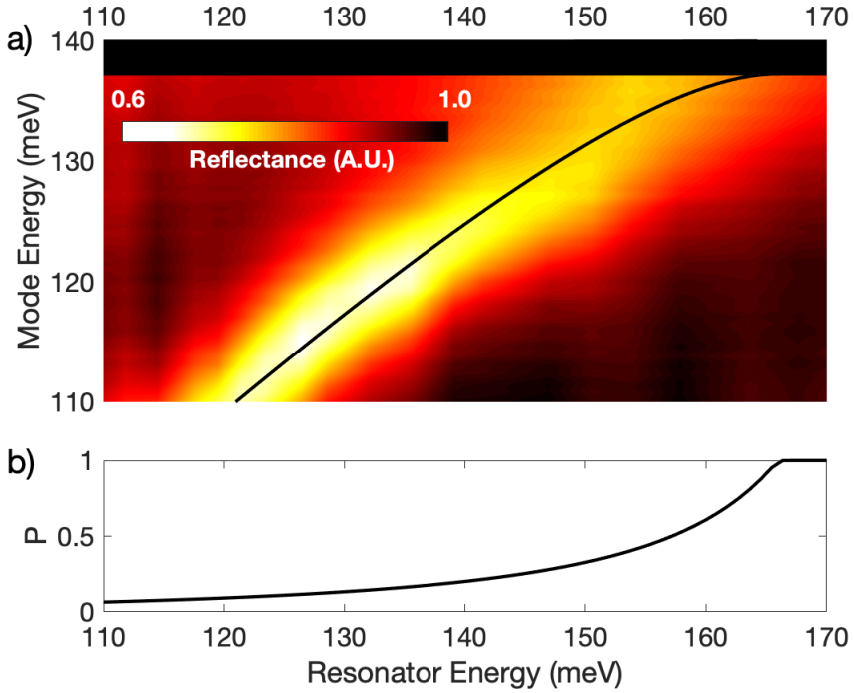

Figure 5.18: **Calculation of the matter weight.** In panel (a) we plot the eigenmodes obtained by our theoretical model with parameters choose to fit the experimental reflectance data shown in the colorplot. Above the ionization threshold the figure is uniformly black as the discrete modes used in the numerical diagonalization are too closely-spaced to be resolved. In panel (b) we use the parameters extracted from panel a) to calculate the matter fraction P of the discrete polariton mode.

a non-perturbative modification of the electronic properties of the system. The strong light- matter coupling manifests as the appearance of a discrete polariton mode below the continuum threshold, whose matter component corresponds to a new bound electronic state not present in the uncoupled system. Let us notice that the experiment shows only the optical response of the system, without giving answers about electronic transport, that means about the capability of these states to conduct current.

If these bound states could serve as a discrete and tunable current channels into the bright states, it has been predicted that they could lead to a dramatic increase in the efficiency of intersubband mid-infrared emitters [112, 113]. An initial work in this direction has recently come to light for bound-to-bound transition in mid-infrared detectors operating in strong light-matter coupling regime [114].

As the previous chapters have the purpose of proving the possibility of tuning material features, such as chemical and structural properties, by coupling them to a microcavity photonic field, here we demonstrate this concept for semiconductor heterostructures, where the cavity quantum electrodynamics can be used as too in quantum material engineering, to not only shift the resonances but also controllably change their nature.

Chapter 6

Cavity mode field hybridization by light-matter coupling

6.1 Introduction

Very Strong Coupling regime is responsible for important modifications of materials' electronic properties. This is due to the fact that the coupling strength is comparable to the spacing between different matter states leading to a multi-mode hybridization. When the coupling becomes comparable to the energy difference between several photonic modes, it is reasonable to expect that, in some circumstances, the same phenomenon occurs for the photonic counter part, not only shifting the resonances in the optical spectra, but also modifying their electromagnetic field distribution.

On this direction, an alteration of the resonator field profile has been predicted in microcavities when Deep Strong Coupling (DSC) is entered, due to the light-matter decoupling deriving from the diamagnetic term of the Hamiltonian [18]. It has also been experimentally shown that, in plasmonic nanocavities, the greatly enhanced coupling between molecular excitons and gap plasmons causes a significant modification of the plasmonic modes profile [115].

As we know, the electromagnetic field confined by a resonator can be decomposed into its modal components, characterised by an essential principle of mutual orthogonality over the whole integration volume. Each electromagnetic mode distribution depends on the geometry and the composition of the resonator, and its spatial overlap with the optically active region of a matter

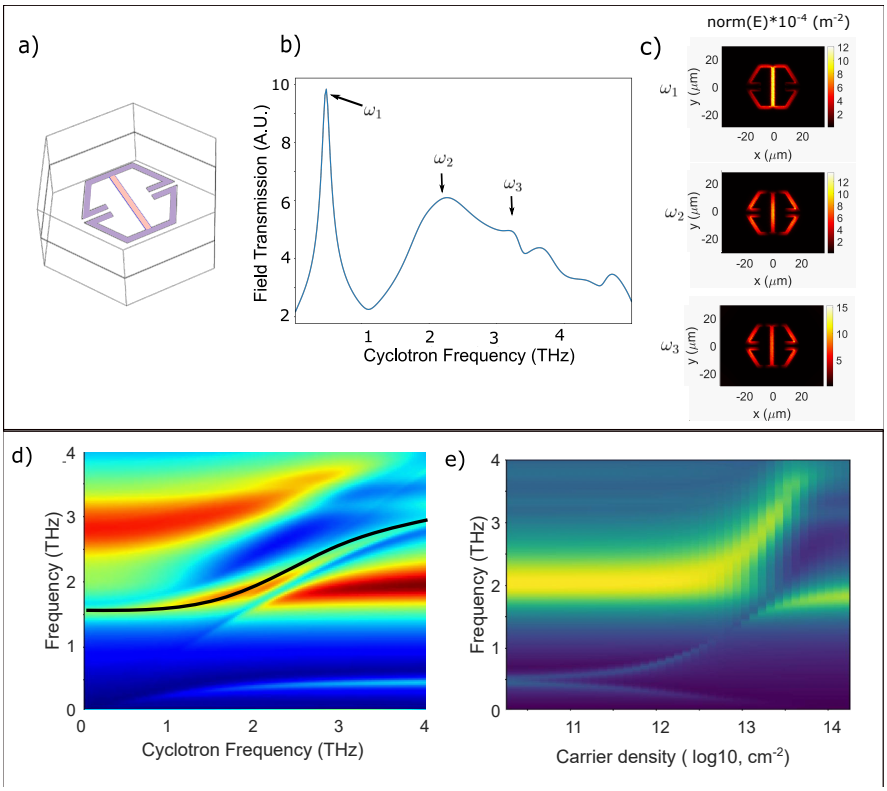

Figure 6.1: **Simulations of doped multi-QWs heterostructure with $N_{QW} = 6$, under the effect of a static magnetic field, coupled to a THz negative hexagonal metamaterial resonator.** Panel (a): Sketch of the simulated unit cell composed by a negative hexagonal metamaterial (the purple shaded region indicates where the gold is not deposited), and a narrow QWs patch, placed right in the central gap of the resonator (red shaded region). Panel (b): Transmission spectrum of the uncoupled resonator displaying peaks at the frequencies of the discrete photon modes, $\omega_1 = 0.48$ THz, $\omega_2 = 2.1$ THz and $\omega_3 = 3.2$ THz etc. Panel (c): Electric field distribution maps for each of the first three resonator modes, normalised over the sample plane. Panel (d): Transmission map of the coupled system as a function of the cyclotron frequency ω_c at fixed total doping $N_{QW} \cdot N_{2DEG} = 18 \times 10^{12}$ cm^{-2}. The black solid curve highlights the characteristic S-shape of the central resonance. Panel(e): Transmission map as a function of the doping density N_{2Deg} at a fixed cyclotron frequency $\omega_c = 0.48$ THz. All the plots have been made by Prof. Lange's group in Regersburg

system, defined as the mode volume V, is considered a key parameter for the optimization of CQED set-up design for the achievement of ever higher coupling strengths. In many kinds of resonator, such as very narrow planar cavities like the one introduced in the previous chapter, the photon modes are so far in energy, compared to the light-matter coupling, that we can describe the system in the single-mode approximation. When, instead, higher photon modes frequencies are not far enough to be neglected, single-mode approximation breaks dow and the inclusion of higher resonator resonances becomes a necessity for the correct description of the system dynamics, as demonstrated in many recent works [18, 116, 117, 118, 119]. Nevertheless, even in this last case, the orthogonality between different photon modes allows to treat them independently, as all the photon modes will excite and thus couple to different mutually orthogonal electronic excitations, forming well-known half-light half-matter polariton modes, observable as a number of independent avoided-crossings in the optical spectrum. Each pair of polariton modes will result from the hybridization of a single matter mode with a single photon mode, and, as such, its optical component, that we can picture as the mode electric field "dressed" by the interaction, will conserve the same field spatial distribution as the bare field. Therefore, we ask ourself: can the light-matter coupling manipulate the photonic field, and if yes, under which conditions?

Aiming to answer this question, we considered a specific QED system, composed by an array of THz metamaterial resonators coupled to cyclotron transition resonances of a 2DEG under the effect of a static magnetic field, similar to the one investigated in Ref. [54]. It has been first predicted [120] and then experimentally demonstrated [121] that it is possible to ultrastrongly couple the cyclotron resonances to the resonator photon field, leading to the formation of the so-called *Landau Polaritons*. In this system, due to the possibility of achieving extremely high values of the normalised light-matter coupling by simply tuning the electronic density of the 2DEG, more than one resonator modes have to involved in the description. Our intuition is that, due to the strong planar confinement of the electron gas, the principle of orthogonality between different photon modes may fall, because it is valid over the whole integration volume but not over the optically active region, which is the 2DEG plane. This would lead to cross interactions between electromagnetic components in the Hamiltonian, and as such a multi-mode hybridization of the dressed electronic field.

In Fig. 6.1 we show the results of Comsol numerical simulations for a

specific system , which were carried out by our collaborators of the group of Prof. C. Lange of University of Regensburg, as all the following throughout this chapter. The studied system is sketched in Fig. 6.1 (a), in which a specific hexagonal shape for the THz metameterial resonator is adopted. This specific design determines the positions of the multiple uncoupled photonic resonances ($\omega_1 = 0.48$ THz, $\omega_2 = 2.1$ THz, $\omega_3 = 3.2$ THz etc), clearly visible in the gap field transmission plot in panel (b). Moreover, Panel (c) displays instead the uncoupled electric field in-plane distributions for the first three photon modes, which appear significantly different.

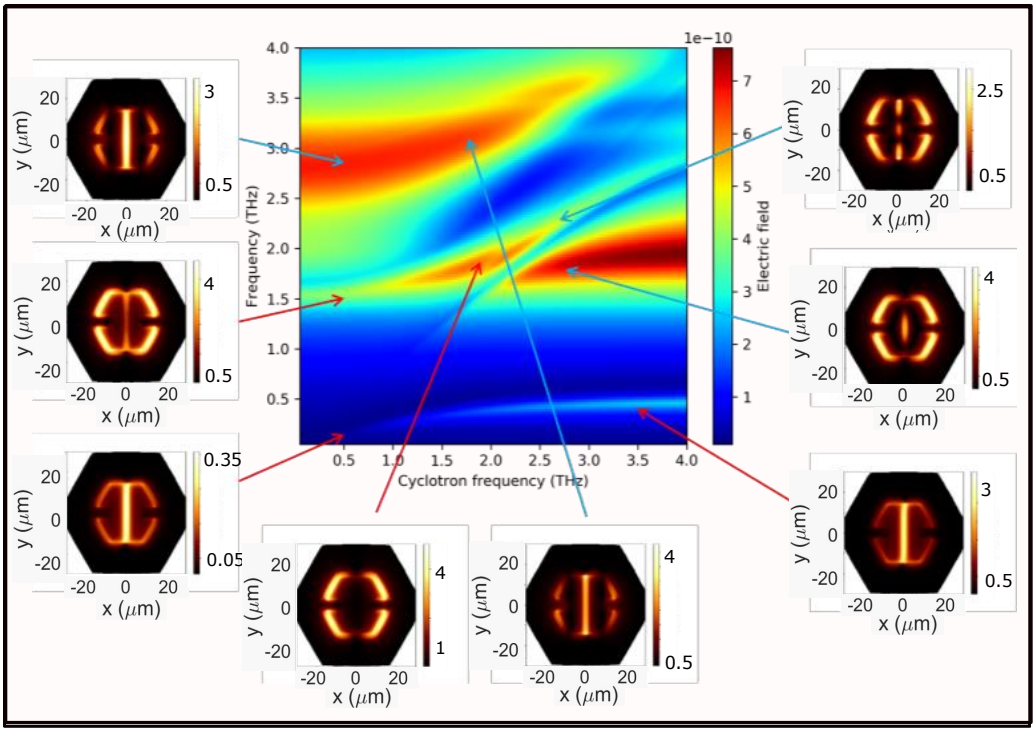

Figure 6.2: **Coupled modes' electric field distribution maps** The figure refers to the same system described in Fig.6.1. It displays the simulated in-plane electric field enhancement for each of the polariton resonances observable in the transmission spectrum as a function of the cyclotron frequency, showing how, as the mode frequencies hybridize near the avoided crossing, also the electric field maps undergo observable modifications. Plots are made by Prof. Lange's group

Fig. 6.1(d)-(e) show the simulated transmission spectra as a function, respectively, of the cyclotron resonance frequency and the two-dimensional electron density. Both the spectra clearly exhibit at least five well resolved Landau polariton resonances, derived from light-matter hybridization between multiple resonator discrete modes and degenerate cyclotron transition modes. If we observe the transmission spectrum in panel (d), calculated at a fixed total electron density 18×10^{12} cm^{-2}, we notice very large splittings between different resonances, due to large coupling strengths, leading to a no longer trivial identification of their nature. Moreover, the third coupled mode (counting by ascending order) results having a peculiar s-shape, underlined by a black-solid curve, likely suggesting that a single matter excitation is not strongly coupled only to the fundamental photon mode, but also to the one at higher frequency [120, 122]. A second interesting feature is, instead, visible in panel(e). Here the transmission resonance branches typically split as the electron density increases: the lower polariton frequency, starting at the cyclotron frequency, decreases never crossing the zero, and the upper polariton resonances are pushed up by the coupling strength, while they converge into the bare photon frequencies at zero doping. However, what is here worthwhile to notice is that the two visible upper polariton modes undergo an avoided crossing around a critic total doping value of 1.8×10^{13} cm^{-2} (in this plot the electron density is in logarithmic scale). This appear as an "anomalous" behaviour, since polariton modes derived from different photon modes, in general, proceed independently, unless we assume a sort of mutual interaction occurring between the resonator modes. Another hint is given by the investigation of the coupled modes field distributions. Each polariton mode is characterized by its characteristic in-plane electric field map, displayed in Fig. 6.2 for different values of the cyclotron frequency. As highlighted in Ref. [54], mapping the polariton modes electric field allows to determine their photon component, and as such, by comparison, to identify which of the bare photon modes they derive from. Nevertheless, we notice here that, as the resonances approach the anti-crossing point, their in-plane electric field distribution changes, until they may become significantly different from the original ones (Fig.6.1 (c)). This modification of the electromagnetic field distribution induced by the coupling is clearly not predictable when we consider the photon modes independently coupled to mutually orthogonal matter modes. In order to give a theoretical and physical explanation to the results of these simulations, we must call into play a multi-photon-mode interaction, due to a non-negligible spatial overlap between the photon modes within the

strongly two-dimensional active region. The latter is formally quantified by an overlap paramenter ranging from 0 (no overlap means orthogonality) to 1 (complete overlap). Formally, the light-matter interaction Hamiltonian will no longer be a sum of N one-to-one interaction terms between N discrete photon modes and N matter excitations, but it will present $N \times N$ cross-interaction terms.

We here develop a formal multi-mode bosonic theory for USC of cyclotron resonances coupled to metamaterial resonators, which assumes the in-plane non-orthogonality, between different resonator modes, allowing to recover the main peculiar spectral features showed by the simulations results. By simultaneously fitting both the cyclotron-frequency-sweep and doping-sweep spectral resonances, for several kind of resonator and QWs designs, we show that the developed theory not only succeeds to explain the behaviour of the polariton modes, but it is also able to seemingly reproduce the electric field distribution maps for each of the coupled states, as linear combinations of the bare photon modes electric fields weighted by Hopfield coefficients. As specified in the overall introduction, the results presented in this chapter are only preliminary, and they refer to different kinds of resonator and QWs geometries, in order to address several levels of the multi-mode spatial overlap and hybridization.

6.2 Quantum system

In this section, we briefly present the quantum system considered in our study. Although we explored doped quantum well heterostructures in the previous chapter, with particular interest in intersubband and bound-to-continuum transitions, we focus here on cyclotron transitions, occurring when the 2DEG is object of an intense static magnetic field, which leads to the formation of discrete Landau levels. We here consider the transitions between different Landau levels coupled to an array of THz metamaterial resonators, characterized by a high sub-wavelength confinement [121, 54].

6.2.1 Cyclotron Resonances in doped QW

When a magnetic field is applied to the 2DEG in a quantum well heterostructure, we obtain magneto-cyclotron transitions between equispaced electronic Landau levels. A scheme of the levels is shown in Fig.6.3. The cyclotron

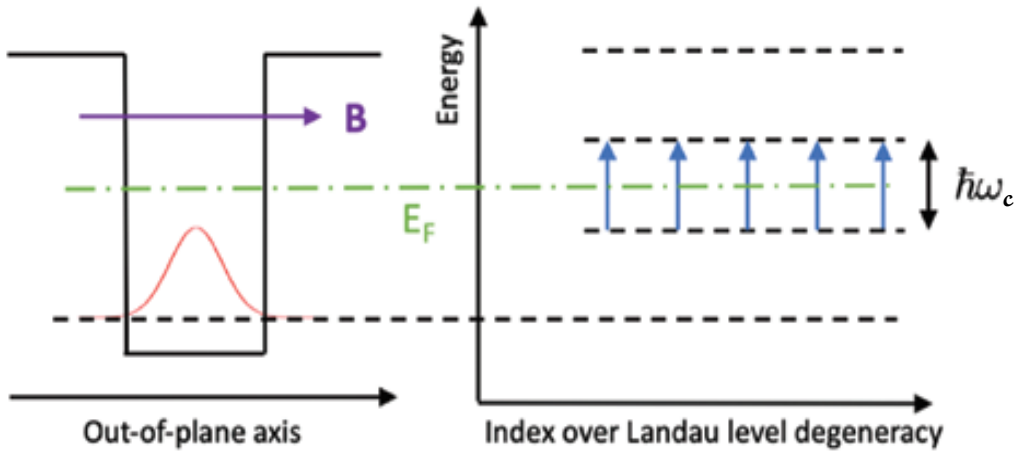

Figure 6.3: Transition between different Landau levels in a 2DEG under applied magnetic field. The image is taken from Ref.[108]

transition frequency is $\omega_c = \frac{eB}{m^*}$, where B is the applied magnetic field, e is the elementary charge, and m^* is the electron effective mass. Cyclotron transitions are thus characterized by a high tunability, and a dipole moment d scaling as $el_0\sqrt{\nu}$, where $l_0 = \sqrt{\frac{\hbar}{eB}}$ is the magnetic length and ν the filling factor depending on the 2DEG density. In general the resolved cyclotron transitions' dipole moments are giant because of their proportionality upon very high levels degeneracy [121].

6.2.2 THz Metamaterial Resonator

On the photonic side, different kinds of both diffraction-limited and sub-wavelength resonators have been used to couple to cyclotron resonances, including strip-line resonators [123], and DBR resonators [124], but the current record for the absolute highest value of the normalised light-matter coupling η of 1.43 [54] is achieved by employing THz metamaterial resonators [125]. These consist of an array of independent resonators fabricated on the surface of a semiconductor substrate by deposition of a few-hundreds-nm thick metal layer in a specific designed pattern, which determines their optical properties, such both resonance frequencies and mode volumes. In the fol-

lowing we will refer to gold gaped metamaterial resonators, similar to the ones employed in [121, 54]. These can be of two kinds: positive or negative resonators (in literature, better known as direct and complementary [126]), which means that either the gold is deposited inside the guidelines forming the frame of the single unit cell with a double capacitive gap in the center, or the design of the unit cell is inverted and the gold in deposited outside the frame. In the first case, the lowest-frequency mode is a LC mode, with capacitive elements represented by the gaps in which the electric fields are localised to decrease the mode volume. In the second case, the electric field the fundamental mode, is strongly confined into the gap in the center, and the quality factor of the resonator decreases due to the increased losses. An important advantage of the negative resonator is that, unlike the positive resonator, the transmission spectrum exhibits peaks, instead of depths, which suppresses undesired spectral features [127].

6.3 Theory of multi-mode light-matter coupling

We can express the Hamiltonian of a 2DEG of two-dimensional electron density N_{2DEG} and effective mass m^* coupled to a resonator photonic multimode field in the Coulomb Gauge as

$$\begin{aligned}\hat{H} &= \sum_{\nu}\hbar\omega_{\nu}\hat{a}_{\nu}^{\dagger}\hat{a}_{\nu}+\sum_{j}\hbar\omega_{c}\hat{c}_{j}^{\dagger}\hat{c}_{j} \\ &+\sum_{j}\sum_{\nu}\hbar\left[\Omega_{\nu}(\mathbf{r}_{\parallel,j})\hat{c}_{j}+\Omega_{\nu}^{*}(\mathbf{r}_{\parallel,j})\hat{c}_{j}^{\dagger}\right]\left(\hat{a}_{\nu}^{\dagger}+\hat{a}_{\nu}\right)+ \\ &\sum_{j}\sum_{\nu,\nu'}\hbar^{2}\frac{\Omega_{\nu}(\mathbf{r}_{\parallel,j})\Omega_{\nu'}^{*}(\mathbf{r}_{\parallel,j})}{\omega_{c}}\left(\hat{a}_{\nu}+\hat{a}_{\nu}^{\dagger}\right)\left(\hat{a}_{\nu'}+\hat{a}_{\nu'}^{\dagger}\right),\end{aligned} \tag{6.1}$$

with $\hat{c}_j$ and $\hat{c}_j^{\dagger}$ the single-electron transition operator between the Landau levels with cyclotron transition frequency ω_c, as in Ref. [124].

In Eq. 6.1 the light-matter coupling parameter is

$$\Omega_{\nu}(\mathbf{r}_{\parallel,j})=\sqrt{\frac{\omega_{c}e^{2}}{2\epsilon_{0}\bar{\epsilon}m^{*}\omega_{\nu}\mathbf{V}_{\nu}}}f_{\nu}(\mathbf{r}_{\parallel,j}), \tag{6.2}$$

where ω_ν and $\mathbf{V}_\nu$ are, respectively, the νth photon mode frequency and mode volume; $f_\nu(\mathbf{r}_{\parallel,j})$, instead, represents the circularly polarized field function for the νth mode, calculated at the jth electron's in-plane position coordinate, such that the in-plane rotated vector potential has components

$$\hat{A}_-(\mathbf{r}_{\parallel,j}) = \sum_\nu \sqrt{\frac{\hbar}{2\epsilon_0\epsilon(z)\omega_\nu V_\nu}} f_\nu(\mathbf{r}_{\parallel,j}) \left(\hat{a}_\nu^\dagger + \hat{a}_\nu\right), \tag{6.3}$$

$$\hat{A}_+(\mathbf{r}_{\parallel,j}) = \sum_\nu \sqrt{\frac{\hbar}{2\epsilon_0\epsilon(z)\omega_\nu V_\nu}} f_\nu^*(\mathbf{r}_{\parallel,j}) \left(\hat{a}_\nu^\dagger + \hat{a}_\nu\right). \tag{6.4}$$

Details about the derivation of this Hamiltonian can be found in the Appendix C. It is worthwhile to mention that we consider the following approximations: first, electronic degrees of freedom in the dielectric background are neglected, however we consider their effect by means of an effective dielectric permittivity $\epsilon_0\bar{\epsilon}$; then we neglect the Coulomb electron-electron interactions, as Kohn's theorem states internal momentum-conserving potentials have no effect on the cyclotron motion of the center of mass. The bare photonic Hamiltonian in Eq. 6.1 is expressed as the sum of energy contributions of infinite photonic modes, which are orthogonal over the whole integration volume V, such that

$$\int_V \mathbf{f}_\nu^* \mathbf{f}_\mu = \mathbf{V}_\nu \delta_{\nu,\mu}, \tag{6.5}$$

with $\mathbf{f}_\nu$ three-dimensional mode function.

The key idea of this theory is to assume that the orthogonality of the bare photon modes is not maintained over the integration surface of the 2DEG. This would lead to an overlap between modes resulting in a mutual photon-photon interaction mediated by the coupling to the electrons. Each of the first n photonic mode functions in-plane $f_\nu(\mathbf{r}_\parallel)$ can be defined in arbitrary basis of n functions ϕ_ν orthogonal over the plane occupied by the 2DEG of area S, as

$$f_\nu(\mathbf{r}_{j,\parallel}) = \sum_{\mu\leq\nu} \alpha_{\nu,\mu}\phi_\mu(\mathbf{r}_{j,\parallel}), \tag{6.6}$$

obeying the orthonormalisation relations

$$\int_S \phi_\nu^*(\mathbf{r}_\parallel)\phi_\mu(\mathbf{r}_\parallel)\mathrm{d}\mathbf{r}_\parallel = \delta_{\mu,\nu}, \tag{6.7}$$

$$\sum_j^{N_{el}} \phi_\nu^*(\mathbf{r}_{j,\parallel})\phi_\mu(\mathbf{r}_{j,\parallel}) = N_{\mathrm{2DEG}}\,\delta_{\mu,\nu}, \tag{6.8}$$

with $N_{el} = N_{\mathrm{2DEG}}S$ number of electrons homogeneously distributed in each 2DEG. For sake of semplicity, when we write Eq.6.6 we choose an arbitrary basis for which all the coefficients $\alpha_{\nu,\mu}$ with $\nu \leq \mu$ are zero. The non-othonormality between the resonator modes over the quantum well plane can be represented by a normalisation matrix of elements

$$\mathcal{F}_{\nu,\mu} = \sum_j^N f_\nu^*(\mathbf{r}_{j,\parallel})f_\mu(\mathbf{r}_{j,\parallel}), \tag{6.9}$$

in general, different from zero. Once defined the matrix in Eq.6.9, we can introduce the overlap parameter

$$\eta_{\nu,\mu} = \frac{\mathcal{F}_{\nu\mu}}{\sqrt{\mathcal{F}_{\mu,\mu}\mathcal{F}_{\nu\nu}}}, \tag{6.10}$$

assuming values from 0 to 1. This is a crucial parameter quantifying the deviation from the orthogonality of each couple of photon modes. It is easy to see that a diagonal matrix F of elements $\mathcal{F}_{\nu,\mu}$ means no overlap ($\eta = 0$) between the photon modes. From the definitions in Eq.6.9 and Eq.6.6, we can write the relation

$$\mathcal{F}_{\nu,\mu} = N_{2DEG}\sum_{\gamma\leq\mu}\alpha_{\nu\gamma}^*\alpha_{\mu\gamma}. \tag{6.11}$$

By introducing a set of bosonic collective matter operators

$$\hat{b}_\mu = \frac{1}{\sqrt{N_{\mathrm{2DEG}}}}\sum_j^N \phi_\mu(\mathbf{r}_{j,\parallel})\hat{c}_j, \tag{6.12}$$

we can finally write the total Hamiltonian as

$$\hat{H} = \hat{H}_{\mathrm{EM}} + \hat{H}_{\mathrm{matter}} + \hat{H}_{\mathrm{int}} + \hat{H}_{\mathrm{dia}}, \tag{6.13}$$

with

$$\hat{H}_{\mathrm{EM}} = \sum_{\nu} \hbar\omega_{\nu}\hat{a}_{\nu}^{\dagger}\hat{a}_{\nu}, \tag{6.14}$$

$$\hat{H}_{\mathrm{matter}} = \sum_{\mu} \hbar\omega_{c}\hat{b}_{\mu}^{\dagger}\hat{b}_{\mu}, \tag{6.15}$$

$$\hat{H}_{\mathrm{int}} = \sum_{\nu}\sum_{\mu\leq\nu} \left[\left(g_{\nu,\mu}b_{\mu} + g_{\nu,\mu}^{*}b_{\mu}^{\dagger}\right)\left(\hat{a}_{\nu}^{\dagger} + \hat{a}_{\nu}\right)\right] \tag{6.16}$$

$$\hat{H}_{\mathrm{dia}} = \sum_{\nu,\nu'} h_{\nu,\nu'}\left(\hat{a}_{\nu}^{\dagger} + \hat{a}_{\nu}\right)\left(\hat{a}_{\nu'}^{\dagger} + \hat{a}_{\nu'}\right), \tag{6.17}$$

with coupling parameters

$$g_{\nu,\mu} = \sqrt{\frac{\hbar^{2}\omega_{c}N_{\mathrm{2DEG}}e^{2}}{2m^{*}\epsilon_{0}\bar{\epsilon}\omega_{\nu}L_{\nu,\mu}}}, \tag{6.18}$$

$$h_{\nu,\nu'} = \sum_{\gamma\leq\nu'} \frac{g_{\nu,\gamma}g_{\nu',\gamma}}{\omega_{c}}, \tag{6.19}$$

$$\tag{6.20}$$

with $L_{\nu,\mu} = V_{\nu}/|\alpha_{\nu,\mu}|^{2}$ effective length We observe that this Hamiltonian presents some important features. First, it is completely bosonic, which allows us to easily determine its eigenmodes by Hopfield method. Second, the light-matter interaction Hamiltonian displays cross-interaction terms between different photon and orthogonal matter modes, suggesting that the resonator modes *see each other* by means of the matter excitations.

Therefore, following the Hopfield approach we diagonalise the Hamiltonian by introducing the usual hybrid multi-mode polariton operators,

$$\hat{p}_{\mu} = \sum_{\nu} \left(x_{\nu,\mu}\hat{a}_{\nu} + w_{\nu,\mu}\hat{b}_{\nu} + y_{\nu,\mu}\hat{a}_{\nu}^{\dagger} + z_{\nu,\mu}\hat{b}_{\nu}^{\dagger}\right), \tag{6.21}$$

with $(x_{\nu,\mu}, w_{\nu,\mu}, y_{\nu,\mu}, z_{\nu,\mu})$ Hopfield coefficients, assumed to be real.

The dressed polariton frequencies ω_{μ}^{p} are the eigenvalues of the $4n \times 4n$ Hopfield matrix representing the Hamiltonian in Eq. 6.13.

6.3.1 Coupled Electric Field Distribution

The cross-term in the light-matter interaction of Eq. 6.13 finds its origin in the spatial overlap between different uncoupled resonator photon modes over

the plane of the 2DEG, and suggests the multi-mode hybrid nature of the resulting polariton modes.

Each coupled photon field, being the light component of a corresponding hybrid polariton mode, results a weighted linear combination of the bare resonator mode fields.

We now aim to calculate the coupled circularly polarized electric field components from the inverse Hopfield coefficients obtained by the diagonalization procedure.

By applying the inverse transformation for the the photon operator to Eq. 6.3

$$\left(\hat{a}_\nu + \hat{a}_\nu^\dagger\right) = \sum_\mu m_{\mu,\nu}\left(\hat{p}_\mu + \hat{p}_\mu^\dagger\right), \tag{6.22}$$

with $m_{\mu,\nu} = (x_{\mu,\nu} - y_{\mu,\nu})$, we find the coupled electric field components

$$\hat{E}_-(\mathbf{r}_{\parallel,j}) = \sum_{\nu\mu}\sqrt{\frac{\hbar\omega_\nu}{2\epsilon_0\bar{\epsilon}V_\nu}} f_\nu(\mathbf{r}_{\parallel,j}) m_{\mu,\nu}\left(\hat{p}_\mu^\dagger + \hat{p}_\mu\right), \tag{6.23}$$

$$\hat{E}_+(\mathbf{r}_{\parallel,j}) = \sum_{\nu\mu}\sqrt{\frac{\hbar\omega_\nu}{2\epsilon_0\bar{\epsilon}V_\nu}} f_\nu^*(\mathbf{r}_{\parallel,j}) m_{\mu,\nu}\left(\hat{p}_\mu^\dagger + \hat{p}_\mu\right). \tag{6.24}$$

The degree of mixing of the different uncoupled resonator modes into the new coupled ones is quantified by the Hopfield parameter $m_{\mu,\nu}$, which represents the contribution of νth photon mode in the μth polariton mode and certainly depends on the light-matter coupling strength.

6.4 Results

6.4.1 Numerical fit for hexagonal resonator with structured QWs

Given the simulated transmission spectra for the negative hexagonal THz metamaterial resonator coupled to a narrow QWs patch of Fig. 6.1, we use our multi-mode theory to fit simultaneously the resonances of both the spectra, by adjusting the photon mode effective lengths $L_{\nu,\mu}$. The resulting polariton modes are shown in Fig.6.4 superimposed on the resonance dips of the transmission spectra. The numerical fit gives also as output result

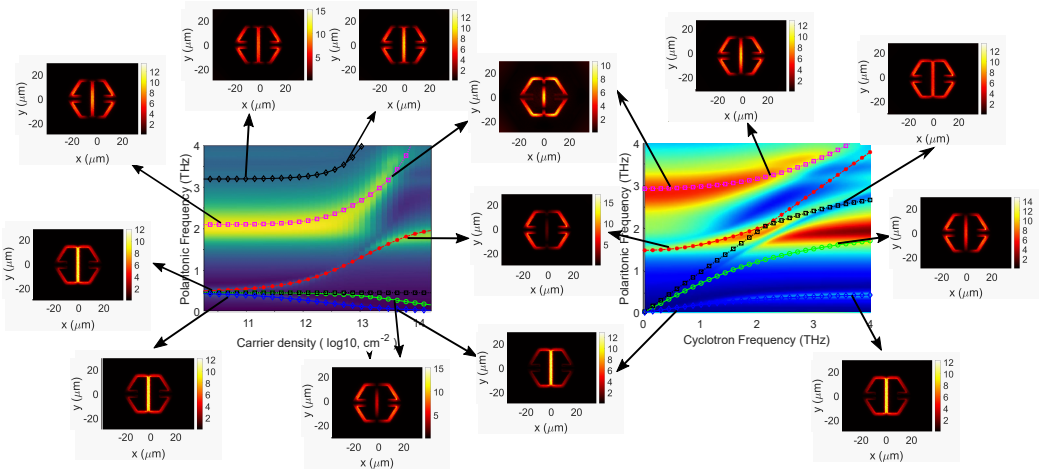

Figure 6.4: **Numerical fit of the simulated transmission data for THz hexagonal resonator coupled to cyclotron resonances of a 2DEG** Left: Transmission resonances fit as a function of the carrier density, and calculated normalised in-plane electric field $\sqrt{|E_x|^2 + |E_y|^2} * 10^{-4}$ m^{-2} for each coupled mode at doping values indicated by the arrows. Right: Same as left panel, but as function of the cyclotron frequency.

the overlap parameters $\eta_{\mu,\nu}$. Although in both the panels of Fig. 6.4, only four resonances are visible within the considered frequency range, this fit has been performed by including the first three photon modes of frequencies $\omega_1 = 0.48$ THz, $\omega_2 = 2.1$ THz and $\omega_3 = 3.2$ THz. We can see that the resulting polariton modes are in good agreement with the transmission resonances, and, most importantly, they maintain their same (at first sight) anomalous features: in the doping-sweep spectrum, the upper polariton modes, indicated by the dot-dashed red and dotted magenta curves, follow the same anti-crossing trend, due the mutual interaction between the first two photon modes, whose calculated overlap is $\eta_{2,1} \approx 0.7$. In the cyclotron-frequency-sweep, the inclusion of a third higher resonator mode allows to recover the s-shaped polariton mode (dashed red curve changing into the dotted black curve at the crossing point), although slightly red-shifted at the maximum cyclotron frequency. The s-shape derives from having a complete in-plane overlap between the third and the first photon modes, $\eta_{3,1} = 1$. The reason is explained as follows. From Eqs. 6.11 and 6.18, we can see that, in the extreme case of full overlap $\eta_{3,1} = 1$, the coupling parameter g_{33}, weighting the one-to-one interaction between the third photon mode and the third electronic mode (orthogonal and degenerate to the others), vanishes, leaving the cross interaction term dominant. Therefore, in this case, both the photon modes $\nu = 1, 3$ couple to a unique electronic excitation mode, leading to a double anti-crossing, as the one observed in [122].

Let us now observe the in-plane electric field maps for several coupled modes in Fig. 6.4. These are calculated from Eq. 6.23, as linear combination of all the photon modes components weighted by the respective Hopfield coefficients. We notice that, exactly as for the simulation, the electric fields look very similar to the original uncoupled ones where no multi-mode hybridization occurs, while they assume different shapes at the points of larger hybridization. For example, in the left panel, by following the first two upper polariton modes (red and magenta curves) as the carrier density increases, we observe significant modifications: at lower doping, both the electric field profiles maintain the same shape as the uncoupled fields of frequencies ω_1 and ω_2, pictured in Fig. 6.1(c), while, when the modes overcome the anticrossing point at higher doping, the electric field maps result a sum and a subtraction of them. Similar conclusions can be achieved for the coupled fields calculated in the cyclotron-frequency-sweep case.

6.4.2 Further Simulations and Numerical Fits

Given the success of our theory to explain the transmission resonances in the case of an hexagonal resonator, coupled to the cyclotron transitions of a narrow QWs patch, we investigated then the same metamaterial-QWs compound system in different design configurations. We here present the transmission data obtained by numerical simulations and corresponding numerical fits obtained through our multi-mode theory for USC.

The simulated unit cell is composed by a THz positive rectangular metamaterial resonator [121, 128], and a QWs stack designed either *unstructured*, that is with the same area as the whole unit cell, or *structured*, which means as a rectangular patch of size smaller than the average width of the resonator. As we will see, this difference in the design will allow to address different overlap parameters $\eta_{\nu,\mu}$ of the bare resonator modes over the area occupied by the 2DEG of the QWs. Fig. 6.5 shows the results obtained by simulating the rectangular resonator coupled to an unstructured stack of $N_{QW} = 3$ doped QWs with electronic density N_{2DEG} and distant $d_{qw} = 30$ nm from the resonator . The THz resonator is sketched in panel (c), where the purple region is occupied by the gold film and the red-shaded region indicates the QW surface, being, in this case, the whole unit cell plane. This type of resonator manifests two first resonances, one LC-type at $\omega_1 = 0.8$ THz and a second dipolar one at $\omega_2 = 1.6$ THz, whose electric field in-plane distribution is shown, respectively, in panels (d) and (e). Panels (a) and (b) display the simulated transmission spectra, respectively, as a function the cyclotron frequency ω_c at a fixed doping $N_{2DEG} = 1 \times 10^{12}$ cm^{-2}, and as a function of the doping at fixed $\omega_c = 0.8$ THz. The curves overlaid on the transmission spectra, represent the polariton modes calculated by numerical fit of the spectral resonances, in the same way as described for the hexagonal resonator case. The black dashed line indicates, instead, the bare cyclotron frequency. In this case, the resulting overlap parameter for the two photon modes is $\eta_{2,1} = 0.8$. Unlike in the hexagonal case, we here do not observe any evident signature of the multi-mode hybridization, because of the significantly lower coupling strength due to a limited electron density range.

Let us observe now what happens in the structured case, when a small square QWs patch is placed underneath the center of the rectangular resonator (Fig. 6.6(c)). Panels (a) and (b) of Fig. 6.6 show, exactly as Fig. 6.5, the simulated transmission spectra for the coupled system, and the cal-

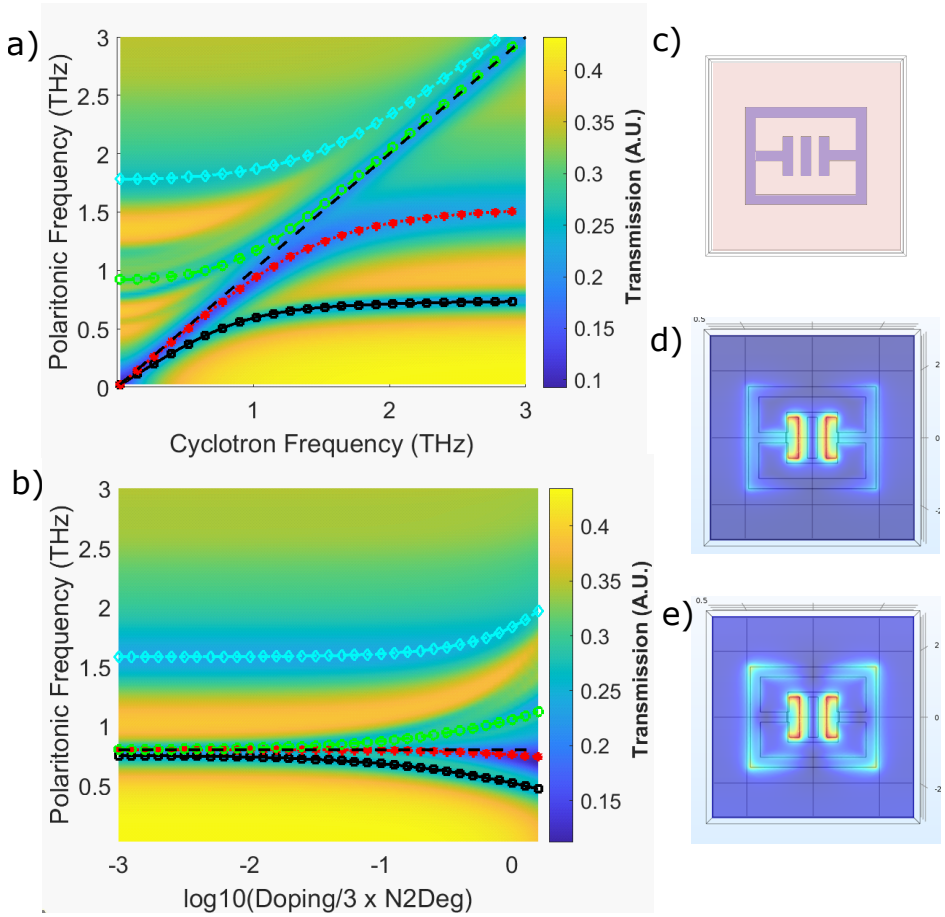

Figure 6.5: **Simulation and fit results of unstructured QWs coupled to a positive rectangular resonator.** Panels(a-b): Transmission spectrum and fit frequency modes as a function, respectively, of the cyclotron frequency and doping electron density. Panel(c): Sketch of the simulated unit cell, with gold deposition area in purple, and red-shaded QW plane. Panels(d-e): distribution maps of the electric field enhancement for the lowest two resonator frequency modes. These maps have been created by Prof. Lange's group

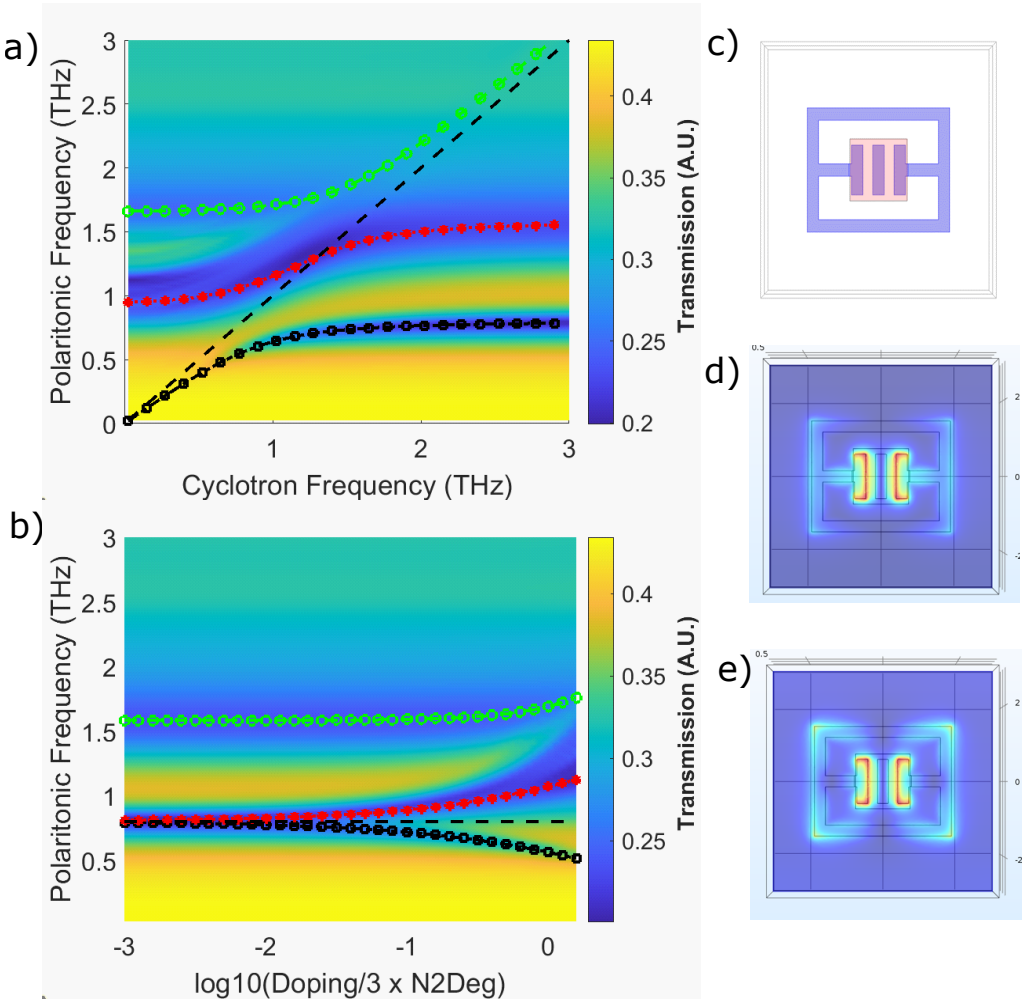

Figure 6.6: **Simulation and fit results of structured QWs patch coupled to a positive rectangular resonator.** Same features as Fig. 6.5.

culated polariton modes. In panel (a) a novel feature of the transmission spectrum is observable: one of the resonances manifests an *S-shape*, which, as seen for the hexagonal case (Fig. 6.1), can only be explained by assuming a full spatial overlap between the resonator modes over the QWs patch area S ($\eta_{2,1} = 1$). The numerical fit for these simulated data is thus a-priori performed by diagonalising the Hamiltonian in a three-modes subspace (two photon modes and one matter mode), obtaining the three polariton modes showed as black, red and green curves in Figs. 6.6 (a) and (b).

Let us discuss now the physical reason for which the overlap parameters in these last two cases are significantly different. Although the resonator design is the same for both the configurations, an important role here is played by the area and the position of the QWs stack. In the unstructured case, the area S occupied by the electrons is the whole unit cell surface, where, on average, the photon modes have a significantly inhomogeneous electric field distribution . On the contrary, in the structured case, both the electric fields are highly confined in the small area occupied by the QWs, although they may potentially have opposite sign. We can naively say that, since the interaction between the resonator modes on the plane is mediated by the electrons with high density N_{2DEG}, the more electrons see both the resonator modes' electric fields highly confined, the more the latters interact between each other. This can also be seen from Eq. 6.9 and from the definition of $\eta_{\nu,\mu}$. The normalised cross integral between the modes $\nu = 2$ and $\mu = 1$ is maximum in the S area over which the mode functions $f_1(\mathbf{r}_{j,\parallel})$ and $f_2(\mathbf{r}_{j,\parallel})$ agree in sign and are mostly confined.

6.4.3 Conclusions

In this chapter, it is shown that non-perturbative light-matter coupling regimes can affect resonator photon fields as well as the matter's properties. In the specific case of a THz metamerial resonator coupled to the cyclotron transitions of a 2DEG, we theoretically demonstrate that, at accessible high values of the normalised coupling, the strongly two-dimensional geometry of the system can lead to a multi-photon-mode hybridization, significantly changing the electromagnetic field profile of the coupled modes. Our developed theory succeeds reproducing not only the spectral resonances, but also some of the electric field in-plane maps obtained by Comsol simulations.

Prof. Lange's group is currently working on the experimental measurements. Preliminary experimental data are already able to confirm what pre-

dicted by simulations and numerical calculations. These promising results encourage us to investigate even more different configurations, aiming to the optimize of the phenomenon. We aim to explore more deeply the nature and the implications of the multi-mode hybridization, in order to address new quantum technological applications based on the possibility of controllably tuning high confined electromagnetic fields .

Chapter 7

Overall Conclusions

Cavity quantum electrodynamics investigates the interaction of matter with single photons confined in a cavity. The most intriguing physical effects are observable when we enter non-perturbative regimes, reached in a broad range of systems, where values of the normalised light-matter coupling comparable to the unity not only cause a shift of the optical resonances, but also lead to significant modification of the properties of the subsystems involved.

My research project had the general aim of uncover significant applicable phenomena of cavity QED physics, that may lead to important advances in quantum technologies.

This dissertation began introducing some of the main standard theoretical models for the description of quantum light-matter phenomena, providing the reader with the key concepts for the understanding of the following. In the first chapter, I presented a novel theoretical approach to describe the non-linear effects coming into play when we detail the internal dipole-dipole interactions within a 2LSs ensamble, coherently coupled to the same cavity mode. Assuming that the dynamics of this kind of systems can be described by a Dicke-Ising Hamiltonian, I developed a theoretical general method which, by exploiting the higher order terms of the Holstein-Primakoff transformations, allows to analytically calculate the polariton spectrum of the system in term of bosonic excitations for large values of the dipole-dipole interaction. The interplay between the dipole-dipole and the light-matter coupling strengths is also investigated, showing that the saturation effects due to the former have a significant impact on the latter, as the interactions become comparable with the bare transition frequency.

I also studied the effects of non-perturbative QED regimes on internal

matter degrees of freedom. In particular, by taking into account the specific case of rotational degrees of freedom of an ensamble of a large number of two-dimensional dipoles coupled to a cavity mode, I demonstrate that an increasing excitation rate (obtained by optical pump) leads to an ordering of the collective orientational configuration of the dipoles. Most importantly, it is also demonstrated that this phenomenon is driven by the collective coupling strength, not by the single-molecule one, and as such potentially observable at room temperature. It is also shown that as the excitation rate approaches the unity, saturation effects should be considered without significantly changing the overall orientational ordering trend. The physics described by this work has a quite general validity. Since the collective light-matter interaction influences the degrees of freedom because of its own dependence upon them, we may expect that the same phenomenon can be observable on other systems, such as, e.g. an array of flux-qubits strongly coupled to LC circuit resonators, where it would be likely possible to measure modifications of the magnetic flux .

Driven by the ever growing interest about the possible applications of cavity QED phenomena in various research fields, from chemistry and biology to solid-state technology, I investigated the effects of non-perturbative regimes on ionization processes. Although the intrinsic irreversible nature of the ionizing transitions, by studying the well-known case of a cavity-embedded doped quantum well heterostructure, my calculations predicted that it is possible not only to achieve SC regime between a discrete cavity mode and ionizing electronic transitions, but also to create a novel bound exciton state, bound not by Coulomb interaction but via photon exchange with the cavity field. Most importanlty, this prediction has also been experimentally demonstrated by reflectivity measurements, carried out by Prof. Raffaele Colombelli and his group in Paris. Since the preliminary phase of the experimental project, I have been involved in the choice of the optimal design, supported by several of my numerical simulations, and, afterwords, I have been in charge of the experimental data analysis. The resultant manuscript is currently under peer-review.

The precious collaboration with another oversea experimental group, leaded by Prof. C. Lange of University of Regensburg (Germany), gave me the opportunity and the hint, in the last year, to explore the possible modifications of the resonator photon field profile in Landau polariton systems at very high normalised coupling strengths. I developed a general multi-photon-mode Hopfield theory, able to numerically determine both the polariton spectrum

and the coupled electric fields. By assuming a non-negligible in-plane interaction between different resonator modes, we demonstrate this leads to a multi-mode hybridization of the polaritons, whose photon components manifest hybrid electric field distributions. This phenomenon is also meant to be experimentally proved by Prof. Lange's group, who gave the honour to be guest and partecipant to fews of the preliminary experimental sessions. In conclusion, my research project is clearly only a drop in the sea of possible investigations of non-perturbative regime induced phenomena, but it can be an encouragement to the research community for the deeper study of technological game-changer CQED applications.

Appendix A

Diagonalisation of Dicke-Ising Hamiltonian

A.1 Diagonalisation of the Hamiltonian for the transverse field Ising model.

A.1.1 Exact diagonalisation

The Hamiltonian in Eq.3.1 can be diagonalised exactly by performing the Jordan-Wigner transformation

$$\begin{aligned} \hat{\sigma}_n^- &= \prod_{j<n}(1-2\,\hat{c}_j^\dagger\hat{c}_j)\hat{c}_n, \\ \hat{\sigma}_n^+ &= \prod_{j<n}(1-2\,\hat{c}_j^\dagger\hat{c}_j)\hat{c}_n^\dagger, \end{aligned} \tag{A.1}$$

where $\hat{c}_n^\dagger$ and $\hat{c}_n$ are fermionic creation and annihilation operators satisfying the anticommutation rules:

$$\left\{\hat{c}_n, \hat{c}_m^\dagger\right\} = \delta_{nm}\ , \tag{A.2}$$

$$\left\{\hat{c}_n^\dagger, \hat{c}_m^\dagger\right\} = \{\hat{c}_n, \hat{c}_m\} = 0. \tag{A.3}$$

The Hamiltonian in Eq.3.1 then takes the form

$$\begin{aligned}\hat{H}_{\rm F} &= \omega_0 \sum_{n=1}^{N} \hat{c}_n^\dagger \hat{c}_n + J \sum_{n=1}^{N-1} (\hat{c}_n^\dagger \hat{c}_{n+1} - \hat{c}_n \hat{c}_{n+1}^\dagger) \\ &\quad + J \sum_{n=1}^{N-1} (\hat{c}_n^\dagger \hat{c}_{n+1}^\dagger - \hat{c}_n \hat{c}_{n+1}). \end{aligned} \tag{A.4}$$

We can now pass in momentum space defining the operators $\hat{c}_k$ and $\hat{c}_k^\dagger$ by the relations

$$\begin{aligned}\hat{c}_n &= \frac{1}{\sqrt{N}} e^{-i\pi/4} \sum_k e^{ink}\, \hat{c}_k, \\ \hat{c}_n^\dagger &= \frac{1}{\sqrt{N}} e^{i\pi/4} \sum_k e^{-ink}\, \hat{c}_k^\dagger, \end{aligned} \tag{A.5}$$

where the phase factor $\exp(-i\pi/4)$ is introduced in order to guarantee real coefficients. The resulting Hamiltonian is then put in the diagonal form in Eq. 3.2 in terms of the fermionic operators

$$\begin{aligned}\hat{d}_{F,k} &= \alpha_{F,k}\, \hat{c}_k + \beta_{F,k}\, \hat{c}_{-k}^\dagger, \\ \hat{d}_{F,k}^\dagger &= \beta_{F,k}\, \hat{c}_{-k} + \alpha_{F,k}\, \hat{c}_k^\dagger, \end{aligned} \tag{A.6}$$

with

$$\begin{aligned}\alpha_{F,k} &= \frac{\omega_0 + 2J\cos k + E_{F,k}}{\sqrt{\left(\omega_0 + 2J\cos k + E_{F,k}\right)^2 + 4J^2 \sin^2 k}}, \\ \beta_{F,k} &= -\frac{2J \sin k}{\sqrt{\left(\omega_0 + 2J\cos k + E_{F,k}\right)^2 + 4J^2 \sin^2 k}}. \end{aligned} \tag{A.7}$$

A.1.2 The Bose approximation

The Hamiltonian in Eq. 3.1 can be mapped into a fully bosonic one through the Holstein-Primakoff transformation (see Eq. 3.6). If one retains only the

first term of the expansions the Hamiltonian becomes:

$$\begin{aligned}\hat{H}_{\rm B} &= \omega_0 \sum_{n=1}^{N} \hat{b}_n^\dagger \hat{b}_n + J \sum_{n=1}^{N-1} (\hat{b}_n^\dagger \hat{b}_{n+1} + \hat{b}_n \hat{b}_{n+1}^\dagger) \\ &\quad + J \sum_{n=1}^{N-1} (\hat{b}_n^\dagger \hat{b}_{n+1}^\dagger + \hat{b}_n \hat{b}_{n+1}). \end{aligned} \tag{A.8}$$

Following a procedure similar to the one used in the exact diagonalisation of the fermionic case, one can pass in momentum space by the relations

$$\begin{aligned}\hat{b}_n &= \frac{1}{\sqrt{N}} \sum_k e^{ink}\, \hat{b}_k, \\ \hat{b}_n^\dagger &= \frac{1}{\sqrt{N}} \sum_k e^{-ink}\, \hat{b}_k^\dagger. \end{aligned} \tag{A.9}$$

After substituting Eq.A.9 in Eq.Eq. A.8, the Hamiltonian can be put in the diagonal form in Eq.3.9 by the Bogoliubov transformation

$$\begin{aligned}\hat{d}_{B,k} &= \alpha_{B,k}\, \hat{b}_k + \beta_{B,k}\, \hat{b}_{-k}^\dagger, \\ \hat{d}_{B,k}^\dagger &= \beta_{B,k}\, \hat{b}_{-k} + \alpha_{B,k}\, \hat{b}_k^\dagger, \end{aligned} \tag{A.10}$$

with

$$\begin{aligned}\alpha_{B,k} &= \frac{\omega_0 + 2J\cos k + E_{B,k}}{\sqrt{\left(\omega_0 + 2J\cos k + E_{B,k}\right)^2 - 4J^2 \cos^2 k}}, \\ \beta_{B,k} &= \frac{2J\cos k}{\sqrt{\left(\omega_0 + 2J\cos k + E_{B,k}\right)^2 - 4J^2 \cos^2 k}}. \end{aligned} \tag{A.11}$$

Introducing the ground state $|G\rangle$, defined by the usual relations $\hat{d}_{B,k}\,|G\rangle = 0$ and inverting Eq.A.10 we can then calculate the ground state population of virtual excitations

$$\begin{aligned}\mathcal{N} &\equiv \langle G|\, \hat{b}_n^\dagger \hat{b}_n\, |G\rangle = \frac{1}{N} \sum_k \langle G|\, \hat{b}_k^\dagger \hat{b}_k\, |G\rangle \\ &= \frac{1}{N} \sum_k |\beta_{B,k}|^2 = \frac{\eta^2}{2} + O(\eta^3). \end{aligned} \tag{A.12}$$

A.2 Diagonalisation of the bosonic matter Hamiltonian at the first-order Holstein-Primakoff approximation

After inserting Eq.3.16 into Eq.3.14, neglecting the nonlinear normally-ordered terms which vanish in the zero- and one-particle subspace, one obtains the Hamiltonian in Eq.3.17, where the linear coefficients are

$$\begin{aligned}
\mathcal{A}_k &= \omega_0(\alpha^2_{\tilde{B},k} + \beta^2_{\tilde{B},k}) + 2(\alpha_{\tilde{B},k} + \beta_{\tilde{B},k})^2 J\cos k, \\
\mathcal{B}_k &= \omega_0\,\alpha_{\tilde{B},k}\,\beta_{\tilde{B},k} + 2(\alpha_{\tilde{B},k} + \beta_{\tilde{B},k})^2 J\cos k, \\
\mathcal{C}_k &= \omega_0\,\beta^2_{\tilde{B},k} + J\cos k(2\alpha_{\tilde{B},k}\beta_{\tilde{B},k} + \beta^2_{\tilde{B},k}),
\end{aligned} \tag{A.13}$$

and the nonlinear ones are

$$\begin{aligned}
f(k,k') &= 2\left(\alpha_{\tilde{B},k}\beta_{\tilde{B},k'} + \alpha_{\tilde{B},k'}\beta_{\tilde{B},k}\right)\left(\alpha_{\tilde{B},k} + \beta_{\tilde{B},k}\right)\left(\alpha_{\tilde{B},k'} + \beta_{\tilde{B},k'}\right)(\cos k + \cos k') \\
&\quad +2\,\alpha_{\tilde{B},k}\beta_{\tilde{B},k}\cos k'\left(\alpha_{\tilde{B},k'} + \beta_{\tilde{B},k'}\right)^2 + 2\,\beta^2_{\tilde{B},k'}\cos k\left(\alpha_{\tilde{B},k} + \beta_{\tilde{B},k}\right)^2, \\
g(k,k') &= 4\,\beta_{\tilde{B},k'}\left(\alpha_{\tilde{B},k} + \beta_{\tilde{B},k}\right)^2\left(\alpha_{\tilde{B},k'} + \beta_{\tilde{B},k'}\right)(\cos k + \cos k') \\
&\quad +2\,\alpha^2_{\tilde{B},k}\cos k'\left(\alpha_{\tilde{B},k'} + \beta_{\tilde{B},k'}\right)^2 + 4\,\beta^2_{\tilde{B},k'}\cos k\left(\alpha_{\tilde{B},k} + \beta_{\tilde{B},k}\right)^2 \\
&\quad +2\,\beta^2_{\tilde{B},k}\cos k'\left(\alpha_{\tilde{B},k'} + \beta_{\tilde{B},k'}\right)^2, \\
h(k,k') &= 2\,\beta_{\tilde{B},k}\beta_{\tilde{B},k'}(\cos k + \cos k')\left(\alpha_{\tilde{B},k} + \beta_{\tilde{B},k}\right)\left(\alpha_{\tilde{B},k'} + \beta_{\tilde{B},k'}\right) \qquad \text{(A.14)} \\
&\quad +2\,\beta^2_{\tilde{B},k}\cos k'\left(\alpha_{\tilde{B},k'} + \beta_{\tilde{B},k'}\right)^2. \qquad \text{(A.15)}
\end{aligned}$$

The coefficients $\alpha_{\tilde{B},k}$ and $\beta_{\tilde{B},k}$ can then be determined perturbatively to the second order through Eq.3.18 by writing

$$\begin{aligned}
\beta_{\tilde{B},k} &\approx \beta^{(0)}_{\tilde{B},k} + \beta^{(1)}_{\tilde{B},k}\,\eta + \beta^{(2)}_{\tilde{B},k}\,\eta^2, \\
\alpha_{\tilde{B},k} &\approx \sqrt{1+\beta^2_{\tilde{B},k}} \approx 1 + \frac{\beta^{(0)2}_{\tilde{B},k}}{2} + \beta^{(0)}_{\tilde{B},k}\beta^{(1)}_{\tilde{B},k}\eta + \frac{\left(\beta^{(1)2}_{\tilde{B},k} + 2\beta^{(0)}_{\tilde{B},k}\beta^{(2)}_{\tilde{B},k}\right)}{2}\eta^2,
\end{aligned} \tag{A.16}$$

and solving analytically the resulting algebraic system.

A.3 Diagonalisation of the Bosonic light-matter Hamiltonian

The bosonic light-matter Hamiltonian in Eq.3.26 can be diagonalised using an approach originally due to Hopfield [51]. For the sake of clarity in this Appendix we will drop the O subscript from the bosonic operators and the effective coupling as the outlined procedure is valid for arbitrary bosonic operators.

In the basis $\hat{\mathbf{v}}_k = \left[\hat{a}_k \ \hat{d}_k \ \hat{a}^\dagger_{-k} \ \hat{d}^\dagger_{-k}\right]^T$, the Hopfield matrix for the Hamiltonian of Eq.3.26 is

$$\mathcal{M}_k = \begin{bmatrix} \tilde{\omega}_k & -\Lambda_k & 0 & \Lambda_k \\ -\Lambda_k & E_k & \Lambda_k & 0 \\ 0 & -\Lambda_k & -\tilde{\omega}_k & \Lambda_k \\ -\Lambda_k & 0 & \Lambda_k & -E_k \end{bmatrix} \tag{A.17}$$

so that

$$\hat{H} = \frac{1}{2}\hat{\mathbf{v}}^\dagger_k \mu \mathcal{M}_k \hat{\mathbf{v}}_k, \tag{A.18}$$

with μ =diag$[1, 1, -1, -1]$ the bosonic metric matrix.
The eigenvalues of $\mathcal{M}_k$ are

$$E^\pm_k = \frac{1}{\sqrt{2}}\left[\tilde{\omega}^2_k + E^2_k \pm \Delta_k\right]^{\frac{1}{2}}, \tag{A.19}$$

with $\Delta_k = \left[(\tilde{\omega}^2_k - E^2_k)^2 + 16\Lambda^2_k\, \tilde{\omega}_k\, E_k\right]^{\frac{1}{2}}$.

If we define the vector $\hat{\mathbf{p}}_k = \left[\hat{p}_{-,k} \ \ \hat{p}_{+,k} \ \ \hat{p}^\dagger_{-,-k} \ \ \hat{p}^\dagger_{+,-k}\right]^T$, the Hamiltonian can then be put in the diagonal form

$$H = \frac{1}{2}\hat{\mathbf{p}}^\dagger_k \mu \mathcal{D}_k \hat{\mathbf{p}}_k, \tag{A.20}$$

where $\mathcal{D}_k = \text{diag}[E^-_k, E^+_k, -E^-_k, -E^+_k]$.
The vectors $\hat{\mathbf{p}}_k$ and $\hat{\mathbf{v}}_k$ are related by the relation $\hat{\mathbf{p}}_k = U^\dagger \mu\, \hat{\mathbf{v}}_k$, where U is the unitary transformation matrix. The extended expressions for the lower- and upper-polariton operators $\hat{p}_{-,k}$ and $\hat{p}_{+,k}$ are then:

$$\begin{aligned} \hat{p}_{-,k} &= x_-\hat{a}_k + y_-\hat{d}_k + w_-\hat{a}^\dagger_{-k} + z_-\hat{d}^\dagger_{-k}, \\ \hat{p}_{+,k} &= x_+\hat{a}_k + y_+\hat{d}_k + w_+\hat{a}^\dagger_{-k} + z_+\hat{d}^\dagger_{-k}, \end{aligned} \tag{A.21}$$

where the coefficients of the transformations, which can always be chosen real, are the components of the eigenvectors:

$$\begin{pmatrix} x_\pm \\ y_\pm \\ w_\pm \\ z_\pm \end{pmatrix} = \left\{ 4E_k^\pm \tilde{\omega}_k \left[1 + \frac{4\Lambda_k^2 E_k \, \tilde{\omega}_k}{(E_k^{\pm 2} - E_k^2)^2} \right] \right\}^{-\frac{1}{2}} \begin{pmatrix} \tilde{\omega}_k + E_k^\pm \\ \frac{2\Lambda_k \tilde{\omega}_k}{E_k^\pm - E_k} \\ -(\tilde{\omega}_k - E_k^\pm) \\ \frac{2\Lambda_k \tilde{\omega}_k}{E_k^\pm + E_k}, \end{pmatrix} . \quad \text{(A.22)}$$

where normalisation factor is found by imposing that the operators $\hat{p}_{-,k}$ and $\hat{p}_{+,k}$ to obey bosonic commutation rules $\left[\hat{p}_{\pm,k}, \hat{p}^\dagger_{\pm,k'}\right] = \delta_{k,k'}$. The inverse relation $\hat{\mathbf{v}}_k = U\mu\,\hat{\mathbf{p}}_k$ allows us to express the operators $\hat{a}_k$ and $\hat{d}_k$ as a linear combinations of $\hat{p}_{-,k}$ and $\hat{p}_{+,k}$ as

$$\begin{aligned} \hat{a}_k &= x_- \hat{p}_{-,k} + x_+ \hat{p}_{+,k} - w_- \hat{p}^\dagger_{-,-k} - w_+ \hat{p}^\dagger_{+,-k}, \\ \hat{d}_k &= y_- \hat{p}_{-,k} + y_+ \hat{p}_{+,k} - z_- \hat{p}^\dagger_{-,-k} - z_+ \hat{p}^\dagger_{+,-k}. \end{aligned} \quad \text{(A.23)}$$

A.4 Diagonalization of the light-matter Hamiltonian at the first order Holstein-Primakoff approximation

Analogously to what has been done for the isolated Ising chain, we aim to diagonalise the full Dicke-Ising Hamiltonian in the first order Holstein-Primakoff approximation, obtained by plugging Eq.3.13 in Eq.3.21, including the nonlinear part of the light-matter Hamiltonian in Eq.3.35. The multimode equivalent of Eq.3.16 reads

$$\begin{aligned} \hat{a}_k &= x_{\check{B},-}\, \hat{p}_{-,k} + x_{\check{B},+}\, \hat{p}_{+,k} - w_{\check{B},-}\, \hat{p}^\dagger_{-,-k} - w_{\tilde{B},+}\, \hat{p}^\dagger_{+,-k}, \\ \hat{b}_k &= y_{\check{B},-}\, \hat{p}_{-,k} + y_{\check{B},+}\, \hat{p}_{+,k} - z_{\check{B},-}\, \hat{p}^\dagger_{-,-k} - z_{\check{B},+}\, \hat{p}^\dagger_{+,-k}, \end{aligned} \quad \text{(A.24)}$$

where the Hopfield coefficients will be determined by diagonalising the quadratic part of the normally-ordered Hamiltonian expressed in terms of the polaritonic operators. By requiring that all the non-diagonal terms must go to zero, we then recover a nonlinear system of equations for the Hopfield coefficients. In order to simplify the analytic calculation, we first expand the

coefficients $x_{\check{B},\pm}$,$y_{\check{B},\pm}$, $z_{\check{B},\pm}$, and $w_{\check{B},\pm}$ respect to the normalised couplings η and ν up to the second order

$$\begin{aligned}
x_{\check{B},\pm} \approx &\quad x^{(0)}_{\check{B},\pm} + x^{(1,\eta)}_{\check{B},\pm}\eta + x^{(1,\nu)}_{\check{B},\pm}\nu + x^{(2,\eta)}_{\check{B},\pm}\eta^2 + x^{(2,\eta\nu)}_{\check{B},\pm}\eta\nu + x^{(2,\nu)}_{\check{B},\pm}\nu^2, \\
y_{\check{B},\pm} \approx &\quad y^{(0)}_{\check{B},\pm} + y^{(1,\eta)}_{\check{B},\pm}\eta + y^{(1,\nu)}_{\check{B},\pm}\nu + y^{(2,\eta)}_{\check{B},\pm}\eta^2 + y^{(2,\eta\nu)}_{\check{B},\pm}\eta\nu + y^{(2,\nu)}_{\check{B},\pm}\nu^2, \\
z_{\check{B},\pm} \approx &\quad z^{(0)}_{\check{B},\pm} + z^{(1,\eta)}_{\check{B},\pm}\eta + z^{(1,\nu)}_{\check{B},\pm}\nu + z^{(2,\eta)}_{\check{B},\pm}\eta^2 + z^{(2,\eta\nu)}_{\check{B},\pm}\eta\nu + z^{(2,\nu)}_{\check{B},\pm}\nu^2, \\
w_{\check{B},\pm} \approx &\quad w^{(0)}_{\check{B},\pm} + w^{(1,\eta)}_{\check{B},\pm}\eta + w^{(1,\nu)}_{\check{B},\pm}\nu + z^{(2,\eta)}_{\check{B},\pm}\eta^2 + w^{(2,\eta\nu)}_{\check{B},\pm}\eta\nu + w^{(2,\nu)}_{\check{B},\pm}\nu^2. \qquad \text{(A.25)}
\end{aligned}$$

By solving the system of equations, we obtain the expressions of the coefficients:

$$\begin{aligned}
x_{\check{B},-} &\approx 1 - \frac{2\omega_0^4\nu^2}{(\omega_0^2-\omega_k^2)^2}, \\
x_{\check{B},+} &\approx \frac{\omega_0^{3/2}\nu}{\sqrt{\omega_k}(\omega_k-\omega_0)} + \frac{\cos k(\omega_0+\omega_k)\omega_0^{3/2}\eta\nu}{\sqrt{\omega_k}(\omega_k-\omega_0)^2}, \\
y_{\check{B},-} &\approx \frac{\omega_0^{3/2}\nu}{\sqrt{\omega_k}(\omega_0-\omega_k)} - \frac{4\cos k\sqrt{\omega_k}\omega_0^{5/2}\eta\nu}{(\omega_k-\omega_0)^2(\omega_k+\omega_0)}, \\
y_{\check{B},+} &\approx 1 + \frac{1}{2}\eta^2\cos k^2 - \frac{2\omega_0^4\nu^2}{(\omega_k-\omega_0)^2(\omega_k+\omega_0)^2}, \\
z_{\check{B},-} &\approx \frac{\omega_0^{3/2}\nu}{\sqrt{\omega_k}(\omega_k+\omega_0)} - \frac{4\cos k\sqrt{\omega_k}\omega_0^{5/2}\eta\nu}{(\omega_k^2-\omega_0^2)(\omega_k+\omega_0)}, \\
z_{\check{B},+} &\approx \eta\cos k - \eta^2\left(2\cos k^2 - \frac{1}{2}\right) - \nu^2\left(\frac{\omega_0^2}{\omega_0^2-\omega_k^2} + \sum_{k'}\frac{1}{N}\frac{\omega_0^2}{2(\omega_{k'}\omega_0+\omega_{k'}^2)}\right), \\
w_{\check{B},-} &\approx -\frac{\omega_0^4\nu^2}{\omega_k^2(\omega_k^2-\omega_0^2)}, \\
w_{\check{B},+} &\approx \frac{\omega_0^{3/2}\nu}{\sqrt{\omega_k}(\omega_k+\omega_0)} + \frac{\cos k(\omega_k-\omega_0)^3\eta\nu}{\sqrt{\omega_k\omega_0}(\omega_k^2-\omega_0^2)}. \qquad \text{(A.26)}
\end{aligned}$$

Appendix B

Theory of bound-to-continuum strong coupling

B.1 Theory of bound-to-continuum strong coupling

B.1.1 Calculation of the bare electronic wavefunctions

Following the approach described in Ref. [129] we determine the electronic envelope functions $\phi_n(z)$ and their subband-edge energies $\hbar\omega^c_{n\mathbf{0}}$ numerically solving the eigenequation

$$\left[-\frac{\hbar^2}{2}\frac{\partial}{\partial z}\frac{1}{m^*(z)}\frac{\partial}{\partial z}+V(z)\right]\phi_n(z) \;=\; \hbar\omega^c_{n\mathbf{0}}\phi_n(z), \tag{B.1}$$

where the potential due to band offset $V(z)$ and the effective mass $m^*(z)$ are piecewise constant. Solution of Eq. B.1 can then be numerically calculated enforcing the continuity of $\phi_n(z)$ and $\frac{1}{m^*(z)}\frac{\partial}{\partial z}\phi_n(z)$ at the interfaces [14].

Appendix C

Theory of Landau Polaritons

C.1 Light matter Hamiltonian in Coulomb gauge

Let us consider the Hamiltonian describing a two-dimensional electron gas (2DEG) of N electrons of charge $-e$ and effective mass m^* interacting with a resonator photonic field in the Coulomb Gauge

$$\hat{H} = \int d\mathbf{r} \left[\frac{\epsilon_0 \hat{\mathbf{E}}_\perp(\mathbf{r})^2}{2} + \frac{\hat{\mathbf{B}}(\mathbf{r})^2}{2\mu_0} \right] + \sum_{j=1}^{N} \frac{\left(\hat{\mathbf{p}}_j + e\hat{\mathbf{A}}(\mathbf{r}_j) \right)^2}{2m^*} + V(\mathbf{r}), \qquad \text{(C.1)}$$

expressed in terms of the electric and magnetic field vectors $\hat{\mathbf{E}}(\mathbf{r})$ and $\hat{\mathbf{B}}(\mathbf{r})$, the potential vector $\hat{\mathbf{A}}(\mathbf{r})$ and the Coulomb potential $V(\mathbf{r})$. The first term represents the energy of the transverse fields $\hat{\mathbf{B}}(\mathbf{r})$ and $\hat{\mathbf{E}}_\perp(\mathbf{r}) = -\frac{\hat{\mathbf{\Pi}}(\mathbf{r})}{\epsilon_0}$,where $\hat{\mathbf{\Pi}}(\mathbf{r})$ is the conjugate momentum of the vector potential, which satisfies the commutation relation $\left[\hat{\mathbf{A}}(\mathbf{r}), \hat{\mathbf{\Pi}}(\mathbf{r}') \right] = \imath\hbar\delta^T(\mathbf{r} - \mathbf{r}')$. We now consider the following approximations: first, we neglect the degrees of freedom of charges in the dielectric background, although considering their effect by substituing the vacuum dielectric permettivity ϵ_0 with the one of medium $\epsilon_0\epsilon(\mathbf{r})$, taken isotropic and non dispersive; then, thanks to Kohn's theorem, we can neglect the Coulomb electron-electron interactions, since it has been demonstrated that they have no effect on the cyclotron resonance we are investigating.

If, for sake of semplicity, we consider a z-dependent background dielectric

permettivity, for the electromagnetic field Hamiltonian we obtain

$$\hat{H}_{\mathrm{EM}} = \int d\mathbf{r} \left[\frac{\epsilon_0 \epsilon(z) \hat{\mathbf{E}}_{\perp}(\mathbf{r})^2}{2} + \frac{\hat{\mathbf{B}}(\mathbf{r})^2}{2\mu_0} \right]. \tag{C.2}$$

By expressing the fields in terms of the potential vector $\hat{\mathbf{A}}(\mathbf{r})$, such that

$$\hat{\mathbf{B}}(\mathbf{r}) = \nabla \times \hat{\mathbf{A}}(\mathbf{r}) \tag{C.3}$$

$$\hat{\mathbf{E}}_{\perp}(\mathbf{r}) = -\frac{\partial}{\partial t} \hat{\mathbf{A}}(\mathbf{r}), \tag{C.4}$$

we can express the electromagnetic Hamiltonian as

$$\hat{H}_{\mathrm{EM}} = \int d\mathbf{r} \left[\frac{\epsilon_0 \epsilon(z)}{2} \left(\frac{\partial}{\partial t} \hat{\mathbf{A}}(\mathbf{r}) \right)^2 + \frac{\left(\nabla \times \hat{\mathbf{A}}(\mathbf{r}) \right)^2}{2\mu_0} \right]. \tag{C.5}$$

By quantizing the electromagnetic field we obtain the vector potential operator

$$\hat{\mathbf{A}}(\mathbf{r}) = \sum_{\nu} \mathcal{C}_{\nu} \left[\mathbf{f}_{\nu}^{*}(\mathbf{r}) \hat{a}_{\nu}^{\dagger} + \mathbf{f}_{\nu}(\mathbf{r}) \hat{a}_{\nu} \right], \tag{C.6}$$

where the index ν counts the electromagnetic modes, $\mathbf{f}_{\nu}(\mathbf{r})$ is the spacial mode shape function vector and $\mathcal{C}_{\nu}$ is a normalization factor

$$\mathcal{C}_{\nu} = (\hbar / 2\epsilon_0 \epsilon(z) \omega_{\nu} V_{\nu})^{\frac{1}{2}} \tag{C.7}$$

with the mode effective volume

$$V_{\nu} = \int d\mathbf{r} |\mathbf{f}_{\nu}(\mathbf{r})|^{\mathbf{2}}, \tag{C.8}$$

such that, calculated the fields from the vector potential C.6 and plugged in C.2, this is equal to

$$\hat{H}_{\mathrm{EM}} = \sum_{\nu} \hbar \omega_{\nu} \left(\hat{a}_{\nu}^{\dagger} \hat{a}_{\nu} + \frac{1}{2} \right). \tag{C.9}$$

Let us focus now on the light matter interaction. We consider a number N_{QW} of 2DEGs in which the electrons are distributed and free to move on the

x-y plane at $z = z_{\mathrm{2DEG},n}$ and that a static magnetic field $\mathbf{B_s}$ is applied along the z direction. For sake of semplicity, we assume that the electromagnetic field distribution varies along z enough slowly to consider it homogeneous within the stack of N_{QW} 2DEGs, and, as such, we assume that light couples equally to all of them. We can write the total Hamiltonian as

$$\hat{H} \approx \hat{H}_{\mathrm{EM}} + \sum_{j=1}^{N} \frac{\left(\hat{\pi}_{\mathbf{j}} + e\hat{\mathbf{A}}(\mathbf{r}_{\parallel,j})\right)^2}{2m^*}, \tag{C.10}$$

where $N = N_{\mathrm{QW}} \cdot N_{\mathrm{2DEG}} S$ is the total number of electrons on the N_{QW} surfaces S with superficial electron density N_{2DEG}, $\mathbf{r}_{\parallel,\mathbf{j}}$ is the electron coordinate on the plane $x - y$, and $\hat{\pi}_j = \hat{\mathbf{p}}_j + e\hat{\mathbf{A}}_0$ is the in-plane momentum coupling with the static vector potential A_0, such that $\mathbf{B_s} = \nabla \times \mathbf{A_0}$.

Let us introduce the bosonic lowering operator between the Landau levels with cyclotron transition frequency ω_c

$$\hat{c}_j = \frac{\hat{\pi}_{y,j} + i\hat{\pi}_{x,j}}{\sqrt{2m^*\hbar\omega_c}}, \tag{C.11}$$

satisfying $[\hat{c}_j, \hat{c}_j^\dagger] = 1$. Then the total Hamiltonian can be rewritten as

$$\begin{aligned}
\hat{H} &= \hat{H}_{\mathrm{EM}} + \sum_{j=1}^{N} \frac{\hat{\pi}_j^2}{2m^*} + \sum_{j=1}^{N} \left[\frac{e}{m^*} \hat{\pi}_{\mathbf{j}} \cdot \hat{\mathbf{A}}(\mathbf{r}_{\parallel,j}) + \frac{e^2}{m^*} \hat{\mathbf{A}}(\mathbf{r}_{\parallel,j})^2 \right] = && \text{(C.12)} \\
&= \hat{H}_{\mathrm{EM}} + \sum_{j=1}^{N} \frac{\hat{\pi}_j^2}{2m^*} + \sum_{j=1}^{N} \left[\frac{e}{m^*} \left(\hat{\pi}_{-,j} \hat{A}_+(\mathbf{r}_{\parallel,j}) + \hat{\pi}_{+,j} \hat{A}_-(\mathbf{r}_{\parallel,j}) \right) \right] && \text{(C.13)} \\
&\quad + \sum_{j=1}^{N} \frac{e^2}{m^*} \hat{A}_-(\mathbf{r}_{\parallel,j}) \hat{A}_+(\mathbf{r}_{\parallel,j}) = \\
&= \hat{H}_{\mathrm{EM}} + \sum_j \hbar\omega_c \left(\hat{c}_j^\dagger \hat{c}_j + \frac{1}{2} \right) + \sum_j \left[\sqrt{\frac{\hbar\omega_c e^2}{m^*}} \left(\hat{c}_j^\dagger \hat{A}_+(\mathbf{r}_{\parallel,j}) + \hat{c}_j \hat{A}_-(\mathbf{r}_{\parallel,j}) \right) \right] \\
&\quad + \sum_{j=1}^{N} \frac{e^2}{m^*} \hat{A}_-(\mathbf{r}_{\parallel,j}) \hat{A}_+(\mathbf{r}_{\parallel,j}), && \text{(C.14)}
\end{aligned}$$

with $\hat{\pi}_{\pm,j} = \left(\hat{\pi}_{x,j} \mp i\hat{\pi}_{y,j}\right)/\sqrt{2}$, which means $\hat{c}_j = \hat{\pi}_{+,j}/\sqrt{m^*\hbar\omega_c}$, and

$$\hat{A}_{\pm}(\mathbf{r}_{\parallel,j}) = \frac{\hat{A}_x(\mathbf{r}_{\parallel,j}) \mp i\hat{A}_y(\mathbf{r}_{\parallel,j})}{\sqrt{2}}. \tag{C.15}$$

Since we defined the vector potential as in Eq.C.6, we can express the two components $\hat{A}_{\pm}(\mathbf{r}_{\parallel,j})$ as

$$\hat{A}_{\pm}(\mathbf{r}_{\parallel,j}) = \sum_{\nu} \mathcal{C}_{\nu} \left(f^*_{\nu,\mp}(\mathbf{r}_{\parallel,j})\hat{a}^{\dagger}_{\nu} + f_{\nu,\pm}(\mathbf{r}_{\parallel,j})\hat{a}_{\nu} \right), \tag{C.16}$$

with $f_{\pm,\nu} = \left(f_{x,\nu} \mp i f_{y,\nu}\right)/\sqrt{2}$. Since we assume real the x and y components of the field, we find $f^*_{\mp,\nu} = f_{\pm,\nu}$, so the vector potential can thus be written as

$$\hat{A}_{\pm}(\mathbf{r}_{\parallel,j}) = \sum_{\nu} \mathcal{C}_{\nu} f_{\pm,\nu}(\mathbf{r}_{\parallel,j}) \left(\hat{a}^{\dagger}_{\nu} + \hat{a}_{\nu}\right). \tag{C.17}$$

Therefore, if we recall $f_{\nu} = f_{\nu,-}$ we can write the total Hamiltonian, as

$$\begin{aligned} \hat{H} \;=\; & \hat{H}_{\mathrm{EM}} + \sum_j \hbar\omega_c \left(\hat{c}^{\dagger}_j \hat{c}_j + \frac{1}{2}\right) + \sqrt{\frac{\hbar\omega_c e^2}{m^*}} \sum_j \sum_{\nu} \mathcal{C}_{\nu} \left[f_{\nu}(\mathbf{r}_{\parallel,j})\hat{c}_j \left(\hat{a}^{\dagger}_{\nu} + \hat{a}_{\nu}\right) + \mathrm{h.c.} \right] + \\ & \frac{e^2}{m^*} \sum_j \sum_{\nu} \sum_{\nu'} \mathcal{C}_{\nu}\mathcal{C}_{\nu'} f_{\nu}(\mathbf{r}_{\parallel,j}) f^*_{\nu'}(\mathbf{r}_{\parallel,j}) \left(\hat{a}^{\dagger}_{\nu} + \hat{a}_{\nu}\right) \left(\hat{a}^{\dagger}_{\nu'} + \hat{a}_{\nu'}\right). \end{aligned} \tag{C.18}$$

Bibliography

[1] E. M. Purcell. "Spontaneous Emission Probabilities at Radio Frequencies". In: *Confined Electrons and Photons*. Ed. by Elias Burstein and Claude Weisbuch. Vol. 340. Boston, MA: Springer US, 1995, pp. 839–839. ISBN: 978-1-4613-5807-7 978-1-4615-1963-8. DOI: 10.1007/978-1-4615-1963-8_40. URL: http://link.springer.com/10.1007/978-1-4615-1963-8_40 (visited on 01/23/2020).

[2] P. Goy et al. "Observation of Cavity-Enhanced Single-Atom Spontaneous Emission". In: *Phys. Rev. Lett.* 50.24 (June 13, 1983), pp. 1903–1906. ISSN: 0031-9007. DOI: 10.1103/PhysRevLett.50.1903. URL: https://link.aps.org/doi/10.1103/PhysRevLett.50.1903 (visited on 01/23/2020).

[3] R. J. Thompson, G. Rempe, and H. J. Kimble. "Observation of Normal-Mode Splitting for an Atom in an Optical Cavity". In: *Phys. Rev. Lett.* 68.8 (Feb. 24, 1992), pp. 1132–1135. ISSN: 0031-9007. DOI: 10.1103/PhysRevLett.68.1132. URL: https://link.aps.org/doi/10.1103/PhysRevLett.68.1132 (visited on 01/23/2020).

[4] D. Meschede, H. Walther, and G. Müller. "One-Atom Maser". In: *Phys. Rev. Lett.* 54.6 (Feb. 11, 1985), pp. 551–554. ISSN: 0031-9007. DOI: 10.1103/PhysRevLett.54.551. URL: https://link.aps.org/doi/10.1103/PhysRevLett.54.551 (visited on 01/23/2020).

[5] C. Weisbuch et al. "Observation of the Coupled Exciton-Photon Mode Splitting in a Semiconductor Quantum Microcavity". In: *Phys. Rev. Lett.* 69.23 (Dec. 7, 1992), pp. 3314–3317. ISSN: 0031-9007. DOI: 10.1103/PhysRevLett.69.3314. URL: https://link.aps.org/doi/10.1103/PhysRevLett.69.3314 (visited on 01/23/2020).

[6] K. Pradeesh, J. J. Baumberg, and G. Vijaya Prakash. "Strong Exciton-Photon Coupling in Inorganic-Organic Multiple Quantum Wells Embedded Low-Q Microcavity". In: *Opt. Express* 17.24 (Nov. 23, 2009), p. 22171. ISSN: 1094-4087. DOI: 10.1364/OE.17.022171. URL: https://www.osapublishing.org/oe/abstract.cfm?uri=oe-17-24-22171 (visited on 02/02/2020).

[7] Peter Lodahl, Sahand Mahmoodian, and Søren Stobbe. "Interfacing Single Photons and Single Quantum Dots with Photonic Nanostructures". In: *Rev. Mod. Phys.* 87.2 (May 11, 2015), pp. 347–400. ISSN: 0034-6861, 1539-0756. DOI: 10.1103/RevModPhys.87.347. URL: https://link.aps.org/doi/10.1103/RevModPhys.87.347 (visited on 01/23/2020).

[8] Xiu Gu et al. "Microwave Photonics with Superconducting Quantum Circuits". In: *Physics Reports* 718-719 (Nov. 2017), pp. 1–102. ISSN: 03701573. DOI: 10.1016/j.physrep.2017.10.002. URL: https://linkinghub.elsevier.com/retrieve/pii/S0370157317303290 (visited on 01/23/2020).

[9] Aji A. Anappara et al. "Signatures of the Ultrastrong Light-Matter Coupling Regime". In: *Phys. Rev. B* 79.20 (May 11, 2009), p. 201303. ISSN: 1098-0121, 1550-235X. DOI: 10.1103/PhysRevB.79.201303. URL: https://link.aps.org/doi/10.1103/PhysRevB.79.201303 (visited on 01/23/2020).

[10] T. Niemczyk et al. “Circuit Quantum Electrodynamics in the Ultrastrong-Coupling Regime”. In: *Nature Phys* 6.10 (Oct. 2010), pp. 772–776. ISSN: 1745-2473, 1745-2481. DOI: 10.1038/nphys1730. URL: http://www.nature.com/articles/nphys1730 (visited on 02/02/2020).

[11] P. Forn-Díaz et al. “Observation of the Bloch-Siegert Shift in a Qubit-Oscillator System in the Ultrastrong Coupling Regime”. In: *Phys. Rev. Lett.* 105.23 (Nov. 30, 2010), p. 237001. ISSN: 0031-9007, 1079-7114. DOI: 10.1103/PhysRevLett.105.237001. URL: https://link.aps.org/doi/10.1103/PhysRevLett.105.237001 (visited on 02/02/2020).

[12] J.B. Khurgin. “Excitonic Radius in the Cavity Polariton in the Regime of Very Strong Coupling”. In: *Solid State Communications* 117.5 (Jan. 2001), pp. 307–310. ISSN: 00381098. DOI: 10.1016/S0038-1098(00)00469-5. URL: https://linkinghub.elsevier.com/retrieve/pii/S0038109800004695 (visited on 02/02/2020).

[13] S. Brodbeck et al. “Experimental Verification of the Very Strong Coupling Regime in a GaAs Quantum Well Microcavity”. In: *Phys. Rev. Lett.* 119.2 (July 12, 2017), p. 027401. ISSN: 0031-9007, 1079-7114. DOI: 10.1103/PhysRevLett.119.027401. URL: http://link.aps.org/doi/10.1103/PhysRevLett.119.027401 (visited on 02/02/2020).

[14] Cristiano Ciuti, Gérald Bastard, and Iacopo Carusotto. “Quantum Vacuum Properties of the Intersubband Cavity Polariton Field”. In: *Phys. Rev. B* 72.11 (Sept. 2, 2005), p. 115303. ISSN: 1098-0121, 1550-235X. DOI: 10.1103/PhysRevB.72.115303. URL: https://link.aps.org/doi/10.1103/PhysRevB.72.115303 (visited on 01/23/2020).

[15] T. Werlang et al. “Rabi Model beyond the Rotating-Wave Approximation: Generation of Photons from Vacuum through Decoherence”. In: *Phys. Rev. A* 78.5 (Nov. 5, 2008), p. 053805. ISSN: 1050-2947, 1094-1622. DOI: 10.1103/PhysRevA.78.053805. URL: https://link.aps.org/doi/10.1103/PhysRevA.78.053805 (visited on 01/24/2020).

[16] X Cao et al. “A Qubit Strongly Coupled to a Resonant Cavity: Asymmetry of the Spontaneous Emission Spectrum beyond the Rotating Wave Approximation”. In: *New J. Phys.* 13.7 (July 5, 2011), p. 073002. ISSN: 1367-2630. DOI: 10.1088/1367-2630/13/7/073002. URL: http://stacks.iop.org/1367-2630/13/i=7/a=073002?key=crossref.1d52c35441ce29dadb1c9a3061a6dee1 (visited on 02/02/2020).

[17] A. Ridolfo et al. “Photon Blockade in the Ultrastrong Coupling Regime”. In: *Phys. Rev. Lett.* 109.19 (Nov. 8, 2012), p. 193602. ISSN: 0031-9007, 1079-7114. DOI: 10.1103/PhysRevLett.109.193602. URL: https://link.aps.org/doi/10.1103/PhysRevLett.109.193602 (visited on 02/02/2020).

[18] Simone De Liberato. “Light-Matter Decoupling in the Deep Strong Coupling Regime: The Breakdown of the Purcell Effect”. In: *Phys. Rev. Lett.* 112.1 (Jan. 6, 2014), p. 016401. ISSN: 0031-9007, 1079-7114. DOI: 10.1103/PhysRevLett.112.016401. URL: https://link.aps.org/doi/10.1103/PhysRevLett.112.016401 (visited on 01/24/2020).

[19] Luigi Garziano et al. “One Photon Can Simultaneously Excite Two or More Atoms”. In: *Phys. Rev. Lett.* 117.4 (July 22, 2016), p. 043601. ISSN: 0031-9007, 1079-7114. DOI: 10.1103/PhysRevLett.117.043601. URL: https://link.aps.org/doi/10.1103/PhysRevLett.117.043601 (visited on 01/24/2020).

[20] Simone De Liberato, Cristiano Ciuti, and Iacopo Carusotto. “Quantum Vacuum Radiation Spectra from a Semiconductor Microcavity with a Time-Modulated Vacuum Rabi Frequency”. In: *Phys. Rev. Lett.* 98.10 (Mar. 8, 2007), p. 103602. ISSN: 0031-9007, 1079-7114. DOI: 10.1103/PhysRevLett.98.103602. URL: https://link.aps.org/doi/10.1103/PhysRevLett.98.103602 (visited on 02/02/2020).

[21] Simone De Liberato and Cristiano Ciuti. “Stimulated Scattering and Lasing of Intersubband Cavity Polaritons”. In: *Phys. Rev. Lett.* 102.13 (Mar. 31, 2009), p. 136403. ISSN: 0031-9007, 1079-7114. DOI: 10.1103/PhysRevLett.102.136403. URL: https://link.aps.org/doi/10.1103/PhysRevLett.102.136403 (visited on 02/02/2020).

[22] P. Forn-Dıaz et al. “Ultrastrong coupling regimes of light-matter interaction”. In: *Rev. Mod. Phys.* 91 (2 June 2019), p. 025005. DOI: 10.1103/RevModPhys.91.025005. URL: https://link.aps.org/doi/10.1103/RevModPhys.91.025005.

[23] Anton Frisk Kockum et al. “Ultrastrong coupling between light and matter”. In: *Nature Reviews Physics* 1.1 (2019), pp. 19–40.

[24] Johannes Flick et al. “Atoms and Molecules in Cavities, from Weak to Strong Coupling in Quantum-Electrodynamics (QED) Chemistry”. In: *Proc Natl Acad Sci USA* 114.12 (Mar. 21, 2017), pp. 3026–3034. ISSN: 0027-8424, 1091-6490. DOI: 10.1073/pnas.1615509114. URL: http://www.pnas.org/lookup/doi/10.1073/pnas.1615509114 (visited on 02/02/2020).

[25] Luis A. Martínez-Martínez et al. “Can Ultrastrong Coupling Change Ground-State Chemical Reactions?” In: *ACS Photonics* 5.1 (Jan. 17, 2018), pp. 167–176. ISSN: 2330-4022, 2330-4022. DOI: 10.1021/acsphotonics.7b00610. URL: https://pubs.acs.org/doi/10.1021/acsphotonics.7b00610 (visited on 02/02/2020).

[26] Luis A. Martínez-Martínez et al. “Polariton-Assisted Singlet Fission in Acene Aggregates”. In: *J. Phys. Chem. Lett.* 9.8 (Apr. 19, 2018), pp. 1951–1957. ISSN: 1948-7185. DOI: 10.1021/acs.jpclett.8b00008. URL: https://pubs.acs.org/doi/10.1021/acs.jpclett.8b00008 (visited on 02/02/2020).

[27] Javier Galego, Francisco J. Garcia-Vidal, and Johannes Feist. “Suppressing Photochemical Reactions with Quantized Light Fields”. In: *Nat Commun* 7.1 (Dec. 2016), p. 13841. ISSN: 2041-1723. DOI: 10.1038/ncomms13841. URL: http://www.nature.com/articles/ncomms13841 (visited on 02/02/2020).

[28] Markus Kowalewski, Kochise Bennett, and Shaul Mukamel. “Cavity Femtochemistry: Manipulating Nonadiabatic Dynamics at Avoided Crossings”. In: *J. Phys. Chem. Lett.* 7.11 (June 2, 2016), pp. 2050–2054. ISSN: 1948-7185. DOI: 10.1021/acs.jpclett.6b00864. URL: https://pubs.acs.org/doi/10.1021/acs.jpclett.6b00864 (visited on 02/02/2020).

[29] James A. Hutchison et al. “Modifying Chemical Landscapes by Coupling to Vacuum Fields”. In: *Angew. Chem. Int. Ed.* 51.7 (Feb. 13, 2012), pp. 1592–1596. ISSN: 14337851. DOI: 10.1002/anie.201107033. URL: http://doi.wiley.com/10.1002/anie.201107033 (visited on 02/02/2020).

[30] Hoi Ling Luk et al. “Multiscale Molecular Dynamics Simulations of Polaritonic Chemistry”. In: *J. Chem. Theory Comput.* 13.9 (Sept. 12, 2017), pp. 4324–4335. ISSN: 1549-9618, 1549-9626. DOI: 10.1021/acs.

jctc.7b00388. URL: https://pubs.acs.org/doi/10.1021/acs.jctc.7b00388 (visited on 02/02/2020).

[31] Javier Galego, Francisco J. Garcia-Vidal, and Johannes Feist. "Cavity-Induced Modifications of Molecular Structure in the Strong-Coupling Regime". In: *Phys. Rev. X* 5.4 (Nov. 9, 2015), p. 041022. ISSN: 2160-3308. DOI: 10.1103/PhysRevX.5.041022. URL: https://link.aps.org/doi/10.1103/PhysRevX.5.041022 (visited on 01/24/2020).

[32] Jonathan Keeling and Peter G. Kirton. "Orientational Alignment in Cavity Quantum Electrodynamics". In: *Phys. Rev. A* 97.5 (May 29, 2018), p. 053836. ISSN: 2469-9926, 2469-9934. DOI: 10.1103/PhysRevA.97.053836. URL: https://link.aps.org/doi/10.1103/PhysRevA.97.053836 (visited on 02/02/2020).

[33] Justyna A. Ćwik et al. "Excitonic Spectral Features in Strongly Coupled Organic Polaritons". In: *Phys. Rev. A* 93.3 (Mar. 22, 2016), p. 033840. ISSN: 2469-9926, 2469-9934. DOI: 10.1103/PhysRevA.93.033840. URL: https://link.aps.org/doi/10.1103/PhysRevA.93.033840 (visited on 02/02/2020).

[34] Michael Ruggenthaler et al. "Quantum-Electrodynamical Density-Functional Theory: Bridging Quantum Optics and Electronic-Structure Theory". In: *Phys. Rev. A* 90.1 (July 9, 2014), p. 012508. ISSN: 1050-2947, 1094-1622. DOI: 10.1103/PhysRevA.90.012508. URL: https://link.aps.org/doi/10.1103/PhysRevA.90.012508 (visited on 02/02/2020).

[35] Javier Galego, Francisco J. Garcia-Vidal, and Johannes Feist. "Many-Molecule Reaction Triggered by a Single Photon in Polaritonic Chemistry". In: *Phys. Rev. Lett.* 119.13 (Sept. 27, 2017), p. 136001. ISSN: 0031-9007, 1079-7114. DOI: 10.1103/PhysRevLett.119.136001. URL: https://link.aps.org/doi/10.1103/PhysRevLett.119.136001 (visited on 02/02/2020).

[36] Johannes Feist, Javier Galego, and Francisco J. Garcia-Vidal. "Polaritonic Chemistry with Organic Molecules". In: *ACS Photonics* 5.1 (Jan. 17, 2018), pp. 205–216. ISSN: 2330-4022, 2330-4022. DOI: 10.1021/acsphotonics.7b00680. URL: https://pubs.acs.org/doi/10.1021/acsphotonics.7b00680 (visited on 02/02/2020).

[37] Rohit Chikkaraddy et al. “Single-Molecule Strong Coupling at Room Temperature in Plasmonic Nanocavities”. In: *Nature* 535.7610 (July 2016), pp. 127–130. ISSN: 0028-0836, 1476-4687. DOI: 10.1038/nature17974. URL: http://www.nature.com/articles/nature17974 (visited on 02/02/2020).

[38] L. Garziano et al. “Switching on and off of Ultrastrong Light-Matter Interaction: Photon Statistics of Quantum Vacuum Radiation”. In: *Phys. Rev. A* 88.6 (Dec. 17, 2013), p. 063829. ISSN: 1050-2947, 1094-1622. DOI: 10.1103/PhysRevA.88.063829. URL: https://link.aps.org/doi/10.1103/PhysRevA.88.063829 (visited on 01/24/2020).

[39] C. K. Law. “Vacuum Rabi Oscillation Induced by Virtual Photons in the Ultrastrong-Coupling Regime”. In: *Phys. Rev. A* 87.4 (Apr. 19, 2013), p. 045804. ISSN: 1050-2947, 1094-1622. DOI: 10.1103/PhysRevA.87.045804. URL: https://link.aps.org/doi/10.1103/PhysRevA.87.045804 (visited on 02/02/2020).

[40] Daniele De Bernardis et al. “Breakdown of Gauge Invariance in Ultrastrong-Coupling Cavity QED”. In: *Phys. Rev. A* 98.5 (Nov. 13, 2018), p. 053819. ISSN: 2469-9926, 2469-9934. DOI: 10.1103/PhysRevA.98.053819. URL: https://link.aps.org/doi/10.1103/PhysRevA.98.053819 (visited on 02/06/2020).

[41] Bruce W. Shore and Peter L. Knight. “The Jaynes-Cummings Model”. In: *Journal of Modern Optics* 40.7 (July 1993), pp. 1195–1238. ISSN: 0950-0340, 1362-3044. DOI: 10.1080/09500349314551321. URL: http://www.tandfonline.com/doi/abs/10.1080/09500349314551321 (visited on 02/02/2020).

[42] D. Braak. “Integrability of the Rabi Model”. In: *Phys. Rev. Lett.* 107.10 (Aug. 29, 2011), p. 100401. ISSN: 0031-9007, 1079-7114. DOI: 10.1103/PhysRevLett.107.100401. URL: https://link.aps.org/doi/10.1103/PhysRevLett.107.100401 (visited on 02/02/2020).

[43] R. H. Dicke. “Coherence in Spontaneous Radiation Processes”. In: *Phys. Rev.* 93.1 (Jan. 1, 1954), pp. 99–110. ISSN: 0031-899X. DOI: 10.1103/PhysRev.93.99. URL: https://link.aps.org/doi/10.1103/PhysRev.93.99 (visited on 01/25/2020).

[44] Michael Tavis and Frederick W. Cummings. "Exact Solution for an N - Molecule—Radiation-Field Hamiltonian". In: *Phys. Rev.* 170.2 (June 10, 1968), pp. 379–384. ISSN: 0031-899X. DOI: 10.1103/PhysRev.170.379. URL: https://link.aps.org/doi/10.1103/PhysRev.170.379 (visited on 02/02/2020).

[45] Pierre Nataf and Cristiano Ciuti. "No-Go Theorem for Superradiant Quantum Phase Transitions in Cavity QED and Counter-Example in Circuit QED". In: *Nat Commun* 1.1 (Dec. 2010), p. 72. ISSN: 2041-1723. DOI: 10.1038/ncomms1069. URL: http://www.nature.com/articles/ncomms1069 (visited on 02/04/2020).

[46] Motoaki Bamba and Tetsuo Ogawa. "Stability of Polarizable Materials against Superradiant Phase Transition". In: *Phys. Rev. A* 90.6 (Dec. 16, 2014), p. 063825. ISSN: 1050-2947, 1094-1622. DOI: 10.1103/PhysRevA.90.063825. URL: https://link.aps.org/doi/10.1103/PhysRevA.90.063825 (visited on 02/04/2020).

[47] Klaus Hepp and Elliott H Lieb. "On the Superradiant Phase Transition for Molecules in a Quantized Radiation Field: The Dicke Maser Model". In: *Annals of Physics* 76.2 (Apr. 1973), pp. 360–404. ISSN: 00034916. DOI: 10.1016/0003-4916(73)90039-0. URL: https://linkinghub.elsevier.com/retrieve/pii/0003491673900390 (visited on 02/04/2020).

[48] Y. K. Wang and F. T. Hioe. "Phase Transition in the Dicke Model of Superradiance". In: *Phys. Rev. A* 7.3 (Mar. 1, 1973), pp. 831–836. ISSN: 0556-2791. DOI: 10.1103/PhysRevA.7.831. URL: https://link.aps.org/doi/10.1103/PhysRevA.7.831 (visited on 02/04/2020).

[49] Clive Emary and Tobias Brandes. "Chaos and the Quantum Phase Transition in the Dicke Model". In: *Phys. Rev. E* 67.6 (June 12, 2003), p. 066203. ISSN: 1063-651X, 1095-3787. DOI: 10.1103/PhysRevE.67.066203. URL: https://link.aps.org/doi/10.1103/PhysRevE.67.066203 (visited on 02/04/2020).

[50] S. Ashhab and K. Semba. "Superradiance Phase Transition in the Presence of Parameter Fluctuations". In: *Phys. Rev. A* 95.5 (May 11, 2017), p. 053833. ISSN: 2469-9926, 2469-9934. DOI: 10.1103/PhysRevA.95.053833. URL: http://link.aps.org/doi/10.1103/PhysRevA.95.053833 (visited on 02/04/2020).

[51] J. J. Hopfield. "Theory of the Contribution of Excitons to the Complex Dielectric Constant of Crystals". In: *Phys. Rev.* 112.5 (Dec. 1, 1958), pp. 1555–1567. ISSN: 0031-899X. DOI: 10.1103/PhysRev.112.1555. URL: https://link.aps.org/doi/10.1103/PhysRev.112.1555 (visited on 02/02/2020).

[52] S. Brodbeck et al. "Experimental Verification of the Very Strong Coupling Regime in a GaAs Quantum Well Microcavity". In: *Phys. Rev. Lett.* 119.2 (July 12, 2017), p. 027401. ISSN: 0031-9007, 1079-7114. DOI: 10.1103/PhysRevLett.119.027401. URL: http://link.aps.org/doi/10.1103/PhysRevLett.119.027401 (visited on 02/02/2020).

[53] J. Casanova et al. "Deep Strong Coupling Regime of the Jaynes-Cummings Model". In: *Phys. Rev. Lett.* 105.26 (Dec. 20, 2010), p. 263603. ISSN: 0031-9007, 1079-7114. DOI: 10.1103/PhysRevLett.105.263603. URL: https://link.aps.org/doi/10.1103/PhysRevLett.105.263603 (visited on 02/03/2020).

[54] Andreas Bayer et al. "Terahertz Light–Matter Interaction beyond Unity Coupling Strength". In: *Nano Lett.* 17.10 (Oct. 11, 2017), pp. 6340–6344. ISSN: 1530-6984, 1530-6992. DOI: 10.1021/acs.nanolett.7b03103. URL: https://pubs.acs.org/doi/10.1021/acs.nanolett.7b03103 (visited on 01/24/2020).

[55] Fumiki Yoshihara et al. "Superconducting Qubit–Oscillator Circuit beyond the Ultrastrong-Coupling Regime". In: *Nature Phys* 13.1 (Jan. 2017), pp. 44–47. ISSN: 1745-2473, 1745-2481. DOI: 10.1038/nphys3906. URL: http://www.nature.com/articles/nphys3906 (visited on 01/24/2020).

[56] Daniele De Bernardis, Tuomas Jaako, and Peter Rabl. "Cavity Quantum Electrodynamics in the Nonperturbative Regime". In: *Phys. Rev. A* 97.4 (Apr. 11, 2018), p. 043820. ISSN: 2469-9926, 2469-9934. DOI: 10.1103/PhysRevA.97.043820. URL: https://link.aps.org/doi/10.1103/PhysRevA.97.043820 (visited on 01/24/2020).

[57] Vladimir M Agranovich. *Excitations in Organic Solids*. Vol. 142. OUP Oxford, 2009.

[58] Gülis Zengin et al. "Approaching the Strong Coupling Limit in Single Plasmonic Nanorods Interacting with J-Aggregates". In: *Sci Rep* 3.1 (Nov. 2013), p. 3074. ISSN: 2045-2322. DOI: 10.1038/srep03074.

URL: http://www.nature.com/articles/srep03074 (visited on 02/04/2020).

[59] D. G. Lidzey et al. "Strong Exciton–Photon Coupling in an Organic Semiconductor Microcavity". In: *Nature* 395.6697 (Sept. 1998), pp. 53–55. ISSN: 0028-0836, 1476-4687. DOI: 10.1038/25692. URL: http://www.nature.com/articles/25692 (visited on 02/04/2020).

[60] Christopher R. Gubbin, Stefan A. Maier, and Stéphane Kéna-Cohen. "Low-Voltage Polariton Electroluminescence from an Ultrastrongly Coupled Organic Light-Emitting Diode". In: *Appl. Phys. Lett.* 104.23 (June 9, 2014), p. 233302. ISSN: 0003-6951, 1077-3118. DOI: 10.1063/1.4871271. URL: http://aip.scitation.org/doi/10.1063/1.4871271 (visited on 02/04/2020).

[61] P. Jordan and E. P. Wigner. "Über Das Paulische Äquivalenzverbot". In: *The Collected Works of Eugene Paul Wigner*. Ed. by Arthur S. Wightman. Berlin, Heidelberg: Springer Berlin Heidelberg, 1993, pp. 109–129. ISBN: 978-3-642-08154-5 978-3-662-02781-3. DOI: 10.1007/978-3-662-02781-3_9. URL: http://link.springer.com/10.1007/978-3-662-02781-3_9 (visited on 02/04/2020).

[62] Eduardo Fradkin. "Jordan-Wigner Transformation for Quantum-Spin Systems in Two Dimensions and Fractional Statistics". In: *Phys. Rev. Lett.* 63.3 (July 17, 1989), pp. 322–325. ISSN: 0031-9007. DOI: 10.1103/PhysRevLett.63.322. URL: https://link.aps.org/doi/10.1103/PhysRevLett.63.322 (visited on 02/04/2020).

[63] Søren Gammelmark and Klaus Mølmer. "Phase Transitions and Heisenberg Limited Metrology in an Ising Chain Interacting with a Single-Mode Cavity Field". In: *New J. Phys.* 13.5 (May 19, 2011), p. 053035. ISSN: 1367-2630. DOI: 10.1088/1367-2630/13/5/053035. URL: http://stacks.iop.org/1367-2630/13/i=5/a=053035?key=crossref.a6fb7f7739974a7fcaea8b4186fb46ab (visited on 02/04/2020).

[64] Yuanwei Zhang et al. "Quantum Phases in Circuit QED with a Superconducting Qubit Array". In: *Sci Rep* 4.1 (May 2015), p. 4083. ISSN: 2045-2322. DOI: 10.1038/srep04083. URL: http://www.nature.com/articles/srep04083 (visited on 02/04/2020).

[65] Søren Gammelmark and Klaus Mølmer. "Interacting Spins in a Cavity: Finite-Size Effects and Symmetry-Breaking Dynamics". In: *Phys. Rev. A* 85.4 (Apr. 25, 2012), p. 042114. ISSN: 1050-2947, 1094-1622. DOI: 10.1103/PhysRevA.85.042114. URL: https://link.aps.org/doi/10.1103/PhysRevA.85.042114 (visited on 02/04/2020).

[66] T. Holstein and H. Primakoff. "Field Dependence of the Intrinsic Domain Magnetization of a Ferromagnet". In: *Phys. Rev.* 58.12 (Dec. 15, 1940), pp. 1098–1113. ISSN: 0031-899X. DOI: 10.1103/PhysRev.58.1098. URL: https://link.aps.org/doi/10.1103/PhysRev.58.1098 (visited on 02/04/2020).

[67] Lisette D. Bakalis and Jasper Knoester. "Optical Properties of One-Dimensional Exciton Systems: Beyond the Heitler-London Approximation". In: *The Journal of Chemical Physics* 106.17 (May 1997), pp. 6964–6976. ISSN: 0021-9606, 1089-7690. DOI: 10.1063/1.473676. URL: http://aip.scitation.org/doi/10.1063/1.473676 (visited on 02/04/2020).

[68] SI Pekar. "The Theory of Electromagnetic Waves in a Crystal in Which Excitons Are Produced". In: 6.33 (1958), p. 4.

[69] L. Garziano et al. "Vacuum-Induced Symmetry Breaking in a Superconducting Quantum Circuit". In: *Phys. Rev. A* 90.4 (Oct. 13, 2014), p. 043817. ISSN: 1050-2947, 1094-1622. DOI: 10.1103/PhysRevA.90.043817. URL: https://link.aps.org/doi/10.1103/PhysRevA.90.043817 (visited on 02/04/2020).

[70] Anton Frisk Kockum et al. "Deterministic Quantum Nonlinear Optics with Single Atoms and Virtual Photons". In: *Phys. Rev. A* 95.6 (June 29, 2017), p. 063849. ISSN: 2469-9926, 2469-9934. DOI: 10.1103/PhysRevA.95.063849. URL: http://link.aps.org/doi/10.1103/PhysRevA.95.063849 (visited on 01/24/2020).

[71] Kazuhiko Misawa et al. "Giant Static Dipole Moment Change on Electronic Excitation in Highly Oriented J-Aggregates". In: *Chemical Physics Letters* 220.3-5 (Apr. 1994), pp. 251–256. ISSN: 00092614. DOI: 10.1016/0009-2614(94)00180-4. URL: https://linkinghub.elsevier.com/retrieve/pii/0009261494001804 (visited on 02/04/2020).

[72] J. Dintinger et al. "Strong Coupling between Surface Plasmon-Polaritons and Organic Molecules in Subwavelength Hole Arrays". In: *Phys. Rev. B* 71.3 (Jan. 28, 2005), p. 035424. ISSN: 1098-0121, 1550-235X. DOI: 10.1103/PhysRevB.71.035424. URL: https://link.aps.org/doi/10.1103/PhysRevB.71.035424 (visited on 02/04/2020).

[73] Salvatore Gambino et al. "Exploring Light–Matter Interaction Phenomena under Ultrastrong Coupling Regime". In: *ACS Photonics* 1.10 (Oct. 15, 2014), pp. 1042–1048. ISSN: 2330-4022, 2330-4022. DOI: 10.1021/ph500266d. URL: https://pubs.acs.org/doi/10.1021/ph500266d (visited on 02/04/2020).

[74] Javier Galego et al. "Cavity Casimir-Polder Forces and Their Effects in Ground-State Chemical Reactivity". In: *Phys. Rev. X* 9.2 (June 21, 2019), p. 021057. ISSN: 2160-3308. DOI: 10.1103/PhysRevX.9.021057. URL: https://link.aps.org/doi/10.1103/PhysRevX.9.021057 (visited on 02/04/2020).

[75] C Emary. "Dark-States in Multi-Mode Multi-Atom Jaynes–Cummings Systems". In: *J. Phys. B: At. Mol. Opt. Phys.* 46.22 (Nov. 28, 2013), p. 224008. ISSN: 0953-4075, 1361-6455. DOI: 10.1088/0953-4075/46/22/224008. URL: http://stacks.iop.org/0953-4075/46/i=22/a=224008?key=crossref.848bc2c04f003216607d228d5a65d7e3 (visited on 02/04/2020).

[76] K. S. Daskalakis et al. "Nonlinear Interactions in an Organic Polariton Condensate". In: *Nature Mater* 13.3 (Mar. 2014), pp. 271–278. ISSN: 1476-1122, 1476-4660. DOI: 10.1038/nmat3874. URL: http://www.nature.com/articles/nmat3874 (visited on 02/15/2020).

[77] Hagen Kleinert. *Path Integrals in Quantum Mechanics, Statistics and Polymer Physics*. Jan. 1995. DOI: 10.1142/1081.

[78] T. Schwartz et al. "Reversible Switching of Ultrastrong Light-Molecule Coupling". In: *Phys. Rev. Lett.* 106.19 (May 11, 2011), p. 196405. ISSN: 0031-9007, 1079-7114. DOI: 10.1103/PhysRevLett.106.196405. URL: https://link.aps.org/doi/10.1103/PhysRevLett.106.196405 (visited on 02/15/2020).

[79] Stéphane Kéna-Cohen, Stefan A. Maier, and Donal D. C. Bradley. "Ultrastrongly Coupled Exciton-Polaritons in Metal-Clad Organic Semiconductor Microcavities". In: *Advanced Optical Materials* 1.11 (Nov.

2013), pp. 827–833. ISSN: 21951071. DOI: 10.1002/adom.201300256. URL: http://doi.wiley.com/10.1002/adom.201300256 (visited on 02/15/2020).

[80] Christopher R. Gubbin, Stefan A. Maier, and Stéphane Kéna-Cohen. "Low-Voltage Polariton Electroluminescence from an Ultrastrongly Coupled Organic Light-Emitting Diode". In: *Appl. Phys. Lett.* 104.23 (June 9, 2014), p. 233302. ISSN: 0003-6951, 1077-3118. DOI: 10.1063/1.4871271. URL: http://aip.scitation.org/doi/10.1063/1.4871271 (visited on 02/15/2020).

[81] Jino George et al. "Liquid-Phase Vibrational Strong Coupling". In: *J. Phys. Chem. Lett.* 6.6 (Mar. 19, 2015), pp. 1027–1031. ISSN: 1948-7185. DOI: 10.1021/acs.jpclett.5b00204. URL: https://pubs.acs.org/doi/10.1021/acs.jpclett.5b00204 (visited on 02/15/2020).

[82] S. Schwarz et al. "Two-Dimensional Metal–Chalcogenide Films in Tunable Optical Microcavities". In: *Nano Lett.* 14.12 (Dec. 10, 2014), pp. 7003–7008. ISSN: 1530-6984, 1530-6992. DOI: 10.1021/nl503312x. URL: https://pubs.acs.org/doi/10.1021/nl503312x (visited on 02/15/2020).

[83] Jino George et al. "Multiple Rabi Splittings under Ultrastrong Vibrational Coupling". In: *Phys. Rev. Lett.* 117.15 (Oct. 6, 2016), p. 153601. ISSN: 0031-9007, 1079-7114. DOI: 10.1103/PhysRevLett.117.153601. URL: https://link.aps.org/doi/10.1103/PhysRevLett.117.153601 (visited on 02/15/2020).

[84] Jonathan Keeling and Peter G. Kirton. "Orientational Alignment in Cavity Quantum Electrodynamics". In: *Phys. Rev. A* 97.5 (May 29, 2018), p. 053836. ISSN: 2469-9926, 2469-9934. DOI: 10.1103/PhysRevA.97.053836. URL: https://link.aps.org/doi/10.1103/PhysRevA.97.053836 (visited on 02/15/2020).

[85] E. Orgiu et al. "Conductivity in Organic Semiconductors Hybridized with the Vacuum Field". In: *Nature Mater* 14.11 (Nov. 2015), pp. 1123–1129. ISSN: 1476-1122, 1476-4660. DOI: 10.1038/nmat4392. URL: http://www.nature.com/articles/nmat4392 (visited on 02/15/2020).

[86] Johannes Feist and Francisco J. Garcia-Vidal. "Extraordinary Exciton Conductance Induced by Strong Coupling". In: *Phys. Rev. Lett.* 114.19 (May 12, 2015), p. 196402. ISSN: 0031-9007, 1079-7114. DOI:

10.1103/PhysRevLett.114.196402. URL: https://link.aps.org/doi/10.1103/PhysRevLett.114.196402 (visited on 02/15/2020).

[87] Gian L. Paravicini-Bagliani et al. "Magneto-Transport Controlled by Landau Polariton States". In: *Nature Phys* 15.2 (Feb. 2019), pp. 186–190. ISSN: 1745-2473, 1745-2481. DOI: 10.1038/s41567-018-0346-y. URL: http://www.nature.com/articles/s41567-018-0346-y (visited on 02/15/2020).

[88] Y. Avishai, Y. B. Band, and M. Trippenbach. "Feshbach Resonance without a Closed-Channel Bound State". In: *Phys. Rev. Lett.* 111.15 (Oct. 11, 2013), p. 155301. ISSN: 0031-9007, 1079-7114. DOI: 10.1103/PhysRevLett.111.155301. URL: https://link.aps.org/doi/10.1103/PhysRevLett.111.155301 (visited on 04/22/2020).

[89] Federico Capasso et al. "Observation of an Electronic Bound State above a Potential Well". In: *Nature* 358.6387 (Aug. 1992), pp. 565–567. ISSN: 0028-0836, 1476-4687. DOI: 10.1038/358565a0. URL: http://www.nature.com/articles/358565a0 (visited on 02/15/2020).

[90] R P Seisyan et al. "The excitonic structure of absorption and magnetoabsorption spectra near the type I-II transition in strained (In, Ga)As/GaAs heterostructures". In: *Semiconductor Science and Technology* 10.5 (May 1995), pp. 611–615. DOI: 10.1088/0268-1242/10/5/007. URL: https://doi.org/10.1088%2F0268-1242%2F10%2F5%2F007.

[91] Dmitri E. Nikonov et al. "Collective Intersubband Excitations in Quantum Wells: Coulomb Interaction versus Subband Dispersion". In: *Phys. Rev. Lett.* 79 (23 Dec. 1997), pp. 4633–4636. DOI: 10.1103/PhysRevLett.79.4633. URL: https://link.aps.org/doi/10.1103/PhysRevLett.79.4633.

[92] A. V. Kavokin et al. "Quantum wells with zero valence-band offset: Drastic enhancement of forbidden excitonic transitions". In: *Phys. Rev. B* 54 (16 Oct. 1996), R11078–R11081. DOI: 10.1103/PhysRevB.54.R11078. URL: https://link.aps.org/doi/10.1103/PhysRevB.54.R11078.

[93] A. V. Kavokin et al. "The effect of a "Coulomb well" on the absorption and magnetoabsorption spectra of strained InGaAs/GaAs heterostructures". In: *Semiconductors* 31.9 (1997), pp. 950–960. ISSN:

1090-6479. DOI: 10.1134/1.1187141. URL: https://doi.org/10.1134/1.1187141.

[94] M. R. Vladimirova et al. "Above-barrier excitons: First magnetooptic investigation". In: *Journal of Experimental and Theoretical Physics Letters* 69.10 (1999), pp. 779–784. ISSN: 1090-6487. DOI: 10.1134/1.568090. URL: https://doi.org/10.1134/1.568090.

[95] Dimitri Dini et al. "Microcavity Polariton Splitting of Intersubband Transitions". In: *Phys. Rev. Lett.* 90.11 (Mar. 18, 2003), p. 116401. ISSN: 0031-9007, 1079-7114. DOI: 10.1103/PhysRevLett.90.116401. URL: https://link.aps.org/doi/10.1103/PhysRevLett.90.116401 (visited on 04/14/2020).

[96] Benjamin Askenazi et al. "Midinfrared Ultrastrong Light–Matter Coupling for THz Thermal Emission". In: *ACS Photonics* 4.10 (Oct. 18, 2017), pp. 2550–2555. ISSN: 2330-4022, 2330-4022. DOI: 10.1021/acsphotonics.7b00838. URL: https://pubs.acs.org/doi/10.1021/acsphotonics.7b00838 (visited on 04/19/2020).

[97] Y. Todorov et al. "Optical Properties of Metal-Dielectric-Metal Microcavities in the THz Frequency Range". In: *Opt. Express* 18.13 (June 21, 2010), p. 13886. ISSN: 1094-4087. DOI: 10.1364/OE.18.013886. URL: https://www.osapublishing.org/oe/abstract.cfm?uri=oe-18-13-13886 (visited on 02/15/2020).

[98] J.-M. Manceau et al. "Resonant Intersubband Polariton-LO Phonon Scattering in an Optically Pumped Polaritonic Device". In: *Appl. Phys. Lett.* 112.19 (May 7, 2018), p. 191106. ISSN: 0003-6951, 1077-3118. DOI: 10.1063/1.5029893. URL: http://aip.scitation.org/doi/10.1063/1.5029893 (visited on 04/18/2020).

[99] Y. Chassagneux et al. "Electrically Pumped Photonic-Crystal Terahertz Lasers Controlled by Boundary Conditions". In: *Nature* 457.7226 (Jan. 2009), pp. 174–178. ISSN: 0028-0836, 1476-4687. DOI: 10.1038/nature07636. URL: http://www.nature.com/articles/nature07636 (visited on 04/18/2020).

[100] U. Fano. "Effects of Configuration Interaction on Intensities and Phase Shifts". In: *Phys. Rev.* 124.6 (Dec. 15, 1961), pp. 1866–1878. ISSN: 0031-899X. DOI: 10.1103/PhysRev.124.1866. URL: https://link.aps.org/doi/10.1103/PhysRev.124.1866 (visited on 02/15/2020).

[101] Yanko Todorov and Carlo Sirtori. "Intersubband Polaritons in the Electrical Dipole Gauge". In: *Phys. Rev. B* 85.4 (Jan. 6, 2012), p. 045304. ISSN: 1098-0121, 1550-235X. DOI: 10.1103/PhysRevB.85.045304. URL: https://link.aps.org/doi/10.1103/PhysRevB.85.045304 (visited on 02/15/2020).

[102] Yanko Todorov. "Dipolar Quantum Electrodynamics of the Two-Dimensional Electron Gas". In: *Phys. Rev. B* 91.12 (Mar. 6, 2015), p. 125409. ISSN: 1098-0121, 1550-235X. DOI: 10.1103/PhysRevB.91.125409. URL: https://link.aps.org/doi/10.1103/PhysRevB.91.125409 (visited on 04/16/2020).

[103] Simone De Liberato and Cristiano Ciuti. "Stimulated Scattering and Lasing of Intersubband Cavity Polaritons". In: *Phys. Rev. Lett.* 102.13 (Mar. 31, 2009), p. 136403. ISSN: 0031-9007, 1079-7114. DOI: 10.1103/PhysRevLett.102.136403. URL: https://link.aps.org/doi/10.1103/PhysRevLett.102.136403 (visited on 01/24/2020).

[104] Y. Kaluzny et al. "Observation of Self-Induced Rabi Oscillations in Two-Level Atoms Excited Inside a Resonant Cavity: The Ringing Regime of Superradiance". In: *Phys. Rev. Lett.* 51.13 (Sept. 26, 1983), pp. 1175–1178. ISSN: 0031-9007. DOI: 10.1103/PhysRevLett.51.1175. URL: https://link.aps.org/doi/10.1103/PhysRevLett.51.1175 (visited on 01/23/2020).

[105] Tsuneya Ando, Alan B. Fowler, and Frank Stern. "Electronic Properties of Two-Dimensional Systems". In: *Rev. Mod. Phys.* 54.2 (Apr. 1, 1982), pp. 437–672. ISSN: 0034-6861. DOI: 10.1103/RevModPhys.54.437. URL: https://link.aps.org/doi/10.1103/RevModPhys.54.437 (visited on 04/19/2020).

[106] Simone De Liberato and Cristiano Ciuti. "Quantum Model of Microcavity Intersubband Electroluminescent Devices". In: *Phys. Rev. B* 77.15 (Apr. 22, 2008), p. 155321. ISSN: 1098-0121, 1550-235X. DOI: 10.1103/PhysRevB.77.155321. URL: https://link.aps.org/doi/10.1103/PhysRevB.77.155321 (visited on 04/19/2020).

[107] Raffaele Colombelli and Jean-Michel Manceau. "Perspectives for Intersubband Polariton Lasers". In: *Phys. Rev. X* 5.1 (Mar. 23, 2015), p. 011031. ISSN: 2160-3308. DOI: 10.1103/PhysRevX.5.011031. URL: https://link.aps.org/doi/10.1103/PhysRevX.5.011031 (visited on 04/19/2020).

[108] Dario Ballarini and Simone De Liberato. "Polaritonics: From Microcavities to Sub-Wavelength Confinement". In: *Nanophotonics* 8.4 (Mar. 26, 2019), pp. 641–654. ISSN: 2192-8614. DOI: 10.1515/nanoph-2018-0188. URL: http://www.degruyter.com/view/j/nanoph.2019.8.issue-4/nanoph-2018-0188/nanoph-2018-0188.xml (visited on 01/24/2020).

[109] M. Załużny and C. Nalewajko. "Coupling of Infrared Radiation to Intersubband Transitions in Multiple Quantum Wells: The Effective-Medium Approach". In: *Phys. Rev. B* 59.20 (May 15, 1999), pp. 13043–13053. ISSN: 0163-1829, 1095-3795. DOI: 10.1103/PhysRevB.59.13043. URL: https://link.aps.org/doi/10.1103/PhysRevB.59.13043 (visited on 04/22/2020).

[110] M. Załużny and W. Zietkowski. "Intersubband Cavity Polaritons: The Role of Higher Photonic Modes". In: *Phys. Rev. B* 80.24 (Dec. 1, 2009), p. 245301. ISSN: 1098-0121, 1550-235X. DOI: 10.1103/PhysRevB.80.245301. URL: https://link.aps.org/doi/10.1103/PhysRevB.80.245301 (visited on 04/22/2020).

[111] Alexey Kavokin, ed. *Microcavities*. Second Edition. Series on Semiconductor Science and Technology 16. Oxford ; New York, NY: Oxford University Press, 2017. 592 pp. ISBN: 978-0-19-878299-5.

[112] Simone De Liberato and Cristiano Ciuti. "Quantum theory of electron tunneling into intersubband cavity polariton states". In: *Physical Review B* 79.7 (2009), p. 075317.

[113] Yuk Nga Chen et al. "Microcavity Enhanced Quantum Well Infrared Photodetector". In: *CLEO: 2013*. Optical Society of America, 2013, QF1A.5. DOI: 10.1364/CLEO_QELS.2013.QF1A.5. URL: http://www.osapublishing.org/abstract.cfm?URI=CLEO_QELS-2013-QF1A.5.

[114] Pierre-Baptiste Vigneron et al. "Quantum Well Infrared Photo-Detectors Operating in the Strong Light-Matter Coupling Regime". In: *Appl. Phys. Lett.* 114.13 (Apr. 2019), p. 131104. ISSN: 0003-6951, 1077-3118. DOI: 10.1063/1.5084112. URL: http://aip.scitation.org/doi/10.1063/1.5084112 (visited on 02/14/2020).

[115] Xingxing Chen et al. "Mode Modification of Plasmonic Gap Resonances Induced by Strong Coupling with Molecular Excitons". In: *Nano Lett.* 17.5 (May 10, 2017), pp. 3246–3251. ISSN: 1530-6984,

1530-6992. DOI: 10.1021/acs.nanolett.7b00858. URL: https://pubs.acs.org/doi/10.1021/acs.nanolett.7b00858 (visited on 02/14/2020).

[116] Neereja M. Sundaresan et al. "Beyond Strong Coupling in a Multimode Cavity". In: *Phys. Rev. X* 5.2 (June 29, 2015), p. 021035. ISSN: 2160-3308. DOI: 10.1103/PhysRevX.5.021035. URL: https://link.aps.org/doi/10.1103/PhysRevX.5.021035 (visited on 02/02/2020).

[117] Jino George et al. "Multiple Rabi Splittings under Ultrastrong Vibrational Coupling". In: *Phys. Rev. Lett.* 117.15 (Oct. 6, 2016), p. 153601. ISSN: 0031-9007, 1079-7114. DOI: 10.1103/PhysRevLett.117.153601. URL: https://link.aps.org/doi/10.1103/PhysRevLett.117.153601 (visited on 02/02/2020).

[118] Sal J. Bosman et al. "Multi-Mode Ultra-Strong Coupling in Circuit Quantum Electrodynamics". In: *npj Quantum Inf* 3.1 (Dec. 2017), p. 46. ISSN: 2056-6387. DOI: 10.1038/s41534-017-0046-y. URL: http://www.nature.com/articles/s41534-017-0046-y (visited on 02/02/2020).

[119] Carlos Sánchez Muñoz, Franco Nori, and Simone De Liberato. "Resolution of Superluminal Signalling in Non-Perturbative Cavity Quantum Electrodynamics". In: *Nat Commun* 9.1 (Dec. 2018), p. 1924. ISSN: 2041-1723. DOI: 10.1038/s41467-018-04339-w. URL: http://www.nature.com/articles/s41467-018-04339-w (visited on 02/02/2020).

[120] David Hagenmüller, Simone De Liberato, and Cristiano Ciuti. "Ultrastrong Coupling between a Cavity Resonator and the Cyclotron Transition of a Two-Dimensional Electron Gas in the Case of an Integer Filling Factor". In: *Phys. Rev. B* 81.23 (June 2, 2010), p. 235303. ISSN: 1098-0121, 1550-235X. DOI: 10.1103/PhysRevB.81.235303. URL: https://link.aps.org/doi/10.1103/PhysRevB.81.235303 (visited on 02/17/2020).

[121] G. Scalari et al. "Ultrastrong Coupling of the Cyclotron Transition of a 2D Electron Gas to a THz Metamaterial". In: *Science* 335.6074 (Mar. 16, 2012), pp. 1323–1326. ISSN: 0036-8075, 1095-9203. DOI: 10.1126/science.1216022. URL: https://www.sciencemag.org/lookup/doi/10.1126/science.1216022 (visited on 02/15/2020).

[122] Janine Keller et al. “Few-Electron Ultrastrong Light-Matter Coupling at 300 GHz with Nanogap Hybrid LC Microcavities”. In: *Nano Letters* 17.12 (2017). PMID: 29172537, pp. 7410–7415. DOI: 10.1021/acs.nanolett.7b03228. eprint: https://doi.org/10.1021/acs.nanolett.7b03228. URL: https://doi.org/10.1021/acs.nanolett.7b03228.

[123] V. M. Muravev et al. “Observation of Hybrid Plasmon-Photon Modes in Microwave Transmission of Coplanar Microresonators”. In: *Phys. Rev. B* 83.7 (Feb. 22, 2011), p. 075309. ISSN: 1098-0121, 1550-235X. DOI: 10.1103/PhysRevB.83.075309. URL: https://link.aps.org/doi/10.1103/PhysRevB.83.075309 (visited on 02/15/2020).

[124] Xinwei Li et al. “Vacuum Bloch–Siegert Shift in Landau Polaritons with Ultra-High Cooperativity”. In: *Nature Photon* 12.6 (June 2018), pp. 324–329. ISSN: 1749-4885, 1749-4893. DOI: 10.1038/s41566-018-0153-0. URL: http://www.nature.com/articles/s41566-018-0153-0 (visited on 02/15/2020).

[125] D. Schurig et al. “Metamaterial Electromagnetic Cloak at Microwave Frequencies”. In: *Science* 314.5801 (2006), pp. 977–980. ISSN: 0036-8075. DOI: 10.1126/science.1133628. eprint: https://science.sciencemag.org/content/314/5801/977.full.pdf. URL: https://science.sciencemag.org/content/314/5801/977.

[126] N. Kanda, K. Konishi, and M. Kuwata-Gonokami. “Terahertz wave polarization rotation with double layered metal grating of complimentary chiral patterns”. In: *Opt. Express* 15.18 (Sept. 2007), pp. 11117–11125. DOI: 10.1364/OE.15.011117. URL: http://www.opticsexpress.org/abstract.cfm?URI=oe-15-18-11117.

[127] Curdin Maissen et al. “Ultrastrong Coupling in the near Field of Complementary Split-Ring Resonators”. In: *Phys. Rev. B* 90.20 (Nov. 24, 2014), p. 205309. ISSN: 1098-0121, 1550-235X. DOI: 10.1103/PhysRevB.90.205309. URL: https://link.aps.org/doi/10.1103/PhysRevB.90.205309 (visited on 04/23/2020).

[128] John F. O’Hara et al. “Effects of Microstructure Variations on Macroscopic Terahertz Metafilm Properties”. In: *Active and Passive Electronic Components* 2007 (2007), p. 049691. ISSN: 0882-7516. DOI: 10.1155/2007/49691. URL: https://doi.org/10.1155/2007/49691.

[129] Gerald Bastard. *Wave Mechanics Applied to Semiconductor Heterostructures*. Monographies de Physique. Les Ulis Cedex, France : New York, N.Y: Les Editions de Physique ; Halsted Press, 1988. 357 pp. ISBN: 978-0-470-21708-5 978-2-86883-092-0.